Linking Cyanobacterial Carboxysome Maturation, Permeability, and Equilibria via Redox Dynamics

By

CLAIR ANNE HUFFINE

B.S., Chemistry, University of North Carolina Asheville, 2020

B.S., Biology, University of North Carolina Asheville, 2020

A thesis submitted to the

Faculty of the Graduate School of the

University of Colorado in partial fulfillment

of the requirement for the degree of

Doctor of Philosophy

Department of Biochemistry

2025

Committee Members:

Boswell Wing

Aaron Whiteley

Amy Palmer

Sabrina Spencer

Roy Parker

Huffine, Clair Anne (Ph.D., Biochemistry)

Linking Cyanobacterial Carboxysome Maturation, Permeability, and Equilibria via Redox Dynamics

Thesis directed by Prof. Jeffrey C. Cameron

With history spanning from the first known fossils and oxygenating the Earth's atmosphere, to performing 25% of modern annual carbon fixation, the photosynthetic prokaryotes, cyanobacteria, are fundamental to life on Earth. They accomplish this feat of carbon fixation by implementing an efficient CO_2-concentrating mechanism (CCM) featuring proteinaceous bacterial microcompartments called carboxysomes. The CCM drives the formation of a CO_2-rich environment inside carboxysomes where the carbon-fixing machinery, ribulose-1,5-bisphosphate carboxylase/oxygenase (Rubisco) and carbonic anhydrase, are housed. The internal environment of carboxysomes is more oxidizing than the surrounding cytosol but the chemical permeability across the protein shell of carboxysomes is largely unknown. In this thesis I utilize a redox-sensitive GFP construct with timelapse fluorescence microscopy to track the redox state of immature and mature carboxysomes under perturbed conditions (high/low [CO_2] and addition of redox agents). These experiments have revealed that the redox state and permeability of carboxysomes are dynamic, responding to environmental changes, and capable of returning to the initial steady-state conditions. This work provides critical understanding of the redox-based mechanisms driving carbon-fixing regulation and robustness under changing environmental state essential for implementation of carboxysomes in biotechnological applications and climate change.

Dedication:

I dedicate my dissertation to my truly special mentor, Professor Jeffrey Cameron, who passed away five months before my defense. Jeff was one of the most brilliant scientists I have ever had the honor to meet. I hope to channel in my dissertation the limitless love and enthusiasm for science that he overflowed with to all whom he interacted with. Always ready with a creative question to any scientific discussion that somehow managed to both come from a unique angle while also striking right into the heart of the matter. Jeff taught me how to ask what was not being asked and to see life not as an unknowable complexity, but simple solutions to processes constrained by the fundamental laws that govern all of physics and beyond. As Jeff put it, he sought to solve The Equation of Life. Thank you for everything you gave me Jeff, I hope to make you proud.

Acknowledgements:

A PhD is a long journey, and many people play important roles along the way. I want to first thank my parents, Nancy and Andy Huffine, for their constant support of my choices and path. They taught me lessons essential for all of life: trust in oneself, curiosity of the world around me, and a love of nature. I wrote my thesis in a conversational style with my parents in mind so that a wider audience may be able to follow along and enjoy reading what I have learned. I extend my thanks to the BioFrontier's IQ Biology program and admin, Kristin Powell and Stephanie Hoyt, for without I would not be the interdisciplinary, versatile scientist I am today, to the Biochemistry Department, who did so much to support me and my lab in the wake of Jeff's passing, and my committee, Boswell (Boz) Wing, Aaron Whiteley, Amy Palmer, Sabrina Spencer, and Roy Parker, for many fruitful discussions and wise guidance. In particular, thank you Boz for being my unofficial co-PI all these years. You have been a rock-solid source of invigorating scientific discussion and a wellspring of excellent mentorship.

I want to thank all the friends who supported me, gave me guidance in rough times, and celebrated successes with me at various points along the way in my PhD: Matthew Campbell, Zachary Maas, Holly Coleman, Rosie Garris, Lukas Buecherl, Catherine Fontana, and many more. I thank Andrew, the ever-friendly barista at Bona Coffee Roasters, for making the dozens of vanilla lattes that fueled the writing of this thesis And lastly, I want to thank all my lab mates over the years and in particular: Anton Avramov, Chris Brininger, Kelsey Dahlgren, Andrew Hren, and Liora Goldstein. My lab mates made every day in lab a blast and were always a helpful source of scientific advice, were fun companions on our many so-called "lab retreat" adventures and will forever be my lab family.

Thank you all, I could not have done this without you.

Table of Contents

Tables

Figures

Chapter 1 - Introduction

To conquer the planet, life needs to source and harness two ingredients: energy and elemental building blocks. Energy comes in the form of chemical and electron potentials, and the building blocks are the elements: carbon, oxygen, nitrogen, hydrogen and so on. Life uses energy to transform these building blocks into all the complex biomolecules needed for life to grow and replicate.

Day to day we are familiar with energy in the form of electricity. Electrons are transferred using energy sourced from burning fossil fuels or harvested with renewable energies to ultimately power the modern world around us. Similarly, in cells, chemical and electron potentials are either generated by breaking down food as 'fuel' (carbohydrates, proteins, etc), called heterotrophy, or by utilizing external energy sources like the sun or thermal vents to harvest sources of electrons, called autotrophy. Since producing the 'fuel' used by heterotrophs requires energy input in the first place, forms of autotrophy were key to the development of early life.[1–3] The most notable form of autotrophy is oxygenic photosynthesis. Photosynthetic organisms first split water to harvest electrons. These electrons are energetically excited using energy from the sun and then, through a series of 'hot potato' with these excited electrons, the solar energy is carefully transferred into compounds that go on to power formation of biomolecules.[4]

Much like how you are always hungry and the dishes are never done, life on Earth requires sources of energy (first law of thermodynamics) and increasing entropy (second law of thermodynamics) to exist.[5–7] An essential stage upon which these fundamental laws of the universe play out in cells is with this transfer of electrons from one compound to another. Energy is transformed, moved from compound to compound, and entropy is increased, the electron 'hot potato' heats up its surroundings and itself becomes easier to handle. The tendency of compounds to gain electrons (reduction) or loose electrons (oxidation) is referred to as reduction-oxidation (redox) potentials. These redox potentials are realized through redox reactions and have been an essential component of the chemistry of life since the formation of the first biomolecules on Earth ~4.36 Gya ± 0.1 Gya (1 Gya is 1 billion years ago).[8,9]

Giving real meaning to the word (r)evolutionary, cyanobacteria are the organisms responsible for the evolution of oxygenic photosynthesis and where these processes I have described have been playing out for nearly 3 billion years.[10] Cyanobacteria harvest the energy of the sun to generate chemical and redox potential: Chemical potential, ultimately in the form of ATP, serves as the main energy currency in biomolecule formation and redox potential takes the form of electron-giving (reducing) compounds like NADPH and $FADH_2$. With the power stored in ATP and NADPH, cyanobacteria collect the essential element of life, carbon, from atmospheric carbon dioxide (CO_2) and "fix" it into bigger compounds used to ultimately create all other biomolecules (proteins, lipids, sugars, etc).

Carbon-fixation is accomplished by the most abundant enzyme on Earth: Rubisco (Ribulose-1,5-Bisphosphate Carboxylase/Oxygenase).[11] In cyanobacteria, this enzyme is housed in a protein-encapsulated compartment, called the carboxysome, which is the focus of my PhD thesis. The carboxysome is a key feature of the cyanobacterial CO_2 concentrating mechanism (CCM) designed to provide a CO_2-rich environment around Rubisco, and, without the protein shell of the carboxysome fully encapsulating Rubisco, cyanobacteria cannot grow in air.[12] Despite its essentiality for cyanobacteria survival, it is not known what exactly is the role of the carboxysome shell in this CCM process.[13–15] As the inside of the carboxysome is a different redox environment than the rest of the cell[16,17] which may be used to turn off and on the function of some of the encapsulated proteins,[18–20] I propose that redox may provide critical insights to this mystery.

In the work described in this thesis I will explore the dynamics of the redox environment within the carboxysome primarily with use of a redox-sensitive fluorescent probe[21] and imaging the growth of cells over time on a widefield microscope. My second chapter will lay out the background literature on what is known about cyanobacterial carbon fixation, the carboxysome, and redox regulation followed by a chapter on the methods I employed in my research. The fourth chapter details work on how the carboxysomal redox state changes in response to alteration of CO_2 levels. The fifth chapter is on neural networks I trained for analysis of the microscopy imaging used throughout my work. This work is published in Photosynthesis Research.[22] The sixth chapter is on further study of carboxysome response to external redox shifts to better understand the permeability of the carboxysome shell. And lastly, my seventh chapter contains the conclusions of my PhD research and what this work means for the field of cyanobacteria and CO_2 capture.

Chapter 2 – Literature Review

This chapter was partially adapted from:

Huffine, C. A.; Wheeler, L. C.; Wing, B.; Cameron, J. C. (2022). Computational Modeling and Evolutionary Implications of Biochemical Reactions in Bacterial Microcompartments. Current Opinion in Microbiology, 65, 15–23. https://doi.org/10.1016/j.mib.2021.10.001.

Huffine, C. A.; Zhao, R.; Tang, Y. J.; Cameron, J. C. (2023). Role of Carboxysomes in Cyanobacterial CO2 Assimilation: CO2 Concentrating Mechanisms and Metabolon Implications. Environmental Microbiology, 25 (2), 219–228. https://doi.org/10.1111/1462-2920.16283.

Huffine, C. A.; Avramov, A.; Fontana, C.; Sempeck, C.; Cameron, J. C. Shell Permeability and [CO_2] Alters Cyanobacterial Carboxysome Redox State. (2025). *In Review. Nature Microbiology.*

2.1 Cyanobacterial Photosynthesis

2.1.1 Light Reactions: Oxygenic Photosynthesis

While it is unknown yet how life originally evolved on Earth, the story I will weave for you involves ancient processes and begins here. What is known is that sometime around 3.5-3.9 Gya (1 Gya = 1 billion years ago), life existed on Earth in the form of single celled organisms.[8,23] The bombardment of asteroids on young Earth, only 0.6-1 Gya old at this point, had slowed, giving time and space for life to arise.[8,24] Given that life on Earth as we know is based around the element carbon, one of life's main goals is acquiring carbon to form all biomolecules. Some organisms are self (auto) nourishing (troph). These autotrophs collect carbon from inorganic sources in their environment, such as carbon dioxide (CO_2). However, for these organisms to generate enough energy to accomplish this task is no small order. The first autotrophs were chemo (chemical) trophs who solely utilized hydrogen gas produced by hydrothermal vents as an energy source.[1] While early communities of life thrived in these geological wellsprings of energy, the chemotrophs were locationally-limited to hydrothermal vents (when was the last time you stopped by your local hydrothermal vent on the way to work?) and energy-limited by the complex processes involved in harvesting sufficient energy from hydrogen.[1–3] Thus, the evolution of photosynthesis, using light from the sun as a power source, dramatically changed the primary productivity of microorganisms on Earth.[25] Light is abundant, energy rich, and not locationally limited. Go back far enough in the food chain and you'll find we are nearly all entirely solar powered.

In brief, photosynthesis involves the capture and funneling of light energy to excite electrons harvested from an electron source. These electrons are passed along an electron transport chain and in the process, the energy from the sun that they contain is used to create chemical gradients that, like water flowing through a dam, powers the production of chemical units of energy that life uses for all its processes.

The evolution of photosynthesis was long and complicated, unsurprising given how incredible a feat it is for life to create biological "solar panels."[26] Arising sometime between 2.3 and 3.5 Gya,[27,28] photosynthesis is thought to have first evolved as an anoxygenic (without oxygen) process, using substrates such as sulfide, organic compounds, and metals as electron sources.[26] Considering that water is practically everywhere compared to the substrates I just listed, the breakthrough of using water as an election source, called oxygenic (with oxygen) photosynthesis, was perhaps one of the most important evolutionary steps in Earth's history. Abundant light as an energy source, abundant water as an electron source, and abundant atmospheric CO_2 as a carbon source. Life is ready to take over the planet.

Oxygenic photosynthesis is thought to have been developed by the ancestors of my organism of study: cyanobacteria.[26] As the name 'cyan' implies, these bacteria are a lovely blue-green color due to their photosynthetic pigments used to harvest light energy. In oxygenic photosynthesis, electrons are sourced for energy from splitting water (H_2O) into its components, hydrogen, used for the proton gradients that drive adenine triphosphate (ATP) production, and oxygen. The electrons themselves are ultimately transferred to compounds (<u>N</u>icotinamide <u>A</u>denine <u>D</u>inucleotide <u>P</u>hosphate (NADPH) and <u>F</u>lavin <u>A</u>denine <u>D</u>inucleotide ($FADH_2$)) that serve as an electron source in subsequent biomolecule creation, as I will describe next. Oxygenic photosynthesis allowed cyanobacteria to overcome limitations in substrate availability and proceed to diversify across nearly every habitat of Earth, including even the most nutrient-poor and extreme (temperature, acidity, etc) environments aquatic and terrestrial.[29]

Some fun facts: Not only did oxygenic photosynthesis allow cyanobacteria to proliferate, but, alongside geological shifts, this process also changed the atmosphere and chemical state of all of Earth.[26,30] The oxygen from photosynthesis, subsequently released into the environment, is thought to have led to the Great Oxidation Event, converting Earth's atmosphere to be oxygen-rich and causing a mass extinction event for anaerobic microorganisms (oops).[30,31] Oxygen is also harmful to cyanobacteria, driving them to develop mechanisms to handle the poisonous reactive oxygen species (ROS) byproducts their photosynthetic machinery produced.[32] I will describe this in more detail in section 1.4. These ancient oxygenic photosynthesizers are not only the ancestors of modern cyanobacteria, but also the ancestors involved in the endosymbiotic event leading to chloroplasts in algae and plants.[33,34] By studying cyanobacteria, we can simultaneously learn more about the sister processes occurring in plants!

2.1.2 Dark Reactions: Carbon Fixation

We have all this light (photo) energy from photosynthesis, now let's talk about the 'synthesis' part. Taking carbon and 'fixing' it into biomolecule building blocks. Carbon fixation does not necessarily require oxygenic photosynthesis, any sufficient energy and reducing power can power the carbon fixation machinery, but in cyanobacteria, photosynthesis is the main pathway.[26] While energy sources vary, the majority of carbon fixation (in the form of CO_2) occurs through the Calvin-Benson (CB) Cycle (*Figure 1*). This cycle is the epitome of three steps forward, two steps back. To generate a single three-carbon product, the whole process must occur three times, consuming in the process hard-earned energy from photosynthesis in the form of nine ATP and six NADPH.[35]

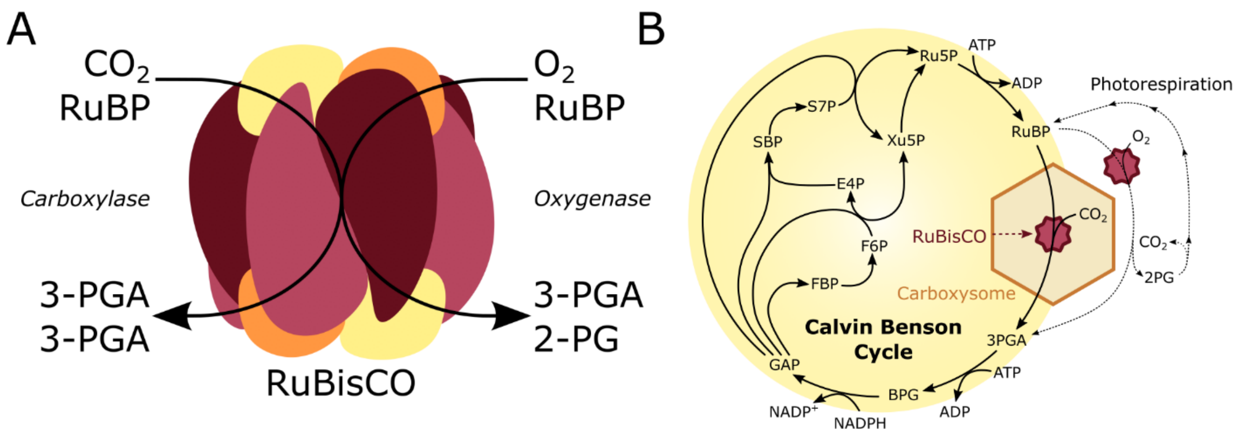

Figure 1. RuBisCO and the Calvin Benson Cycle

(A) Diagram of the carbon-fixation and oxygen-fixation reactions of RuBisCO. (B) An overview of the Calvin Benson cycle. Note, it takes six CO2 fixation events to generate one GAP to be taken out of the cycle for use as a building block for sugars, I don't have this stoichiometry included just for clarity of the visual. Panel B adapted from Huffine et.al 2023.[36]

Apologies in advance for the acronym soup in the next couple paragraphs. Bear with me through this and I will end this chapter with a table for easy reference (*Table 2*), plus a count of how many times each acronym is used in this chapter so you know which ones you actually need to remember.

The star of the show for CO_2-fixation is the enzyme Ribulose-1,5-Bisphosphate Carboxylase/Oxygenase (RuBisCO) (*Figure 1*). RuBisCO is found in plants, algae, and cyanobacteria and is the most abundant enzyme on Earth, maybe because it's the best or maybe because it has a secret dark side, jury is still out.[11] This enzyme is capable of fixing CO_2 to Ribulose-1,5-Bisphosphate (RuBP) to create two 3-Phosphoglyceric acid (3PGA) which subsequently feeds into the CB cycle to create sugars and biomass for the cell (sweet!).

Not only can RuBisCO fix CO_2, but as the 'oxygenase' part of its name implies, it can also fix oxygen (O_2) (*Figure 1*). As O_2 is molecularly hard to distinguish from CO_2, RuBisCO also fixes O_2 with RuBP, creating one molecule of 3PGA and one molecule of 2-Phosphoglyceric acid (2PG). 2PG must be processed through an energetically expensive pathway, called photorespiration, to recover the invested carbon.[37,38]In plants, this photorespiratory pathway uses 25% of a plant's energy.[37,38] While originally thought as a pathway to be avoided at all costs, more recent studies have revealed that photorespiration is actually important for cellular function, playing roles in limiting ROS, production of the amino acids serine and cysteine, and assimilation of sulfur and nitrogen.[37–40]

All that being said, there is still a strong evolutionary pressure in photosynthetic organisms for developing mechanisms to maximize RuBisCO's CO_2 fixation and minimize O_2 fixation.[41] To overcome this challenge, cyanobacteria employ a highly effective CO_2 concentrating mechanism (CCM) that results in cyanobacteria accounting for nearly 25% of annual global carbon fixation.[42] What is their secret ingredient? The cyanobacterial CCM features a bacterial microcompartment called the carboxysome,[36,43] or as I like to call it: The Box. The carboxysome is essential for cyanobacterial carbon fixation and allows for maximizing the efficient function of RuBisCO.[43] Stay tuned to learn more!

2.2 Bacterial Microcompartments

Once thought of as simple 'sacks of enzymes', it is now clear that the internal organization of bacteria rivals that of eukaryotes (like you and me).[44] For example: not only do cyanobacteria contain complex internal membranes with all their photosynthetic machinery,[44,45] but they also contain carboxysomes. Carboxysomes are a class of protein-based organelles, termed bacterial microcompartments (BMCs), that resemble icosahedral viral capsids with their protein shells and encapsulated cargo.[46]

On a broader front, BMCs have been found across at least 23 diverse bacterial phyla and are defined by a common protein shell architecture while containing different suites of enzymes in their core.[47] They fall within two main categories, catabolic (breaking down molecules) metabolosomes and anabolic (building up molecules) carboxysomes (*Figure 2*). Both categories of BMCs create a chemical and physical microenvironment inside their shell that is optimized to perform chemical reactions which would otherwise be toxic to other cellular components, create volatile intermediates, or involve enzymes, coenzymes, or intermediates that are redox-sensitive.[18–20,36,48–50] BMCs are of interest in the biotechnology world for their potential applications in controlling the flux and selectivity of biochemical reactions, containment of toxic intermediates from industrial reactions, antigen display for vaccine development, and creation of nanoparticles in chemotherapy targeting.[51,52] Recent reviews have delved into a wide variety of topics such as BMC positioning,[53] BMC repurposing for industrial uses,[50] evolutionary relationship of shell proteins across different BMCs,[54] and BMC protein stoichiometry.[55,56]

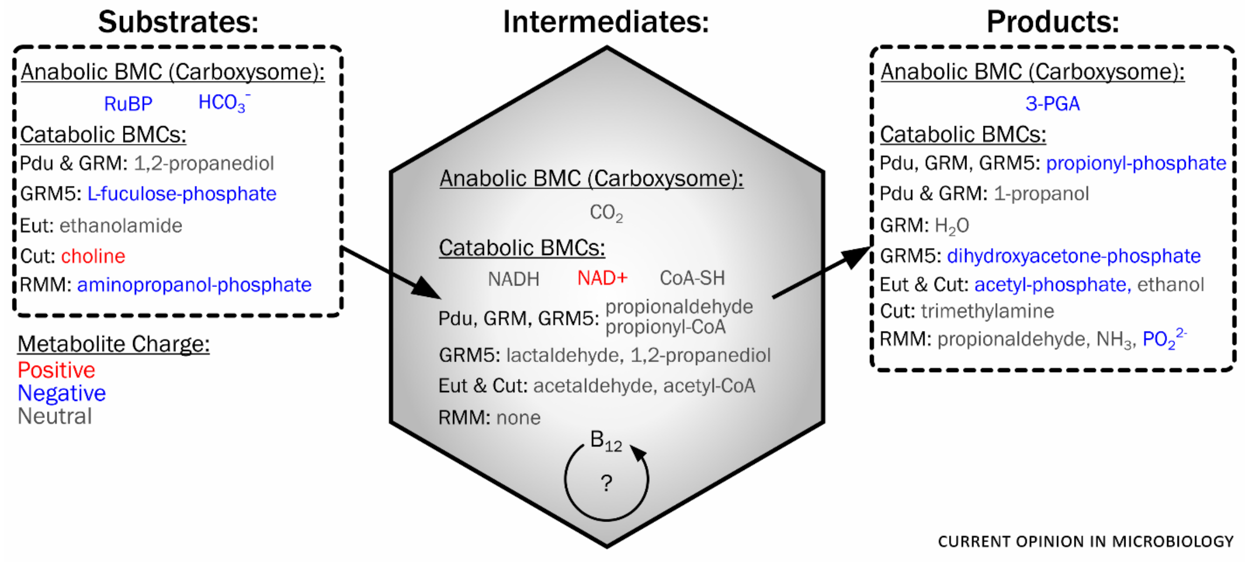

Figure 2. Bacterial Microcompartment Overview

Diagram of the substrates, intermediates, and products of carboxysomes and the most studied catabolic BMCs.[49,57–59] The charge of each metabolite is indicated with color; positive in red, negative in blue, and neutral in grey. The intermediates are nonpolar whereas substrates and products, which transverse the protein shell, are predominantly negatively charged or nonpolar. There is theorized inclusion of B_{12} cycling inside some catabolic BMCs.[49,59] Abbreviations: BMC, bacterial microcompartments; RuBP, ribulose-1,5-bisphosphate; Pdu, 1,2-propanediol utilization; GRM, glycyl radical enzyme-associated microcompartments; GRM5, fuculose-associated microcompartment; Eut, ethanolamine utilization; Cut, choline-utilization; RMM, 1-amino-2-propanol utilization; 3-PGA, 3-phosphoglyceric acid. Figure adapted from Huffine et.al. 2022.[43]

Despite this intense focus on synthesizing what is currently known about BMCs, many important details remain unknown about the function(s), assembly mechanisms, stability, and ultimate use in enhancing the biochemical reactions that they encapsulate. Due to their small size (40-600 nm, that's about one thousandth the width of a human hair)[60,61] and sub-cellular heterogeneity (e.g. intact/functional, assembly intermediates, and degrading stages),[62] the chemical environment inside BMCs remains challenging to experimentally measure with standard technologies. Recent work tracking the position and activity of individual BMCs for the first time through single-cell lineages addresses this heterogeneity and points towards a solution for understanding how the chemical environment of BMCs dictate activity and degradation.[62]

2.3 Cyanobacterial Carboxysomes

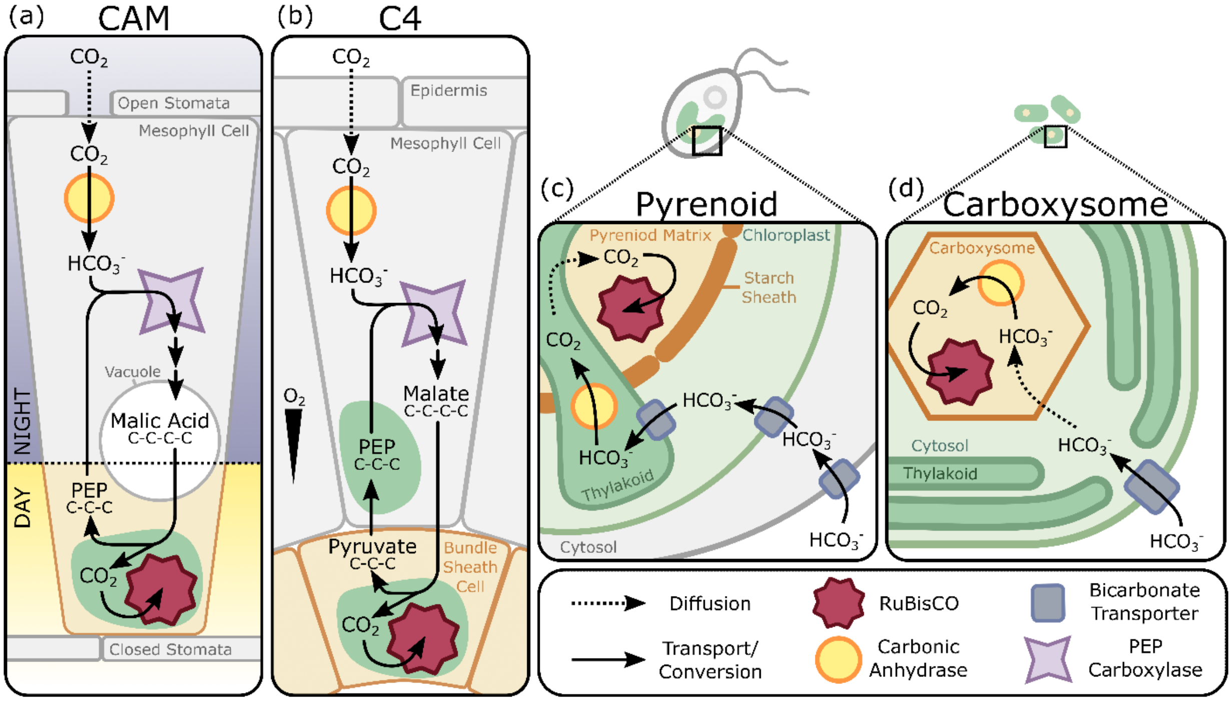

Figure 3. Carbon Concentrating Mechanisms

Diagram of CCMs across plants, algae, and cyanobacteria. (a) Crassulacean acid metabolism (CAM) plants have a temporal CCM, in which carbon is stored as malic acid in vacuoles during the night, when stomata are open to allow free diffusion of CO_2 and molecular oxygen (O_2), and then fixed during the day, when stomata are closed to reduce water loss. (b) C4 plants have a spatial CCM, in which CO_2 is first converted to malate in mesophyll cells and then malate is transported to bundle-sheath cells, where carbon is then fixed in an environment with reduced levels of O_2. (c) Pyrenoids, found in many species of eukaryotic algae as well as in the bryophyte hornworts, contain RuBisCO within a pyrenoid matrix shielded from CO_2 and O_2 diffusion by a starch sheath. Bicarbonate (HCO_3^-) is actively transported into the thylakoid lumen, which crosses through the pyrenoid matrix, and is converted back into CO_2 by carbonic anhydrase (CA). CO_2 diffuses into the pyrenoid matrix and undergoes fixation by RuBisCO. (d) Cyanobacteria encapsulate RuBisCO and CA in proteinaceous compartments known as carboxysomes. HCO_3^- from the environment is accumulated using active transport mechanisms to maintain a high concentration in the cell. In these various ways, all four CCMs simultaneously increase CO_2 concentrations around RuBisCO while excluding or outcompeting O_2, which increases the carboxylation rate and reduces oxygen fixation and photorespiration. Abbreviations: PEP, phosphoenolpyruvate; PEP Carboxylase, phosphoenolpyruvate carboxylase. Figure adapted from Huffine et.al. 2023.[36]

As I introduced prior, the anabolic BMC, the carboxysome, is the central gem around which the cyanobacterial CCM (CO_2 concentrating mechanism in case you forgot!) functions and the focus of the rest of my thesis. While the specific type and mechanisms of CCMs found in plants, algae, and cyanobacteria differ, they all lead to an increased concentration of CO_2 around RuBisCO to enhance carbon fixation and limit photorespiration (*Figure 3*).[36] It is notable that not all plants or algae contain CCMs, but all free-living cyanobacteria contain carboxysomes and their presence is required for survival under current ambient CO_2 levels (0.04% of our atmosphere).[41] The shared characteristics of the independently evolved CCMs in plants, algae, and cyanobacteria highlight the key components necessary to increase carbon fixation by RuBisCO under both similar and disparate selective pressures. While competing theories exist, studies indicate that the cyanobacterial CCM could have evolved in response to rising oxygen levels rather than as a result of limiting CO_2 in the ancient atmosphere.[31]

The carboxysome is a fascinating specialized region of the cell, being a highly stable complex (~16 hours half-life) that persists over multiple cell generations.[62] The carboxysome houses not only our new favorite enzyme; RuBisCO, but also the remarkably fast enzyme; carbonic anhydrase (CA) (*Figure 4*).[63–65] Through the creation of high levels of bicarbonate (HCO_3^-) in the cell via HCO_3^- transporters,[66,67] and CA's activity converting HCO_3^- to CO_2 exclusively in the carboxysome, a CO_2-rich environment 1000-fold higher than ambient levels is created around RuBisCO.[65,68] Much remains to be discovered about the exact details of the carboxysome lifecycle, permeability, and internal chemical environment. The work presented in this thesis is but one PhD's worth of effort to push the edges of the unknown regarding these aspects of the carboxysome. Let's dive in!

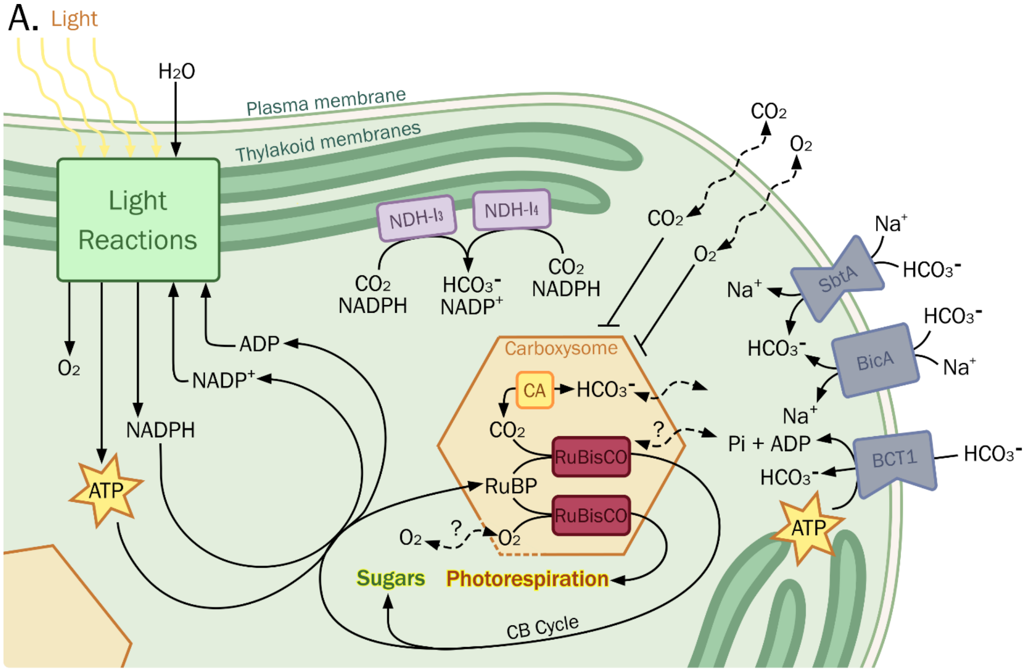

Figure 4. Cyanobacterial CCM

Schematic representations of the CCM and light reactions of oxygenic photosynthesis in beta-cyanobacteria. Included are the active carbon uptake complexes, NDH-I_3 and NDH-I_4, bicarbonate transporters, BCT1, BicA, and SbtA, and carboxysome enzymes, carbonic anhydrase (CA) and RuBisCO. Inorganic carbon, in the form of bicarbonate (HCO_3^-), is actively transported via transporters (BCT1, BicA, SbtA) into the cell. Carbon dioxide (CO_2) enters the cell via passive diffusion and is then converted to HCO_3^- by thylakoid membrane-localized NDH-I_3 and NDH-I_4 to increase cytoplasmic HCO_3^- concentration. HCO_3- diffuses across the proteinaceous shell into the carboxysome, where it is brought into equilibrium with CO_2 by CA in a fully reversible reaction. CO_2 is then fixed by RuBisCO using ribulose-1,5-bisphosphate (RuBP) as an acceptor molecule, resulting in the production of substrates that are converted into carbohydrates through the Calvin-Benson Cycle (CB Cycle). The CB Cycle is powered with ATP and NADPH produced from photosynthetic light reactions. RuBisCO may require inorganic phosphate (Pi) for activation. RuBisCO can also undergo a side reaction with O_2 leading to an energetically expensive carbon recovery pathway called photorespiration, but this reaction may mainly occur in broken carboxysomes (dotted shell line). Figure adapted from Huffine et.al. 2022.[43]

In general, carboxysomes are composed of several different types of shell proteins, the enzymes RuBisCO and CA, and scaffold proteins that hold everything together.[19,20,69] There are two types of carboxysomes, α-carboxysomes and β-carboxysomes. They are structurally and functionally similar, with homologous (similar) shell proteins and enzymes, but are evolutionarily distinct and have different molecular scaffolds responsible for assembly. Same but Different. A number of recent reviews detail these differences.[54,70,71] For the purpose of this thesis, we will concern ourselves with the β-carboxysome with aspects of the α-carboxysome being points of comparison where relevant. You may assume that, unless specified otherwise, I am describing and referring to the β-carboxysome from this point on.

I have outlined three features of the carboxysome: the shell, the enzymes, and the scaffold. I will first describe each of these parts and then, before your very eyes, I will build the carboxysome so you may understand not only what it is comprised of but also how all the pieces come together (*Table 1*).

Table 1. Beta Carboxysome Components

Proteins comprising the β-carboxysome in *Synechococcus sp.* PCC 7002.[70,72,73]

Name	**Description**	**Location**	**Function**
CcmK1	BMC-Hexamer	Shell	Shell
CcmK2	BMC-Hexamer	Shell	Shell
CcmK3	BMC-Hexamer	Shell	Shell
CcmK4	BMC-Hexamer	Shell	Shell
CcmL	BMC-Pentamer	Shell	Shell vertex
CcmM	RuBisCO nucleation protein	Core	Carboxysome assembly
CcmN	Encapsulation protein	Core	Carboxysome assembly
CcmO	BMC-Trimer	Shell	Shell
CcmP	BMC-Trimer	Shell	Shell
CcmS	Chaperonin	Cytosol	Shell Assembly
RbcL	Form 1B RuBiscO large subunit	Core	CO_2 Fixation
RbcS	Form 1B RuBiscO small subunit	Core	CO_2 Fixation
RbcX	Chaperonin	Core/Cytosol	RuBisCO Assembly
CcaA/IcfA	β-class carbonic anhydrase	Core	CO_2 generation

2.3.1 Carboxysome Shell

My first introduction to the proteins that comprise the carboxysome shell was the day I interviewed with Dr. Jeffrey Cameron at the University of Colorado Boulder. He sat me down in his office and handed me a couple of large-knobby hexagon-shaped 3D printed models. Little did I know what I was holding was to become, in only a few short years, the focus of much of my time and fascination. Jeff asked me: “How do those fit together?” and like a kid with their first LEGO set, I proceeded to play with these structures to see how different orientations let them nestle closely together. *In plastico* research as Jeff liked to call it. Given their hexagonal (six-sided) disk shape, they easily fit side-by-side, which Jeff confirmed was their usual orientation.

The proteins these models represented, I then learned, would tessellate to create a flat sheet. Where two of these sheets met would create edges. And where five of these connected sheets intersected would be vertices, capped by a pentameric shell protein (which Jeff then handed me a model of). With this, an icosahedral shape would come to be (*Figure 5A*). If you are a little confused on the shape I am describing, for those who play Dungeons and Dragons, picture a D20 dice.

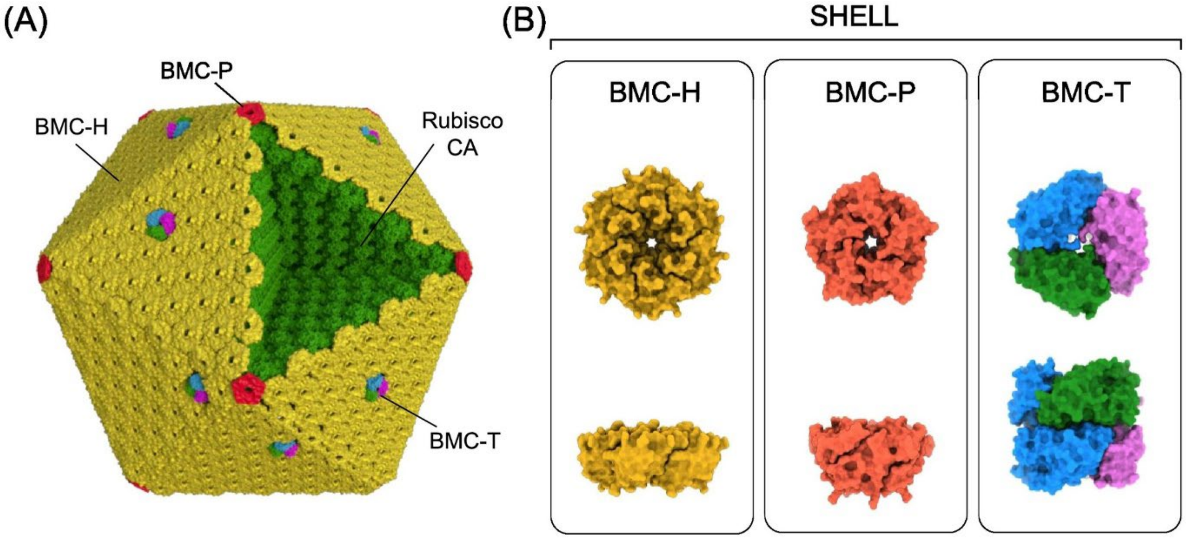

Figure 5. Carboxysome Shell

(A) A model of the carboxysome showing the icosahedral shape and the shell protein localizations. (B) The three categories of shell protein, BMC-Hexamer, BMC-Pentamer, and BMC-Trimer. Image adapted from Lu-Ning Liu, 2022.[74]

There are three different groups of shell proteins: Pentamers, Hexamers, and Trimers (*Figure 5B*). The pentamer shell protein is a complex of identical five proteins (CcmL) that oligomerize (come together) to form the pentameric cap for the carboxysome shell.[75,76] The hexameric shell proteins are a bit more complicated and can be divided into two categories, homo- (same) and hetero- (different) hexamers. Homohexamers are shell protein complexes comprised of six of the same proteins and, in the cyanobacteria I study, *Synechococcus sp.* PCC 7002 (hereafter PCC 7002), there are two such homohexamers named by the protein that are their building blocks: CcmK1, CcmK2.[75,77] CcmK1 and CcmK2 are the most common shell proteins and make up the majority of the carboxysome shell structure.[75] As for the heterohexamers, there are two proteins that come together in a 1:2 ratio, CcmK3 and CcmK4 and, while not essential, they are thought to be important for regulation of carboxysome permeability.[78] Lastly, the trimer shell proteins, CcmO and CcmP, retain the hexagonal shape of the hexamer shells, but are built of three proteins instead of six. CcmO is thought to reside at the edges of the shell, where the two flat planes meet, and is essential for the encapsulation of the carboxysome.[12,75] And lastly, CcmP is thought to form a dimer of trimers (*Figure 5B*), creating what has been referred to as an 'airlock' that potentially plays an important role in the passage of 3PGA and RuBP in and out of the carboxysome.[79,80]

A key feature of all the shell proteins is that, like a donut, they form a pore in their center. These pores have positively charged amino acids and vary in size from 4-7 Å for most of the shell proteins,[75,77] and ~14 Å for CcmP (plus an airlock mechanism).[79,80] For reference, an Å (angstrom) is the relative size of a single atom, CO_2 is roughly 3.3 Å in size,[81] and a single amino acid is ~3-5 Å wide.[82] So these pores are fairly restrictive, size-wise. Add in the positive charge factor, and now only neutral or negatively charged small molecules are going to easily make it past this barrier. What is the point of this barrier into and out of the carboxysome? Truth be told, no one really knows.

The carboxysome shell was historically thought to be selectively permeable to HCO_3^- while limiting diffusion of O_2 and CO_2[14,83,84], however recent computational analysis suggests that the diffusion of O_2 and CO_2 is remarkably unrestrained by the shell (not surprising given they are smaller than the pore and neutrally charged). Diffusion limitation is likely largely restricted to cations and larger molecules.[15,84,85] Which molecules, beyond the scope of carbon fixation metabolites (3PGA, RuBP), and for what purpose this diffusion limitation serves, is a woefully understudied field and an area my research provides some hints on.

2.3.2 Carboxysome Enzymes

I have already introduced the two enzymes housed in the carboxysome: RuBisCO and CA (*Table 1*), so I will use this opportunity now to describe in greater detail their composition, activation, and activity.

RuBisCO is comprised of eight copies each of two different proteins: the large subunit RbcL, and the small subunit RbcS. Their complete oligomerization is an essential component for their packaging into the carboxysome.[86,87] RbcX, a RuBisCO assembly chaperonin protein assists in this process and plays potentially critical roles in carboxysome formation.[88] The active site for RuBisCO, a spot nestled between two RbcL where the carbon fixing magic happens, must be altered before being functional. This alteration involves a specific amino acid in the active site, lysine, to be covalently bound to a CO_2 molecule in a process called carbamylation.[89] There is potential that this carbamylation serves as a control for turning on RuBisCO activity only when CO_2 levels are sufficiently high.[43] Even once activated, RuBisCO is a fairly slow enzyme, operating on a per-second timescale, entirely unlike its speedy carboxysomal enzymatic companion, CA.[90,91]

There are a couple of different CAs that can be found in carboxysomes. One of the scaffolding proteins (CcmM) that I will describe in the next section has a γ-CA region that is active in some cyanobacteria species, and nonfunctional in others.[18,63,92] In the species I study, PCC 7002, this γ-CA is not functional and, instead, a β-CA, IcfA, is encapsulated into the carboxysome.[64]

What is arguably most fascinating about carboxysomal CAs is, that if CA is active in the cytosol of the cell, then CA will rapidly dissipate the hard earned pool of cytosolic HCO_3^- and the CCM will cease to function.[93] This puts a curious limitation on CA's function where there must be some mechanism to keep CA 'off' while the carboxysome forms, and then turn it 'on' once CA is secured within a fully formed carboxysome shell. How, you may wonder? I propose redox regulation as a mechanism, which I will expand upon in much greater detail later.[18,64]

2.3.3 Carboxysome Scaffold

Much like it takes the egg in a cookie recipe to hold all the ingredients together before baking the cookies, there are proteins that function as the molecular scaffold for the carboxysome enzymes and shell. CcmM and CcmN are these carboxysome aggregation proteins. They both feature very mobile intrinsically disordered regions and more structured sticker regions that allow them to flexibly bind to multiple proteins simultaneously. CcmM binds to RuBisCO, CA, and several of the shell proteins (CcmK2, CcmK4, CcmL)[94,95] while CcmN binds to CA and shell proteins (CcmO, CcmL)[96] and, through a network of these connections, they hold the entire carboxysome assembly together (*Figure 6*).[19,20,69,96]

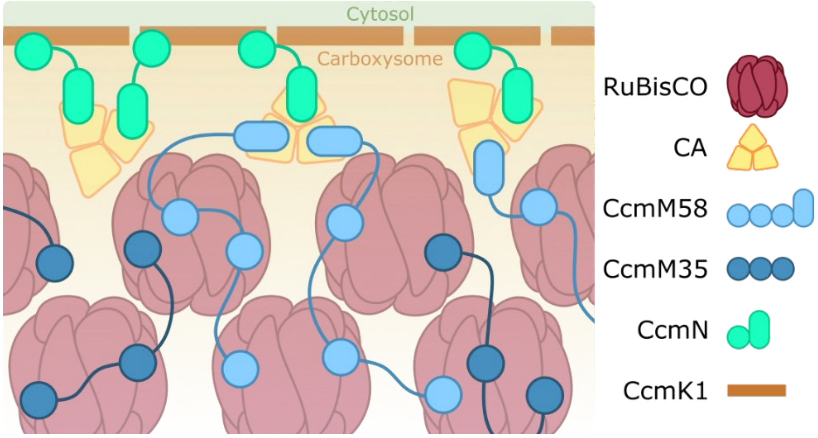

Figure 6. CcmM and CcmN Binding

Diagram of the binding pattern of the two forms of CcmM and CcmN. On CcmM, circles represent SSUL, and the rectangle represents the γ-CA domain. The lines between these are the flexible linker regions.

Going into some finer details on CcmM, this protein is comprised of the γ-CA region that I mentioned in the previous section as well as three sticker regions that closely resemble the small subunit of RuBisCO.[95] CcmM is created in two lengths: the full length CcmM-58 that includes the γ-CA region and CcmM-35 which is truncated to only the three small-subunit-like (SSUL) domains.[95] There was debate in the field for some time on if these SSUL domains replaced RbcS on RuBisCO, and it was ultimately determined that the SSUL attach to RuBisCO not where RbcS does, but instead along the equator of the RbcL.[19,20]

2.3.4 Carboxysome Lifecycle

Incredibly, all these pieces of carboxysomes are capable of self-assembling to form the beautiful, ordered structure of the carboxysome. This process begins with the aggregation of RuBisCO and CA, mediated by CcmM, to form the procarboxysome.[12,16] CcmN aids in the attachment of the shell, starting with the sheets of hexameric and trimeric shell proteins, which are then capped by the pentameric CcmL shell protein to complete the encapsulation process (*Figure 7*).[12,16] Once fully encapsulated, the carboxysome is thought to undergo a maturation process to activate CA, potentially involving a change in redox state and subsequent alteration of CcmM binding, before being a fully functional carbon-fixing compartment.[18–20] Viola! The carboxysome!

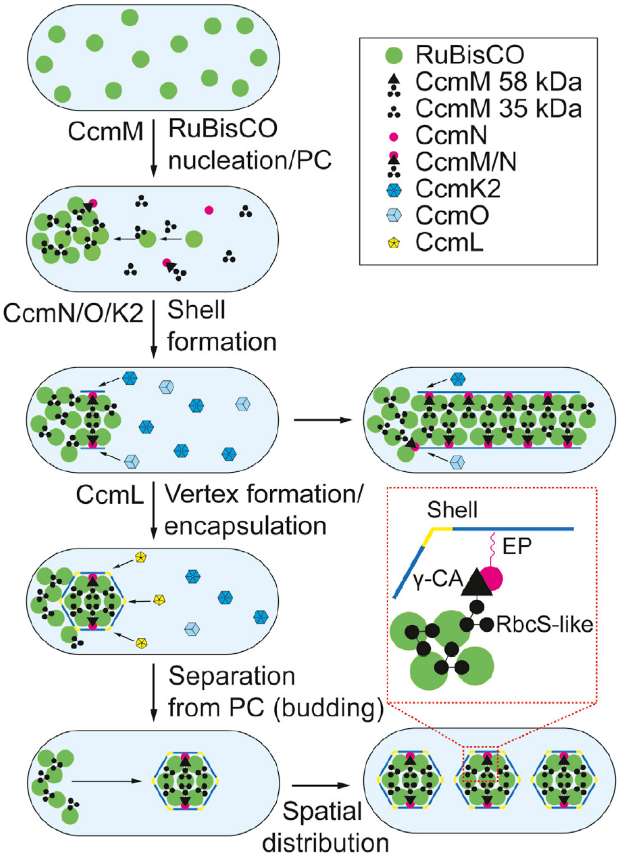

Figure 7. Formation of the Carboxysome

Diagram of the process of carboxysome formation. RuBisCO is aggregated into a procarboxysome (PC) at the pole of the cell by CcmM. This procarboxysome is then encapsulated and capped by shell proteins to form a functional carboxysome. Without the CcmL, elongated structures are formed that are unable to be fully encapsulated. Adapted from Cameron, et. al. 2013.[12]

Carboxysomes are distributed throughout the cell so when the cell later divides in two, both her daughters receive their dowry of functional carbon-fixing machinery and are ready to continue to grow and divide. This process is accomplished by a bacterial positioning system implemented in different forms across many species, McdA/B.[53,97–99] Recent reviews go into further detail on the positioning mechanism for carboxysomes.[53,100]

While carboxysomes protein complexes are remarkably structurally stable,[62] the activity of the cyanobacterial CCM is sensitive to environmental conditions including temperature, light, desiccation, and CO_2 and other nutrient levels. This sensitivity is largely controlled by HCO_3^-

transporter, RuBisCO gene expression levels, and ROS levels, with downstream impacts on cytosolic C_i levels, carboxysome number, size, and composition.[101–105] In this way the cell can flexibly respond to its environment and ensure continued survival and growth.

When a carboxysome is no longer functional, by some unknown mechanism, it makes its way to the pole of the cell where it is subsequently recycled or degraded.[62] Much remains to be discovered on what governs this process and what becomes of the many piece parts of the old carboxysome. This was originally the goal of my thesis, but fate pulls us in unexpected directions and that remains the work for another future graduate student or post doc.

2.4 Redox in Cyanobacteria

2.4.1 Cellular Redox State

Reduction-oxidation (redox) regulation is an integral aspect across a number of cellular processes, including the function of the CCM and carboxysome (*Figure 8*).[18–20,66,69,106–109] Under illumination, cyanobacterial photosynthetic machineries continually ROS through both water splitting and light energy dissipation from pigments. There are three main ROS formed, singlet oxygen ($^1O_2$), hydroxyl radicals ($\cdot OH$), and hydrogen peroxide (H_2O_2). As ROS are both useful as internal signaling molecules and damaging to the cell, their levels must be carefully regulated.[110] Levels of the longest-lived ROS, H_2O_2, are regulated via glutathione (GSH/GSSG), a non-ribosomal peptide-based antioxidant, and other oxidative stress pathways such as with catalases and peroxidases.[110–113] GSH is oxidized into GSSG when exposed to H_2O_2 and reduced by NADPH with an enzymatic catalyst. In this way, the cytosol can be maintained as a reducing environment.

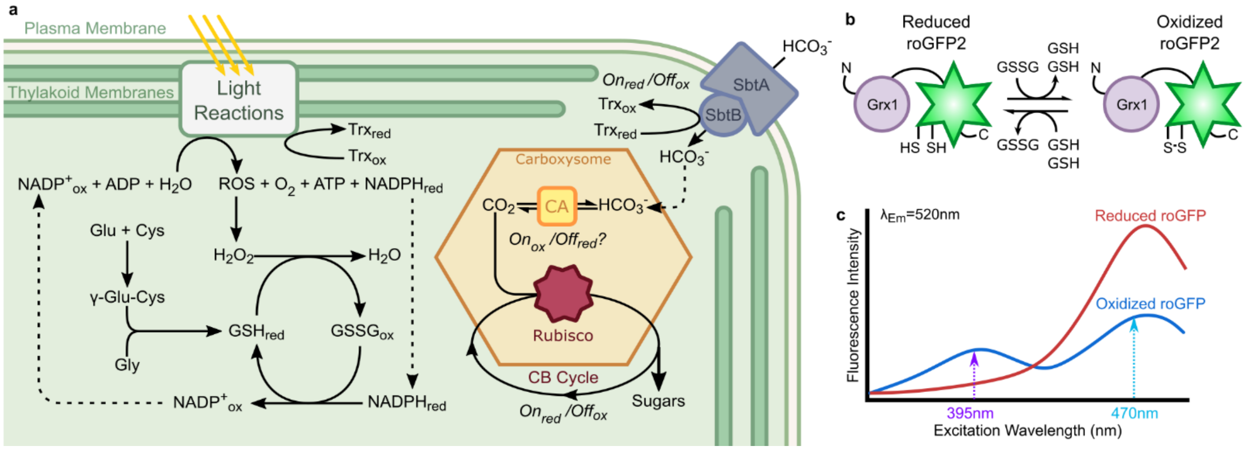

Figure 8. CCM Redox Overview

(A) Overview of known and theorized redox regulation in cyanobacteria. (B) Grx1-roGFP2 glutaredoxin specifically interacts with glutathione redox pools. (C) Grx1-roGFP2 fluorescence excitation spectrum with capability of ratiometric readout of redox environment.[21] The bimodal fully oxidized spectrum has a high fluorescence ratio $R_{395/470}$ compared to the monomodal fully reduced spectrum with a low fluorescence ratio. Emission for both excitations is collected at 520nm. Figure adapted from Huffine et.al. 2024a.[48]

2.4.2 Redox and the Carboxysome

Previous work has indicated that the internal redox environment of the carboxysome is an oxidizing environment.[16,17,20] Notably, this suggests there is likely limitation in permeability across the carboxysome shell for redox agents. However, carboxysomal redox state has neither been directly compared to the cytosol nor has a specific redox pool been targeted (until now),[16,17,20] so much remains to be explored on the redox relationship of the carboxysome to the cytosol under variable conditions. The activity and function of several CCM proteins are known to be redox-regulated, such as one of the HCO_3^- membrane transporters, SbtB/A, as way to modulate carbon uptake,[66,114] and the scaffold protein, CcmM, as a way to adjust RuBisCO packing during carboxysome formation.[18–20,106,107] Others have been indicated as redox-sensitive, such as the shell protein, CcmK4,[106,107] and both the large and small subunits of RuBisCO, but it is unknown what these redox sensitivities achieve.[106,107] The purpose and mechanism underlying this distinct redox environment in the carboxysome remains an area of active investigation. I hypothesize that the shell may serve an important role in maintaining a distinct redox state in the carboxysome to promote CCM function.

While not functional in PCC 7002, in some cyanobacterial strains, CcmM has an active γ-CA domain, which serves as the carboxysomal CA. This γ-CA is redox-regulated.[18,92] As mentioned much earlier, a cytosolically located CA would disrupt the HCO_3^- gradient generated by the CCM so CA must be inactivated during carboxysome formation in the cytosol.[93] The redox regulation of γ-CA in CcmM suggests a clear mechanism by which the γ-CA is able to be inactivated in the reducing cytosol and activated in the oxidized carboxysome via disulfide bond formation. In contrast, the functional CA in PCC 7002 is a β-CA, IcfA (also known as CcaA), for which the regulation is unclear.[64,65] While pioneer work found this β-CA to be inactivated by reducing agents,[65] cysteines involved in disulfide bond formation and redox sensing have not been identified.[64] Featured in Chapter Four, I use a knockout strain of the shell protein CcmO to trap the carboxysome in the shell-less procarboxysome stage. As the procarboxysome contains cytosolically exposed CA, the *ΔccmO* strain provides a unique opportunity to study redox environment in the procarboxysome where CA activity is thought to be inhibited by reduction.

2.4.3 Redox sensors

There are several redox pools in the cell operating both independently and in tandem, making it important to consider the dynamics of different redox pools. I use throughout my thesis a previously characterized redox-sensitive green fluorescent protein (roGFP) that is specifically capable of sensing the glutathione (GSH/GSSG) redox pool via human Glutaredoxin 1 (Grx1) (*Figure 8*).[16,21,115,116] This roGFP-Grx1 construct is highly sensitive and selective in the physiological potential range, with 100,000 faster oxidation by GSSG than roGFP alone,[21] and has been utilized in both eukaryotic and prokaryotic systems,[17,21,115,116] demonstrating the robustness and broader scope of this system. I use this tool across the rest of this dissertation to ask questions about carboxysome encapsulation, regulation, and permeability.

2.5 Synthetic Biology Applications of the Carboxysome

You are dozens of pages deep into my thesis (wow, thank you for reading this far!) and you're starting to wonder 'why exactly do we care about the cyanobacterial CCM, and the carboxysome, and how its regulated, and, and, and-." Beyond, of course, my limitless enthusiasm for this topic and passion for how cool these systems are. I will take this section to provide examples of where understanding the rules that govern carboxysomes can be very beneficial to biotechnology and sustainability.

Enhanced biological capture and conversion of CO_2 into useful products is a key step towards a sustainable future. With the increasing foundation of knowledge about the carboxysome structure and function to build on, the application of bioengineered CCMs has three main approaches:[36]

1. Expression and reconstitution of functional carboxysomes in heterotrophic bacteria to impart CO_2-fixing capabilities.
2. Expression and reconstitution of functional carboxysomes in plant chloroplasts to increase crop yields.
3. Optimization of the CCM for enhanced CO_2 fixation.

2.5.1 Carboxysome Reconstitution in Alternative Microbial Species

The reconstitution of functional carboxysomes in an alternative model host organism is an essential research goal in bioengineering. Like swappable pieces in a puzzle, this allows carboxysomal components to be synthetically altered to impart different functionality as well as permits the carboxysome for direct integration into existing pipelines for bioproduction. For example, the type of encapsulated RuBisCO in reconstituted carboxysomes could be switched or altered to increase carbon fixation rates.[117,118]

Encouragingly, functional α-carboxysome were successfully reconstituted in *Escherichia coli* through the expression of 20 CCM genes and enabled the autotrophic bacteria to grow by fixing CO_2 to biomass.[119] To achieve high CO_2 assimilation efficiency of these α-carboxysomes, chaperonins from *E. coli* (GroEL/S) and cyanobacteria (RbcX) were introduced to synthesize the α-carboxysome in *E. coli*. These chaperonins helped regulate protein folding and improved the solubility and abundance of carboxysome components.[120] As far as I am aware, β-carboxysomes have not been able to be reconstituted in other bacteria, suggesting there may be essential components we have yet to discover.[121]

2.5.2 Carboxysome Reconstitution in Chloroplasts

High photorespiration rates from O_2 fixation in C_3 plants results in a loss of 25% of fixed CO_2.[121] Introduction of cyanobacterial carboxysomes within the chloroplasts of plants could theoretically enhance the agricultural production yield for important C_3 crop plants, such as wheat and rice, as much as 60%.[122,123] Natively, these C_3 species lack the CCMs found in C_4 and CAM plant species (*Figure 3*) and to compensate for a lack of a CCM, RuBisCO is produced in excess and comprises 5% of the biomass in C_3 plants.[11] Recent proposals to enhance CCM in plants generally consist of three following elements: (1) optimized expression of carboxysomal proteins for carboxysome formation in the chloroplast, (2) knocked-out CA in the stroma, and (3) HCO_3^- transporters in the chloroplast membrane. To achieve the engineered CCM plant system, cyanobacterial RuBisCO was expressed in plants and the recombinant RuBisCO showed comparable kinetic properties to those in their native host under high CO_2 condition.[124–126] Due to the lack of HCO_3^- transporters, the engineered plants grew deficiently. More discussion of recent discoveries were well summarized in the review paper by Borden and Savage[127] with further advancements celebrated in more recent papers.[72,128]

2.5.3 CCM Optimization

Recent approaches altering carbon-fixing machinery could lead to substantial improvements over the status quo. For example, a study inspired by the packed arrangement of RuBisCO within carboxysomes generated synthetic stacked assemblies of RuBisCO that exhibited enhanced activity and stability.[129] Incorporation of RuBisCO activase within carboxysomes reduces inactivation of RuBisCO and enhances carbon-fixation.[130] Modification of other steps in the CB cycle, including the regenerative phases that produce ribulose 1,5-bisphosphate, including sedoheptulose 1,7-bisphosphate and transketolase, are also promising targets for improvement of CCMs.[131–133]

There is much more work to be done to bring these synthetic biology applications of the carboxysome to fruition in the biotechnology realm. My aspiration is that the research I have conducted in my PhD will provide one of the many keys to integration of carboxysomes in novel organisms. There is still much we must know in order for these systems to be fully functional and I am proposing that carboxysomal redox regulation is an aspect that deserves more attention when reconstituting carboxysomes.

Table 2. Abbreviation Guide

Abbreviation	**Word**	**Count**
CO_2	Carbon Dioxide	49
ATP	Adenine Triphosphate	5
NAD(P)H	Nicotinamide adenine dinucleotide phosphate	6
$FADH_2$	Flavin adenin dinucleotide	2
CB	Calvin Benson Cycle	5
RuBisCO	Ribulose-1,5-Bisphosphate Carboxylase/Oxygenase	50
RuBP	Ribulose-1,5-Bisphosphate	6
3PGA	3-Phosphoglyceric Acid	4
O_2	Oxygen	13
2PG	2-Phosphoglyceric Acid	2
CCM	CO_2 Concentrating Mechanism	32
BMC	Bacterial Microcompartment	26
CA	Carbonic Anhydrase	36
HCO_3^-	Bicarbonate	16
SSUL	Small Subunit-Like	5
GSH/GSSG	Glutathione	3
roGFP	Redox-sensitive green fluorescent protein	5

Chapter 3 – Experimental Procedures

This chapter was adapted from:

Huffine, C. A.; Avramov, A.; Fontana, C.; Sempeck, C.; Cameron, J. C. Shell Permeability and [CO_2] Alters Cyanobacterial Carboxysome Redox State. **2025**. *In Review. Nature Microbiology.*

3.1 Strain cultivation

Wild type *Synechococcus sp.* PCC 7002 (WT, hereafter PCC 7002) and all mutants produced from WT were cultivated in AL-41 L4 Environmental Chambers (Percival Scientific, Perry, IA) at 37°C under constant illumination (~150 µmol photons m^{-2} s^{-1}) by cool white, fluorescent lamps, under either ambient (air, 0.04%) or elevated (3%) CO_2 conditions. Cultures were grown in 25 ml of pH 8.2 A+ media in orbital shaking baffled flasks (125 ml) contained with foam stoppers (Jaece Identi- Plug), or on pH 8.2 A+ media solidified with Bacto Agar (1%; w/v). Antibiotics were added for routine growth of strains (kanamycin, 100 µg/ml; gentamycin, 30 µg/ml). To permit growth of otherwise lethal carboxysome mutants, these high CO_2 requiring (HCR) mutants were grown in elevated CO_2 conditions. If HCR mutants were grown on solid media, agar percentage was lowered to 0.5% w/v.[134]

3.2 Plasmid and strain construction

All plasmids and strains used are described in Table 3 and 4. Plasmids were created through Gibson assembly of plasmid backbones (pUC19) and PCR-amplified inserts, generated using Phusion polymerase (Thermo Fisher Scientific). Cyanobacterial strains were generated by transforming cells in exponential/early linear growth phase with 0.5 ng/ml of plasmid DNA, containing the insert of interest flanked by 600–base pair homology arms for recombination into a specified genomic locus. After incubation at 30°C in low constant illumination (50 to 150 µmol photons m^{-2} s^{-1}) for 24 hours, transformed cells were selected for with appropriate antibiotic at half concentration on plates in ambient CO_2, for non-HCR strains, and 3% CO_2 for HCR strains, respectively. From plates, individual colonies were serially patched onto new plates with full antibiotic concentration and tested for segregation after >3 passages. Confirmation of segregation was confirmed by PCR, using primers specific for either the insert, or the WT genome as described in Table III. Presence of the insert-specific PCR product and absence of the WT-specific PCR product was used as an indicator of full segregation.

Table 3. Strains

Name	**Number**	**Description**	**Resistance**	**Reference**
WT	-	Wild-type *Synechococcus* sp. PCC 7002	None	-
Grx1-roGFP2	scJC0501	WT cells transformed with sJC0694	Gm^R	Huffine 2025
RbcL-Grx1-roGFP2	scJC0479	WT cells transformed with sJC0683	Km^R	Huffine 2025
ΔccmO	scJC0079	WT cells transformed with sJC0132	Km^R	Huffine 2025
ΔccmO RbcL-Grx1-roGFP2	scJC0503	*ΔccmO* cells transformed with sJC0691	Km^R, Gm^R	Huffine 2025

Table 4. Plasmids

Name	**Number**	**Description**	**Genomic Site**	**Reference**
Grx1-roGFP2-His	sJC0658	Used as Grx1-roGFP2 PCR template to make sJC0694 and sJC0683	-	Gutscher 2008
Grx1-roGFP2-His_Gm^R	sJC0694	Procarboxysome*cmK2::*Grx1-roGFP2 downstream of Km^R cassette	*glpK*	Huffine 2025
RbcL-Grx1-roGFP2-His_Km^R	sJC0683	Procarboxysome*cmK2*::RbcL-Grx1-roGFP2 downstream of Km^R cassette	*glpK*	Huffine 2025
RbcL-Grx1-roGFP2-His_Gm^R	sJC0691	Procarboxysome*cmK2*::RbcL-Grx1-roGFP2 downstream of Gm^R cassette	*glpK*	Huffine 2025

Δ*ccmO*_Km^{R}	sJC0132	Km^{R} cassette flanked by *ccmO* operon upstream and downstream homology arms	*ccmO*	Huffine 2025
RbcL-GFP-V5_Km^{R}	sJC0624	Used as a PCR template to make cJC0683	*glpK*	Huffine 2025
RbcL-GFP-APEX2_Gm^{R}	sJC0490	Used as a PCR template to make cJC0691 and cJC0694	*glpK*	Huffine 2025

Table 5. Primers

Name	**Description**	**Sequence (5'-3')**	**Reference**
CHo0005	Insert amplification of sJC0658 containing Grx1-roGFP2-His for sJC0683 and sJC0691	GATCCGGGGGTGGTGGGTCTATGGCTCAAGAGTTTGTGAACTG	Huffine 2025
CHo0006	Insert amplification of sJC0658 containing Grx1-roGFP2-His for sJC0683 and sJC0694 and sJC0691	GGCTTTGTTAGACAGCCGGATCCTTAGTGATGGTGATGGTGATGAGATC	Huffine 2025
CHo0007	Vector amplification of sJC0624 containing RbcL and Km^{R} cassette for sJC0683, sJC0490 containing RbcL and Gm^{R} cassette for sJC0694, or sJC0490 containing Gm^{R} cassette for sJC0694	TAAGGATCCGGCTGTCTAACAAAGCC	Huffine 2025
CHo0008	Vector amplification of sJC0624 containing RbcL and Km^{R} cassette for sJC0683 or sJC0490 containing RbcL and Gm^{R} cassette for sJC0694	AGACCCACCACCCCCGGATC	Huffine 2025
CHo0010	Vector amplification of sJC0490 containing Gm^{R} cassette for sJC0694	CTAATTTATCCTCGCTTATCAAGCTTAATGTC	Huffine 2025
CHo0011	Insert amplification of sJC0658 containing Grx1-roGFP2-His for sJC0694	GCTTGATAAGCGAGGATAAATTAGATGGCTCAAGAGTTTGTGAACTGCAAAAT	Huffine 2025
JCC388	To test via colony PCR for presence of insert in *glpK*	CAATGGCGAAGGTTTTCTGT	Moore 2020[134]
JCC389	To test via colony PCR for presence of insert in *glpK*	GGGAGATGCTGTAGGCAAGA	Moore 2020[134]

3.3 Spot plating

The growth of PCC 7002 was measured on agar plates as described. Plates at 0.5 and 1% agar were spotted with strains in triplicate. Liquid cultures in log growth phase of each PCC 7002 strain were diluted to 0.05 OD_{730} and five 1:10 serial dilutions were performed. Five µL of the serial dilutions was used for each spot and allowed to dry (30 min – 1 hour) prior to incubation. Images were taken 3 days after spotting the plates with a backlight on a Kaiser eVision light plate and imaged with a Nikon D7200 digital single-lens reflex camera.

3.4 Liquid Growth Curves

Growth of PCC 7002 was measured in liquid cultures as described. The precultures were started from PCC 7002 cells scraped from plates and grown in the same conditions as the subsequent growth curve cultures, either ambient (air, 0.04%) or elevated (3%) CO_2 conditions. 50mL A+ cultures were inoculated in triplicate with 1 mL of PCC 7002 pre-culture diluted to 0.14 OD_{730} and grown in the standard conditions described in Strain Cultivation. During the growth curve, time points were taken every 24 hours for 72 hours. At each time point, 200 µL was removed from each culture and the OD_{730} was measured in a 96-well plate on a Tecan Spark multimode microplate reader.

3.5 Spectrofluorometer

The redox state for the Grx1-roGFP2 strains in bulk culture were measured as described.

3.5.1 Chlorophyll quantification

Pre-cultures grown in standard liquid culture conditions were used to inoculate 50mL cultures. These liquid cultures were grown to OD_{730} 0.3-1.0 in either ambient (air, 0.04%) or elevated (3%) CO_2 conditions. Chlorophyll was methanol extracted from 1 mL of culture diluted to 0.3 OD_{730} as described in Porra et al..[135] Absorbance at 665 nm was measured and the chlorophyll content was calculated with *Equation 1*.

Equation 1:
$$Chl\ a\left(\frac{\mu g}{mL\ @\ 0.233\ OD_{730}}\right) = 16.29 * Abs\ @\ 665\ nm$$

3.5.2 Fluorescent Spectra Measurement

Once each culture's chlorophyll had been quantified, each original culture was diluted to a chlorophyll concentration of 3 µg/mL in A+ media. The normalized chlorophyll cultures were loaded into a FireflySci 1FLPS Disposable Cuvette. Fluorescence was measured using a Fluorolog-3 spectrofluorometer (Horiba Jobin Yvon). Grx1-roGFP2 was excited from 350- to 480nm with a 5nm slit and a step size of 1 nm and the fluorescence emission spectra was gathered with an emission wavelength of 510nm with a 5nm slit. For sensitivity tests, either 30 mM H_2O_2 or 100 µM DTT was added to the cuvettes and allowed to incubate for 30s prior to measurement.

For the time trial with DTT addition in Chapter 6, the following alterations to the above method were observed. Separate samples were used at each timepoint so samples are not bleached by the measurement. Due to limited cultures, WT measurements were taken periodically, skipping measurements at 10 min and 40 min and n=2 at 4-6 hours. Samples at the 10- and 40-min time points were normalized with the WT background measured at the preceding timepoint.

3.5.3 Ratiometric Data Processing

In replicates of three or four, WT emission was averaged at excitation at 395- and 470nm respectively (b_{395} and b_{470}). This value was then subtracted from each Grx1-roGFP2 strain's emission value from 395- and 470nm excitation respectively (I_{395} and I_{470}) before dividing the emission from 395nm excitation by the emission from 470nm excitation (*Equation 2*) and averaging across samples.

Equation 2:

$$R_{\frac{395}{470}} = \frac{I_{395} - b_{395}}{I_{470} - b_{470}}$$

As $R_{\frac{395}{470}}$ approaches 1, then the environment that the Grx1-roGFP2 construct is in is considered oxidized.[21] In reverse, as $R_{\frac{395}{470}}$ approaches 0, then the environment that the Grx1-roGFP2 construct is in is considered reduced. In this way we can determine the relative redox state of regions of the cell where Grx1-roGFP2 is localized via tagging to proteins of known localization.

3.6 Quantitative microscopy

Fluorescence images were taken using a customized Nikon TiE inverted wide-field microscope with a near-infrared–based Perfect Focus System.[62,136] Temperature and CO_2 concentrations were controlled with a Lexan environmental chamber outfitted with a $ProCO_2$ P120 Carbon Dioxide Single Chamber Controller (BioSpherix, Parish, NY), and growth light was controlled via a transilluminating red light emitting diode (LED) light source (Lida Light Engine, Lumencor, Beaverton, OR). A highspeed light source with custom filter sets was used for imaging (Spectra X Light Engine, Lumencor, Beaverton, OR), along with a hardware-triggered and synchronized shutter for control of imaging and growth light. NIS Elements AR software (version 5.11.00 64-bits) with Jobs acquisition upgrade was used to control the microscope. Image acquisition was performed using an ORCA-Flash4.0 V2+ Digital sCMOS camera (Hamamatsu) with a Nikon CF160 Plan Apochromat Lambda 100× oil immersion objective (1.45 numerical aperture).

3.6.1 Imaging with an Agarose Pad

For long-term time-lapse microscopy on an agarose pad, cells in exponential or early linear phase were diluted to 0.14 OD_{730}, all strains were mixed in equal proportions, and five 1 µL spots were dropped onto a 1 mL 1% agarose A+ pad, formed with via the cut off top of an *E.coli* culture tube, and careful to not disrupt the surface of the pad to avoid air bubble formation during the movie.

Cells were dried onto the pad (20 min) and inverted onto a 35-mm glass bottom imaging dish (ibidi). The outside of the imaging dish was wrapped in a single layer of parafilm (careful not to have parafilm on the bottom of the dish as it will not sit flat if so) to keep the pad from drying out and add traction for the imaging dish holder on the scope. The imaging dish was then preincubated at 37°C for 1 hour in the dark on the scope to allow for all components to warm up and reduce loss of focus in the early frames of the movie. No antibiotics were included on the agarose pad. Images were taken every 20 min using a 395- (BFP), 470- (GFP), 555- (RFP) and 640nm (Cy5) LED light source (Spectra X), and emission wavelengths were collected using standard GFP (395- and 470nm excitation, 520-nm emission), RFP (595nm emission), and Cy5 (705nm) filters (Nikon). Cells were constantly illuminated with red light except during fluorescent imaging to provide light energy for cell growth.

3.6.1.1 Redox Agent Addition

For experiments where DTT or H_2O_2 are added mid-movie the following modifications to the above protocol are observed. The glass imaging dish is modified with a small hole on top, which is covered with parafilm to minimize desiccation of the imaging pad. At the designated time point, 3 µL of DTT or H_2O_2 at the desired concentration are dropped onto the back (top) of the imaging pad with a syringe, needle accessing the pad via the hole. The hole is carefully resealed with parafilm.

3.6.2 Imaging with a Microfluidics Device

For long-term time-lapse microscopy with a microfluidics device, the microscope stage was swapped for the plate-holder adapter. CellASIC® ONIX Microfluidics Plates (Type B04A for bacteria) were used. PBS was manually removed from every well and replaced with 200 µL A+ to wells in columns 1-6 (wells for media for the imaging chambers) and wells in columns 8 (wells for cell culture that is the source for injecting cells into the imaging chambers). To remove any remaining PBS, once the plate is sealed to the CellASIC® ONIX2 Microfluidics System (Cat. No. CAX2-S0000) the Liquid Priming Sequence with small modifications as follows: Column 2 is excluded due to an inability for that column to hold a vacuum, columns 6 and 8 are included, and this sequence is run at 34.5kPa for 5 min.

Meanwhile, cells in an exponential or early linear phase were diluted to 0.1 OD_{730} with A+ and all strains were mixed in equal proportions. Once the Liquid Priming Sequence is completed, all media is removed from the plate. 50 µL of the cell culture is added to each well in column 8, and 300 µL A+ to the rest of the wells if running without any condition changes. In the case of condition changes partway through the movie, 200 µL of A+ was added to the respective columns to be replaced just prior to the condition change with the additive (DTT in A+ usually). Once sealed again to the Microfluidics system and with parafilm around the edge for stability, the Run Cell Loading Sequence is run to add cells to the imaging chamber. Unstuck cells are washed away by running the Liquid Priming Sequence again but without column 8 and at 4 psi for 5 min. The whole system is incubated for 1 hour on the scope without lights at 37°C.

The microfluidics protocol was set as 8 hours Perfusion from columns 1 and 5 at 2 psi/13.8 kPa, 8 hours Perfusion from columns 3 and 4 (usually has DTT) at 2 psi/ 13.8 kPa, then back to the first state with 8+ hours Perfusion from columns 1 and 5 at 2 psi/13.8 kPa. Variable [DTT] are manually added to wells 3 and 4 <20 min prior to the switch to them to minimize DTT degradation. Images were taken every 20 min using a 395-, 470-, 555- and 640nm LED light source (Spectra X), and emission wavelengths were collected using standard GFP (395- and 470nm excitation, 520-nm emission), RFP (595nm emission), and Cy5 (705nm) filters (Nikon). Cells were constantly illuminated with red light except during fluorescent imaging.

3.6.3 Image processing and analysis

Classic cell segmentation was performed using MATLAB version R2023b as outlined previously using CyAn (https://github.com/Biofrontiers-ALMC/CyAn).[136] To segment (identify) individual cells, we also captured images in bright field, with the red growth light as an illumination source. Cells were then identified by applying an intensity threshold and watershed algorithm to create a cell mask. Manual mask correction was then performed to correct mistakes before data analysis. Cells that died or overlapped were removed from the mask and subsequent data analysis. Carboxysome and procarboxysome puncta were further segmented based on their GFP signal. Note that these mask images were only used for cell segmentation—reported data were measured from the original images.

Each cell's strain was visually identified. Puncta smaller than 62 pixels in the *ΔccmO* mutant were excluded from analysis to limit misidentified puncta from background noise. Averaged intensity of WT was used for background subtraction for 395- and 470 nm excitation channels from the averaged intensity of each cell or puncta. To account for low signal in the 470 nm excitation channel, any cell or puncta that was below zero after background subtraction was brought to zero for subsequent calculations. Redox states were calculated across all strains using Equation 2. This ratio was overlayed on the respective cell or puncta mask to generate ratiometric images for ease of visualization.

3.7 DTT degradation time trial

1mL Eppendorf tubes with 100 µL of the desired [DTT] were prepared and placed either in the AL-41 L4 Environmental Chambers (Percival Scientific, Perry, IA) at 37°C under constant illumination (~150 µmol photons m^{-2} s^{-1}) by cool white, fluorescent lamps, or in a 4°C fridge in the dark. At each timepoint the appropriate tubes were transferred to a -20°C freezer until the Ellman's assay was conducted.

3.7.1 Ellman's Assay

This assay determines the amount of free thiols in a solution. I did not run a standard curve as I was wanting to track DTT degradation overtime and was not overly concerned with the actual [DTT]. First prepare the Reaction Buffer of 0.1M pH 8 phosphate buffer solution with 1 mM EDTA. Make Ellman's Reagent solution by dissolving 4 mg DTNB in 1 mL of the Reaction Buffer. In a 96 well plate combine 12.5 µL of sample with 125 µL of Reaction Buffer and 2.5 µL of the Ellman's Reagent. Incubate at room temperature for 15 min. Run on the on a Tecan Spark multimode microplate reader measuring optical absorbance at 412 nm. Background was subtracted from each value and then the data normalized to the highest absorbance to indicate the 100% DTT activity for the assay.

3.8 Statistics

For the statistical comparison of $R_{395/470}$ for bulk culture redox state, unpaired two-tailed Student's t-tests were used. P values are indicated by asterisks; *p < 0.05, **p < 0.001, ***p < 0.0001.

Chapter 4 – Shell Permeability and [CO_2] Alters Cyanobacterial Carboxysome Redox State

This chapter was adapted from:

Huffine, C. A.; Avramov, A.; Fontana, C.; Sempeck, C.; Cameron, J. C. Shell Permeability and [CO_2] Alters Cyanobacterial Carboxysome Redox State. **2025**. *In Review. Nature Microbiology.*

4.1 Summary

Responsible for fixing 25% of CO_2 globally, cyanobacteria utilize the carboxysome to house their CO_2 fixing machinery. The permeability of the proteinaceous shell of the carboxysome is an area of active study. While necessary in air, the shell is not required when cyanobacteria are in high CO_2 levels representative of early earth. To understand how the carboxysome shell permeability responds to increased CO_2 conditions, we used a Grx1-roGFP2 redox sensor and single cell timelapse fluorescence microscopy to track subcellular redox states of *Synechococcus* sp. PCC 7002. Comparing different levels of compartmentalization, we targeted the cytosol, a shell-less carboxysomal assembly intermediate called the procarboxysome, and the carboxysome. The carboxysome redox state was dynamic and, under 3% CO_2, mirrored cytosolic redox states, indicating that more permeable shell architecture may be favorable when [CO_2] is high. This work builds understanding on the carboxysome response to changing CO_2 concentrations and the selective forces driving carboxysome evolution.

4.2 Introduction

The carboxysome shell was historically thought to be selectively permeable to HCO_3^- while limiting diffusion of molecular oxygen and CO_2[14,83,84], however recent computational analysis suggests that the diffusion of oxygen and CO_2 is remarkably unrestrained by the shell and that diffusion limitation is largely restricted to cations and larger molecules.[15,84,85] Further investigation is needed to identify which molecules, beyond carbon fixation metabolites, are subject to diffusion limitation by the carboxysome shell and to elucidate the functional significance of this selective permeability.

De novo formation of β-carboxysomes is initiated by aggregation of Rubisco and CA to the pole of the cell via the scaffold protein, CcmM, into a structure known as the procarboxysome.[12,16,18,19,69,86,137,138] The procarboxysome is a transient and short-lived intermediate preceding full encapsulation of the shell and maturation into carboxysomes.[16,62] Little is known on the permeability and functional state of procarboxysomes, however, since the shell is either absent or not yet fully formed, procarboxysomes would have greater permeability than a carboxysome.[139] The procarboxysome can be studied in a perpetual state utilizing shell knock-out mutants. In many cyanobacteria, including PCC 7002, the essential trimeric shell protein, CcmO, is encoded at a separate genomic locus distinct from the *ccm*-operon. The *ccm*-operon encodes other necessary carboxysome proteins including the hexameric (CcmK1, CcmK2) and pentameric (CcmL) shell proteins in addition to the aggregation proteins, CcmM and CcmN.[12] Failure of shell assembly in CcmO knock-out lines (Δ*ccmO*) results in the terminal formation of procarboxysomes (1-2 per cell) without disrupting other core elements of the carboxysome.[12] *ΔccmO* mutants exhibit a high-CO_2-requiring (HCR) phenotype and are unable to grow in air (0.04% CO_2), but can be fully rescued in elevated CO_2 (3% CO_2), allowing for study of the procarboxysome directly in high-CO_2 conditions.[12,62] By studying the procarboxysome, we can better understand carboxysome permeability during and after assembly as well as the procarboxysome as a potential evolutionary intermediate.

This work investigates the hypothesis that the carboxysome shell functions in maintaining a distinct redox state in the carboxysome. We track the dynamic redox changes within the cytosol, carboxysomes, and procarboxysomes in PCC 7002 during growth in air (0.04%) and 3% CO_2 conditions. To accomplish this, we implemented previously characterized roGFP2 fused with glutaredoxin (Grx1) to specifically probe changes in glutathione redox pools (*Figure 8*).[16,17,21,115] Using single-cell timelapse fluorescence microscopy under precisely controlled environmental conditions,[62,136] we were able to measure relative redox states at subcellular levels in PCC 7002. The work provides the first direct analysis of the redox state of the cyanobacterial cytoplasm, highlighting differences in the redox state within the carboxysome and showing that these differences are influenced by the carboxysome shell, particularly regarding the exclusion of thiol reductants, which has important implications for the functional role of the shell in regulating carboxysomal CA during biogenesis. The work also suggests that the permeability characteristics of the carboxysome increases in response to elevated CO_2 conditions reminiscent of shell-less, procarboxysome-like structures which appear to reflect a mechanism to adjust carboxysome permeability and provide insight into the evolutionary pressures leading to the encapsulation of Rubisco and its co-localization with CA. Furthermore, this study provides a window into how cyanobacteria may adapt to anthropogenetic increases in CO_2 levels.

4.3 Results

4.3.1 The Carboxysome is More Oxidized than the Cytosol and Procarboxysome

To probe subcellular cyanobacteria redox environments, we expressed Grx1-roGFP2[21] either as soluble protein to target the cytosol or as an C-terminal translational fusion with the large subunit of Rubisco (RbcL) to target the carboxysome/procarboxysome (*Figure 9a*). Live-cell fluorescence imaging showed that the roGFP signal morphology and localization for the carboxysome, cytosol, and procarboxysome was consistent with previous literature.[12,62,136] To assess unintentional disruption of the carboxysome function or shell structure, we tested strains for lack of a high-CO_2 requiring phenotype.[12,62,134] Addition of RbcL-Grx1-roGFP2 construct to the *ΔccmO* mutant did not disrupt the existing *ΔccmO* high-CO_2 requiring growth pattern[12,62] while all other strains had WT-like growth in both air and 3% CO_2 (*Figure 9b*). Overall, the roGFP-expressing strains appeared to be functionally comparable to WT and previously characterized *ΔccmO* mutant[12] with the growth pattern indicating RbcL-Grx1-roGFP2 addition did not disrupt normal carboxysome function or localization.

To confirm sensitivity of the roGFP probe, oxidizing (H_2O_2) and reducing agents (DTT) were added to bulk cultures and the fluorescence emission spectra of roGFP was measured, generating ratiometric readouts of the redox environment in each strain (*Figure 9*c). The cytosol showed consistent redox responses whereas the carboxysome was unresponsive to H_2O_2 addition, indicating either differences in shell permeability of the oxidizing and reducing agents or that the carboxysome was already fully oxidized.[17] No significant changes were measured in the procarboxysome with either redox agent, likely due to the preexisting reduced state from growing in 3% CO_2 limiting DTT impact and lower sensitivity to H_2O_2 as seen in the carboxysome (*Figure 9d*). Because the roGFP probe relies on a ratiometric measurement, the measurement of redox state is independent of roGFP concentration, subsequently allowing for comparison of strains with differing GFP signal intensity.[21] This feature of the roGFP system is supported by comparable redox readouts of the diffuse cytosol signal and the cytosolically exposed procarboxysome with high intensity puncta (*Figure 9a and e*). These results indicate that the roGFP system is functional at a bulk culture level and can be used to probe the redox poise of different subcellular regions.

To observe if subcellular redox states respond to [CO_2] changes, the redox state was measured in bulk cultures grown either in air or 3% CO_2 (*Figure 9e*). Carboxysomes were more oxidized than the cytosol in both air and 3% CO_2 (*Figure 9e*), however, unexpectedly, both the cytosol and carboxysomes became more reduced in 3% CO_2 conditions compared to their air-grown counterparts. Although previous work has probed the carboxysome environment independent of the cytosol,[16,17] this is the first time, to our knowledge, that the redox environment of these two subcellular regions have been directly compared. The procarboxysome redox state was not significantly different than the cytosol in 3% CO_2. This supports that the procarboxysome, with its non-existent shell,[12] is exposed to the cytosolic environment with a similar reduced redox environment. Furthermore, CO_2 concentration impacts redox environment in subcellular regions of PCC 7002.

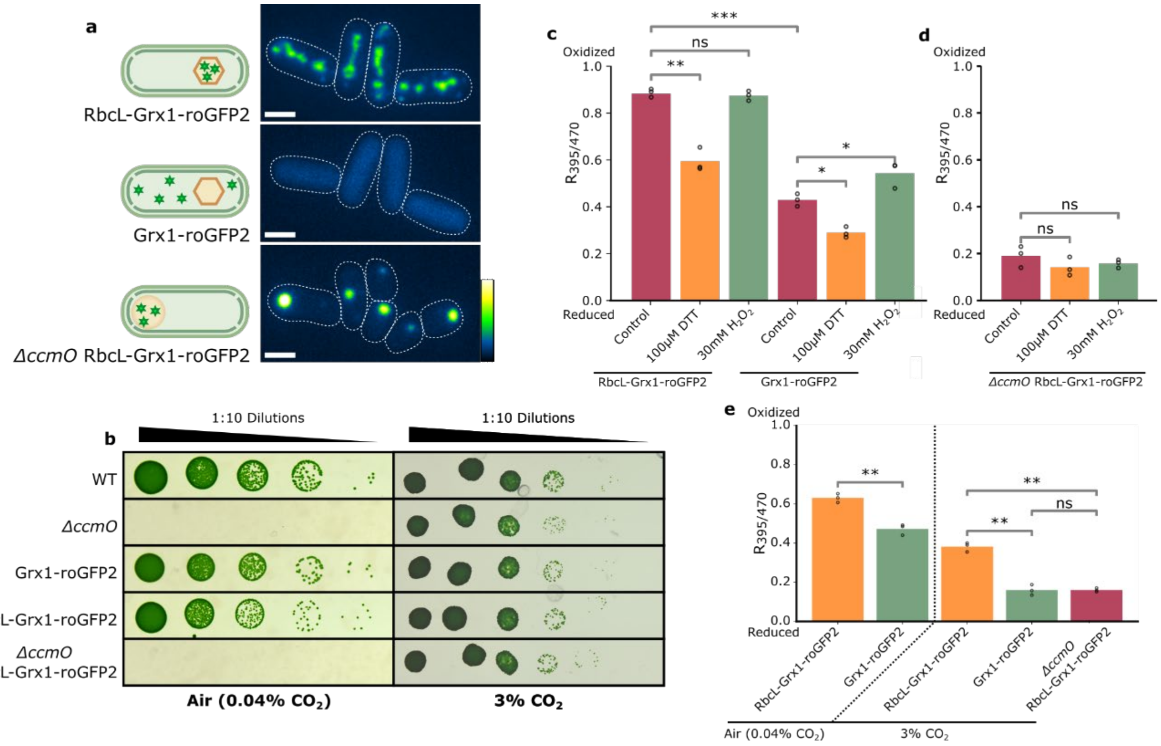

Figure 9. Grx1-roGFP2 Strains Characterization

(A) Fluorescence microscopy images of GFP intensity and localization in exponentially growing PCC 7002 strains growing in air (RbcL-Grx1-roGFP2 and Grx1-roGFP2) or growing in 3% CO_2 (*ΔccmO* RbcL-Grx1-roGFP2). Indicating the localization pattern of Grx1-roGFP2 to each of the subcellular regions of interest (carboxysome, cytosol, and procarboxysome, respectively). Color bar indicates GFP intensity. Scale bars represent 2μm. (B) Growth of strains in air (0.04% CO_2) and 3% CO_2 on 1% and 0.5% agar spot plates, respectively.[134] RoGFP strains showed either WT or *ΔccmO*-like growth. Ten-fold serial dilutions were plated and imaged after 72 hours. Images are representative of three biological replicates. (C and D) Spectrofluorometer measurements of strains grown in bulk liquid with 100 μM DTT and 30 mM H_2O_2 added 25s prior to measurement. (C) Grown in air, the carboxysome (RbcL-Grx1-roGFP) and the cytosol (Grx1-roGFP) are reduced when exposed to DTT whereas only the cytosol is oxidized with exposure to H_2O_2. (D) Grown in 3% CO_2, the procarboxysome (*ΔccmO* RbcL-Grx1-roGFP2) does not change redox state under either condition. (E) Spectrofluorometer measurements of strains grown in bulk liquid in air and 3% CO_2. The carboxysome (RbcL-Grx1-roGFP) is more oxidized than the cytosol (Grx1-roGFP) and procarboxysome (*ΔccmO* RbcL-Grx1-roGFP2) and both the cytosol and carboxysome become more reduced under 3% CO_2 than in air. No data is included for the procarboxysome redox state under air as *ΔccmO* RbcL-Grx1-roGFP2 cannot grow in air. Cultures were grown in respective CO_2 conditions for 24 hours prior to measurement. The results are representative of three biological replicates, n = 3, and data was analyzed by Student's t-test. *, $p < 0.05$; **, $p < 0.01$.

4.3.2 The Carboxysome Redox State Dynamically Responds to [CO2]

The bulk culture results revealed that the redox state in cyanobacteria responded to changes in [CO_2]. To investigate this response to 3% CO_2 at a finer scale, we used time-lapse microscopy to capture the redox dynamics of subcellular regions of PCC 7002. This approach allowed for simultaneous comparison of redox dynamics across a population as well as individual cell responses. In agreement with the bulk data, the carboxysome was consistently more oxidized than the cytosol and procarboxysome (*Figure 10a-e*). There is a general trend towards more reduced overtime in both the cytosol and carboxysome, whereas the procarboxysome exhibits an intermediate redox state, especially in air where they are unable to grow and may be experiencing photodamage. When the growing conditions were changed from air to 3% CO_2, there was an approximately 8-hour shift of the carboxysome to more reduced redox environment (*Figure 10f-j*). However, when reversed from 3% CO_2 back to air, the average redox shift of the carboxysome to a steady-state more oxidizing environment exhibited hysteresis and did not return to the same pre-high CO_2 redox state (*Figure 11*). These observations suggest that the redox state in the carboxysome is dynamic, but, at the average population level, did not explain what might drive these shifts.

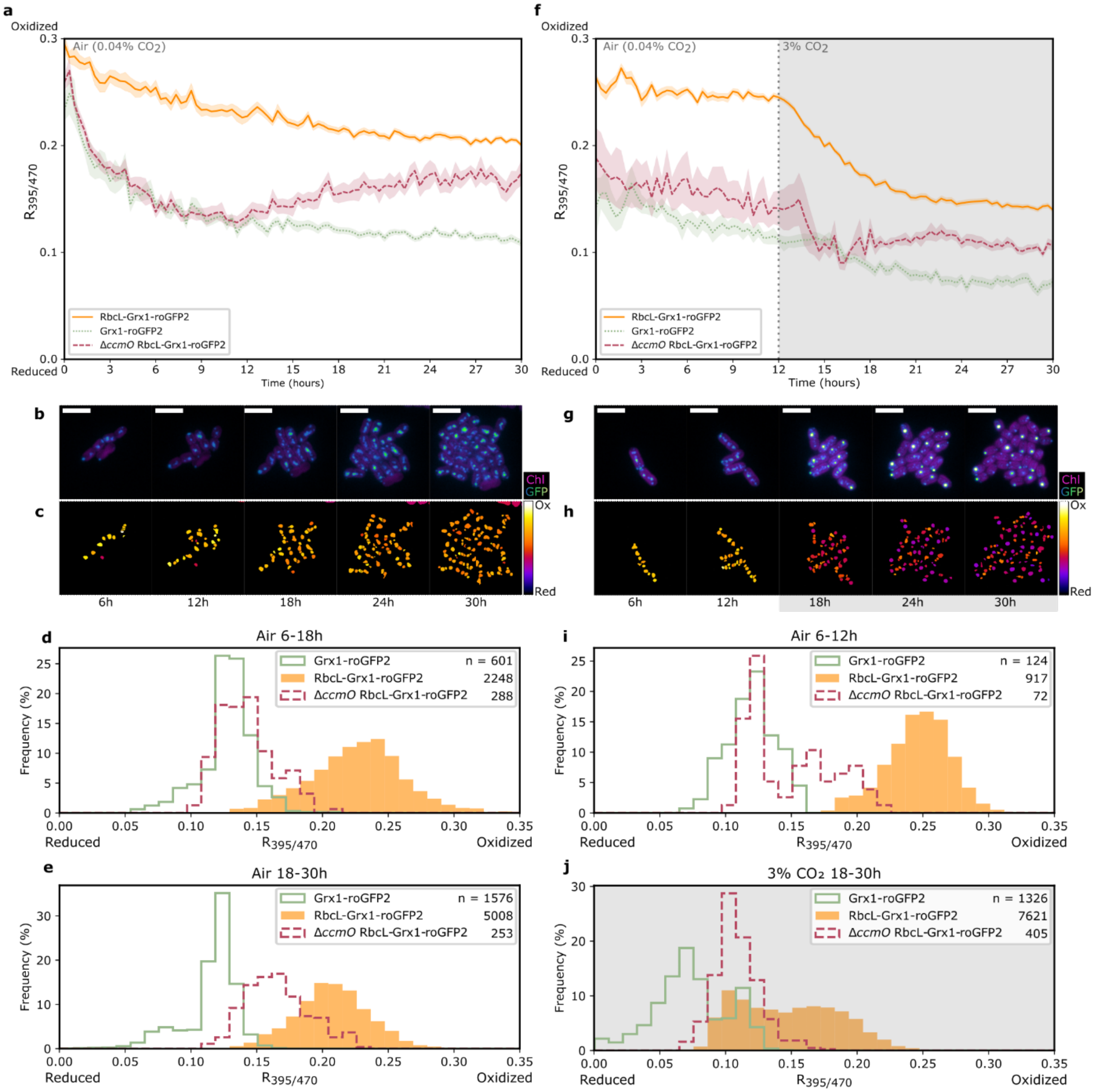

Figure 10. Redox state dynamics under low and low to high [CO_2].

Aggregated redox state from timelapse fluorescence microscopy of the carboxysome (RbcL-Grx1-roGFP2), procarboxysome (*ΔccmO* RbcL-Grx1-roGFP2), and cytosol (Grx1-roGFP2) over 30 hours of growth in (A-E) air or (F-J) 3% CO_2 conditions from hour 12 to 30. (B and G) GFP and chlorophyll fluorescence and (C and H) ratiometric images of representative carboxysomes over 30 hours of growth. Redox color bar spans from $R_{395/470}$ 0 to 0.3. Histograms represent frequency of redox state of each subcellular region when growing in air (D, E, I) or 3% CO_2 (J). Wildtype background fluorescence was subtracted from excitation intensity values at 395 nm and 470 nm (emission at 520 nm). Error bars represent standard error with n changing over the course of the experiment for each strain as a result of cell division (*Figure 12*). Scale bars represent 5µm. Representative data from three biological replicates.

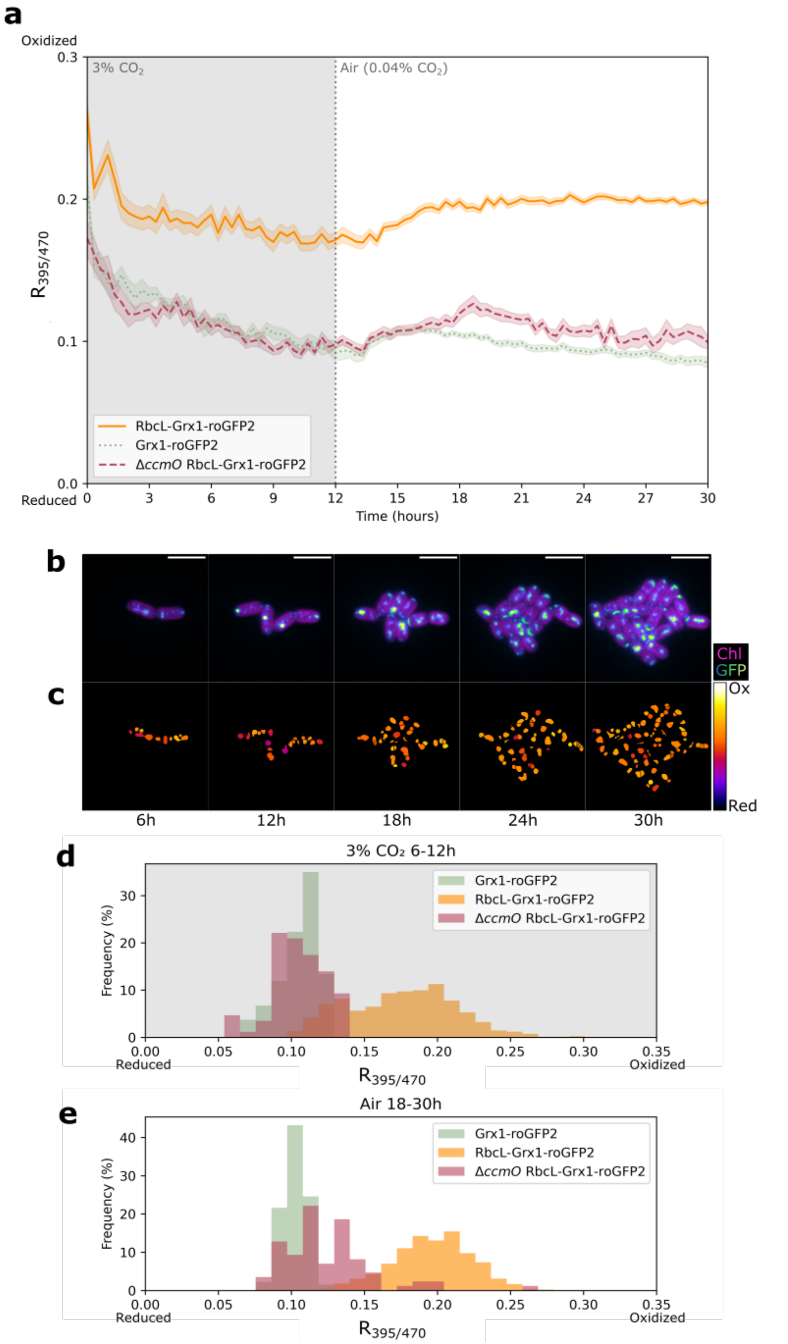

Figure 11. Redox state dynamics under high to low [CO$_2$].

(A) Aggregated redox state from timelapse fluorescence microscopy of the carboxysome (RbcL-Grx1-roGFP2), procarboxysome (*ΔccmO* RbcL-Grx1-roGFP2), and cytosol (Grx1-roGFP2) over 30 hours of growth in 3% CO$_2$ conditions from hour 0 to 12. (B) GFP and Chlorophyll fluorescence and (C) ratiometric images of representative carboxysomes over 30 hours of growth. Redox color bar spans from 0 to 0.3 and scale bars represent 5µm. Histograms represent frequency of redox state of each subcellular region when growing in (D) 3% CO$_2$ or (E) air. Wildtype background fluorescence was subtracted from excitation intensity values at 395 nm and 470 nm (emission at 520 nm). Error bars represent standard error with n changing over the course of the experiment (*Figure 12*). Representative data from three biological replicates.

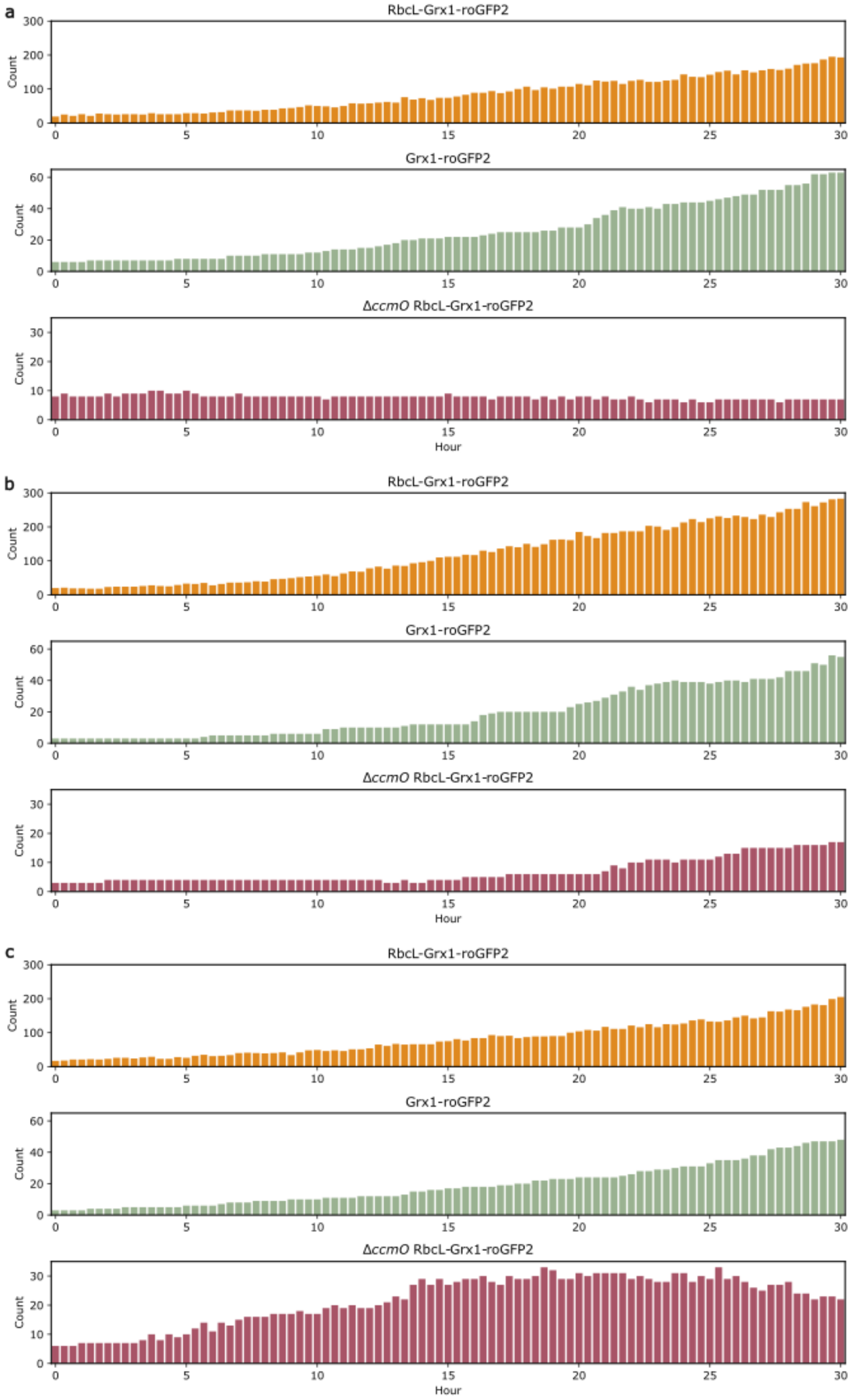

Figure 12. Counts for Timelapse Data

Timelapse fluorescence microscopy N-values of the carboxysome (RbcL-Grx1-roGFP2), procarboxysome (*ΔccmO* RbcL-Grx1-roGFP2), and cytosol (Grx1-roGFP2) over 30 hours of growth (A) from Figure 3a, (B) Figure 3j, and (C) Supplementary Figure 1. Minimum N is 3.

4.3.3 Procarboxysome-Like Structures Form in 3% CO_2

Further analysis of the population abundances of subcellular redox states revealed that in 3% CO_2 the carboxysomes in RbcL-Grx1-roGFP2 have a bimodal distribution (*Figure 10j*) which disappears when returned to air (*Figure 11*). In addition, we also noticed changes in the morphology of the fluorescent puncta labeling carboxysomes in RbcL-Grx1-roGFP2. When grown in 3% CO_2, there was formation of large, high intensity signal puncta with redox states comparable to the procarboxysome puncta in *ΔccmO* RbcL-Grx1-roGFP2 (*Figure 10, Figure 13*) which we refer to as procarboxysome-like structures. Given that the procarboxysome and procarboxysome-like structures share a similar redox state with the cytosol and that the procarboxysome does not have a shell,[12] we therefore concluded that the procarboxysome-like structure's shell must either have greater permeability to reducing agents, or an incomplete to absent shell exposing the Rubisco core to the cytosol. Once the cells were returned to air, the reduced state of these procarboxysome-like structures persisted for <6 hours before presumably being processed into carboxysomes (*Figure 11*).

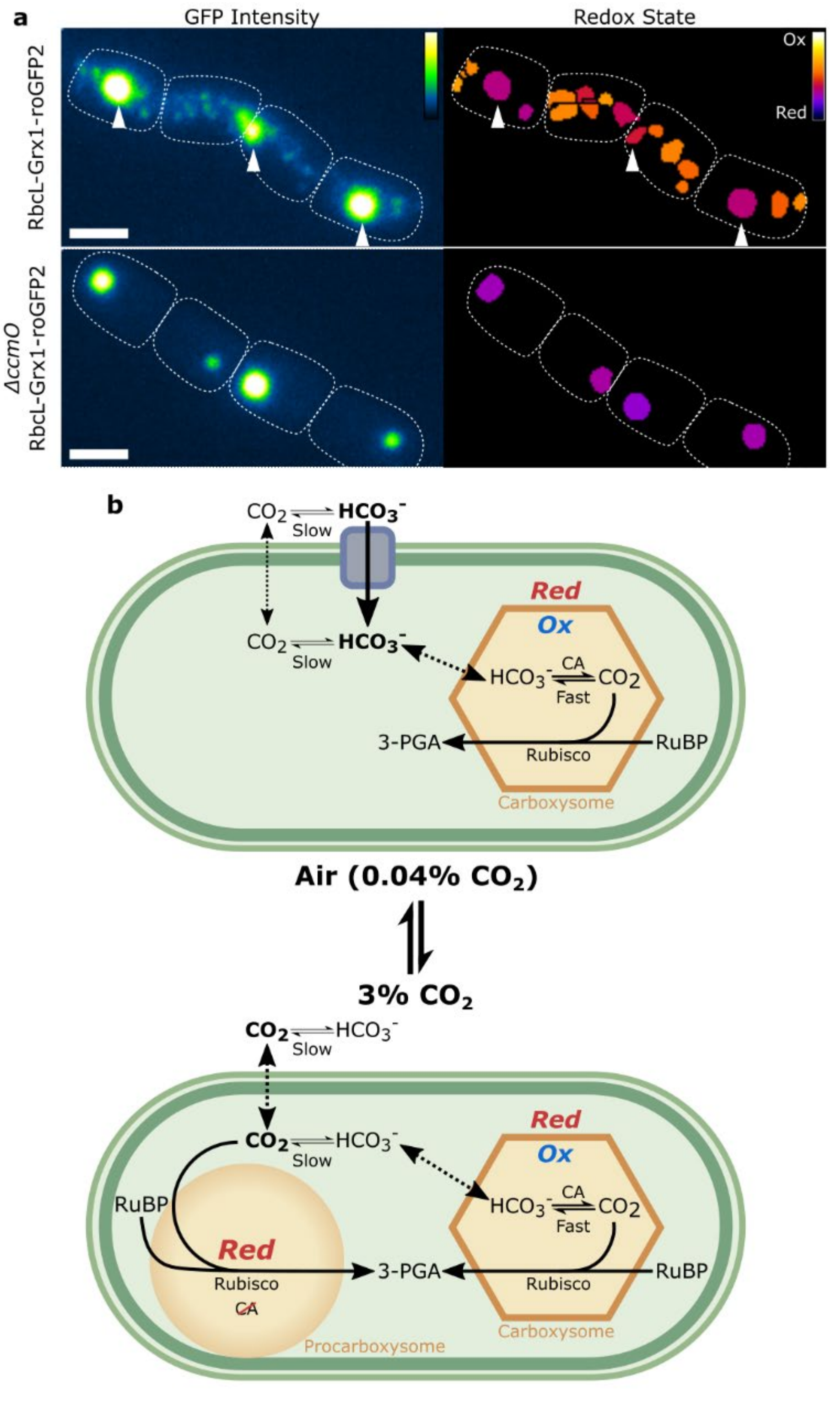

Figure 13. Procarboxysome-like Structures form in 3% CO_2

(A) GFP fluorescence microscopy showing that under 3% CO_2 there are procarboxysome-like puncta present in the carboxysome-labeled strain (RbcL-Grx1-roGFP). These procarboxysome-like structures have a similar size, fluorescent intensity, and redox state as procarboxysomes as seen in the procarboxysome-labeled strain (*ΔccmO* RbcL-Grx1-roGFP2). Color bars indicate GFP intensity and redox ratio (0-0.5) respectively and scale bars represent 2μm. (B) Proposed dynamic cyanobacterial CCM model under low and high CO_2 conditions. Under reducing environments carbonic anhydrase (CA) activity is thought to be inhibited,[65] and bicarbonate (HCO_3^-) transport downregulated as the pH shift in 3% CO_2 reduces [HCO_3^-].

4.4 Discussion

The function and permeability of the carboxysome shell has been an area of debate for over thirty years.[65,93] A leading hypothesis was that the shell served as a barrier to CO_2 and oxygen,[14,83,138] thus trapping CA-derived CO_2 with Rubisco and limiting Rubisco's side reaction with oxygen. However, recent computational work has suggested that CO_2 and O_2 diffusion is only minimally limited by the carboxysome shell.[15,84,85] Another possibility is that the shell serves to maintain a pH differential,[15,140,141] though modeling of diffusion argues that protons would be able to freely cross the shell and dissipate pH differences.[14,84,142] Consistent across all these studies is that larger molecules, such as the reactant RuBP, experience selective permeability across the shell pores with potential limitations to size passage and favorability to anions.[14,16,84,143] Additionally, one key chemical environmental difference of the carboxysome lumen has been identified prior and here, which is that the carboxysome is more oxidized than the cytosol.[16,17] When the shell is intact *in vitro*, reduction by reducing agents, such as TCEP[139] and DTT[65] occurs on the order of tens of minutes compared to carboxysomes with disrupted shells.[139] From this, we support the theory that the carboxysome shell serves as a barrier to redox compounds, such as glutathione and NADPH, in order to create a distinct internal oxidizing environment.[18]

The redox state of the carboxysome may serve as a chemical "switch" to indicate completion of the shell and activate its carbon-fixing role in the CCM.[16] Oxidation of CcmM promotes homodemixing, which is thought to create metabolite channels within the carboxysome and promote access for Rubisco repair proteins.[20] Disruption of the disulfide bonds in CcmM resulted in fewer, large, aberrant carboxysome structures with a HCR phenotype.[19] CA activity across several cyanobacteria species have also been shown to be activated by oxidizing conditions,[18,65,92] and, critical to CCM function, remain inactive when in a reducing environment such as the cytosol.[93] The exact mechanism of redox (in)activation of β-CA needs to be more deeply explored in both PCC 7002.[65] This theory begs the question, if the need of the carboxysome shell is removed, by being in high CO_2, is the carboxysome maintained as an oxidized environment?

This work represents the first exploration on the impact of $[CO_2]$ on the carboxysome redox environment. We found that the carboxysome redox state is dynamic and becomes more reduced in high CO_2. Whether this is a result of changes in the shell pores or shell structure, this overall shift indicates an adjustment of the carboxysome permeability to redox agents as the changing C_i pool affects global redox metabolism.

The dynamic redox state, exemplified by a shift of carboxysomes to a more reduced environment in high CO_2, brings up the unanswered question of what drives and maintains carboxysome oxidation state in the first place. While redox regulation has repeatedly been implicated in controlling γ-CA activity[18,92] and carboxysome aggregation via CcmM structure and binding affinity,[18–20] to our knowledge, there has not yet been an identified component of the carboxysome system capable of actively oxidizing the internal carboxysome environment during carboxysome formation. In other BMCs, the encapsulated reactions rely on the NAD(P)H electrochemical cycle. In these BMCs either reductases are co-encapsulated or FeS clusters are thought to occupy shell pores to transfer elections across the BMC shells.[49,144] These mechanisms also support that the BMC shell is a barrier to redox agents such as NADH. For the carboxysome, we speculate that the diffusion of oxygen and potentially H_2O_2 across the shell gradually oxidizes the trapped glutathione pool in the carboxysome lumen, as seen in purified α-carboxysomes.[17] This pool cannot be reduced due to shell impermeability to reducing agents and protein reductases.

None of the known carboxysome components have been reported to possess enzymatic oxidizing capability. It is possible that the presence of the roGFP sensor alters the redox environment in which it is located and artificially creates an oxidized carboxysomal environment but, given the evidence for redox regulation of CAs and CcmM,[18–20] there is biologically based functional support for the carboxysome being an oxidized environment. As this study uses a glutaredoxin to specifically track the glutathione pool, further work targeting other forms of redox activity in the carboxysome is warranted, such as other redox pools (NADPH) and reductase-dependent methionine oxidation.[145] Other redox probes could be implemented but, given the unknown permeability of the carboxysome shell to chemical probes, such as SNAP dyes,[16] this nanometer-scale subcellular region[146] remains challenging to study.

There was a consistent shift in redox environment the first 2-3 hours, likely a consequence of the cells adjusting to the environmental conditions of the microscope and therefore was disregarded in the CO_2 modulation data.[134] However, this shift still has intriguing implications. Since the state of the carboxysome appears to start out oxidized then trend towards a more reduced steady state over time (*Figure 10, Figure 11*), there may be some adjustment of the redox state of the carboxysomal glutathione pool. There is potential for modifiable permeability of the carboxysome to redox agents, perhaps through the less explored shell proteins with larger pores such as CcmP.[14] The shell is not completely impermeable to reducing agents, such as DTT (*Figure **9c***) or TCEP[17,139] and it is unclear when exposed to H_2O_2, if the shell is a diffusion barrier, the cytosol serves as a buffer against this oxidizing agent, or if the carboxysome is already fully oxidized. For what might be driving the trend towards reduction, we speculate that the formation of aggregated cells may affect gas exchange or other physiologically significant parameters leading to a more reduced condition, but this will need a more thorough analysis as part of a future study. Further work is needed to explore carboxysome redox dynamics, shell permeability to redox agents, and processes driving carboxysome oxidation.

Discovery of reduced procarboxysome-like structures in high CO_2 conditions provides both insights into carboxysome evolution and function and opens new questions. Unique to the work presented here, we leveraged the terminal procarboxysomes in *ΔccmO* mutants to directly compare similarities in morphology and redox state of the procarboxysome-like structures forming high [CO_2] in non-knockout cells. The procarboxysome and procarboxysome-like structures share a reduced state, like the cytosol, which suggests the shell is either incomplete or missing (*Figure* 13). Recent work studying *in vitro* α-carboxysomes found that carboxysomes were larger and shell proteins had increased fluidity in reducing conditions.[147] Additional experiments, such as thin section TEM, tracking shell protein localization via GFP,[12,75] and FRAP of shell proteins to determine mobility[147] would be needed to confirm the composition or complete absence of the carboxysome shell in these procarboxysome-like structures. Given there is not an impact on growth by the roGFP strains, it is unlikely that the procarboxysome-like structures are aberrant Rubisco aggregations.[97] Increased permeability or loss of the carboxysome shell would result in moderate increase of photorespiration rates,[109,148] but given previous studies with carboxysome mutants were conducted in high CO_2, it is difficult to determine if these WT photorespiration rates were elevated as well if procarboxysome-like structures were present under these conditions. Future work is needed to explore the details of these dynamics.

Notably, after six hours of being returned to air, reduced procarboxysome-like structures appear to either be processed into oxidizing carboxysomes or diluted by the formation of *de novo* carboxysomes (*Figure 11*). The data presented here is insufficient to determine between whether this process is driven by changes in carboxysome protein expression levels or structural alternations in response to redox shifts.[19,20,147] There is a lack of agreement in the literature on if the expression of carboxysomal proteins in high CO_2 conditions is increased,[146] decreased,[149] or remains the same.[150] While additional RbcL from the expression of the RbcL-Grx1-roGFP2 construct under its native promoter[62] may also alter carboxysome formation, we do not note any growth rate reduction that would be indicative of excess protein expression and aggregation (*Figure 9**b***).[97] Mutation of the disulfide bonds in CcmM in *Synechococcus* sp. PCC 7942 resulted in formation of large, HCR carboxysomes.[19] This suggests the mechanism that reduction of CcmM may alter carboxysome condensation and shell permeability leading to the larger, more permeable procarboxysome-like structures observed in high CO_2, and is a reversable process when CcmM becomes oxidized again.

High CO_2-specific formation of procarboxysome-like structures could point to the procarboxysome as an evolutionary intermediate during changing CO_2 conditions.[31,140] Pioneering studies on *Synechococcus* sp. PCC 7942[151] and *Synechocystis* sp. PCC 6803[146,150] found there were less carboxysomes when grown in increased [CO_2], and in *Synechococcus* UTEX 625 grown in 5% CO_2, a subset of carboxysomes were larger and irregularly shaped,[152] indicating that formation of procarboxysome-like structures in high [CO_2] is not a strain specific phenomena.

We hypothesize that the carboxysome shell serves as a diffusion barrier to redox agents, such as glutathione, in order to maintain an oxidizing environment in air (*Figure 13b*).[18] In high CO_2, a procarboxysome-like structure with greater permeability to the cytosol would allow Rubisco to remain exposed to the high cytosolic CO_2 without needing the CCM and minimal to absent CA activity.[153,154] This work paves the way for a more detailed understanding of carboxysome formation, shell permeability, and redox regulation of carbon fixation. By better understanding these processes, we can more effectively implement the carboxysome for applications in biotechnology as well as guide research on the pressures driving carboxysome evolution.

Chapter 5 - Machine Learning Models for Segmentation and Classification of Cyanobacterial Cells

This chapter was adapted from:

Huffine, C. A., Maas, Z. L., Avramov, A., Brininger, C., Cameron, J. C., Tay, J.W. (2025). Machine learning models for segmentation and classification of cyanobacterial cells. *Photosynth Res* **163**, 16

https://doi.org/10.1007/s11120-025-01140-x

5.1 Summary

Timelapse microscopy has recently been employed to study the metabolism and physiology of cyanobacteria at the single-cell level. However, the identification of individual cells in brightfield images remains a significant challenge. Traditional intensity-based segmentation algorithms perform poorly when identifying individual cells in dense colonies due to a lack of contrast between neighboring cells. Here, we describe a newly developed software package called Cypose which uses machine learning (ML) models to solve two specific tasks: segmentation of individual cyanobacterial cells, and classification of cellular phenotypes. The segmentation models are based on the Cellpose framework, while classification is performed using a convolutional neural network named Cyclass. To our knowledge, these are the first developed ML-based models for cyanobacteria segmentation and classification. When compared to other methods, our segmentation models showed improved performance and were able to segment cells with varied morphological phenotypes, as well as differentiate between live and lysed cells. We also found that our models were robust to imaging artifacts, such as dust and cell debris. Additionally, the classification model was able to identify different cellular phenotypes using only images as input. Together, these models improve cell segmentation accuracy and enable high-throughput analysis of dense cyanobacterial colonies and filamentous cyanobacteria.

5.2 Introduction

Timelapse microscopy, combined with the use of fluorescent labeling and sensing, allows molecular processes to be observed in individual cells at a sub-cellular level. Recent techniques have shown that cyanobacteria, a model organism for the study of photosynthetic processes, can be filmed over extended periods of time[155,134,136]. The resolution of microscopy datasets has led to discoveries that were not previously observed in bulk culture experiments[156,157] such as the regulation of photosynthetic processes[134] and organelle development and positioning[158,159,62].

Due to the large number of individual cells that can be captured in a single image, computational pipelines are often used to obtain single-cell data from microscopy datasets. However, the identification (or segmentation) of individual cells in the resulting images remains the main bottleneck in these pipelines. Cell segmentation is typically performed using intensity-thresholding, where every pixel above a set threshold is identified as being part of a cell[136,160,161]. Intensity-thresholding is popular as it is a relatively simple technique that works well if cells are fluorescently labeled, so that the fluorescence signal is much brighter compared to the background.

Cyanobacteria produce photosynthetic pigments which are autoflourescent. While this might initially seem advantageous, the fluorescence signal is typically non-uniform throughout the cell. Additionally, the fluorescence intensity changes depending on the cell’s photosynthetic capacity, which can lead to issues when choosing a threshold intensity. Together, these issues have meant that using photosynthetic fluorescence to identify individual cells is undesirable. Alternatively, fluorescent proteins or dyes could be used to mark the cells. However, the presence of the autofluorescence once again complicates matters since most microscopes are limited to imaging ~3 fluorescence channels due to spectral overlap[162,163]. Requiring a fluorescent label would limit one’s ability to label other molecules or organelles of interest. It is therefore advantageous to develop segmentation algorithms which use the brightfield image, which is generated by light transmitted through the sample, to remove the need for further labeling.

We previously developed intensity-thresholding algorithms to identify cyanobacteria in brightfield images. However, these images are difficult to segment because there is little contrast between the cell interior and the background[164]. The problem is exacerbated when cells grow in dense colonies or for filamentous strains of cyanobacteria as cell boundaries become even less pronounced (*Figure 14**,** Figure 15*).

Here, we describe the development of a family of machine learning models, collectively named Cypose, to improve the segmentation of individual cyanobacterial cells. Compared to intensity-based thresholding, machine learning segmentation models can learn to identify cells using complex hierarchical image features and have been shown to work well even without fluorescent labeling[165,166]. Additionally, we describe a method to train a classification model, using a convolutional neural network (CNN) named Cyclass, to perform image-based identification of different cellular phenotypes. We demonstrate that the Cyclass model can be used to identify different cellular phenotypes using only image data as input. We demonstrate the usefulness of both Cypose and Cyclass by showing that these models can be used together to initially segment cyanobacterial cells in dense colonies, then classify different cellular phenotypes in a timelapse video. This methodology could be helpful in studies of mixed bacterial species by enabling multiple genotypes/phenotypes to be imaged simultaneously or to distinguish individual species in studies containing mixed populations.

5.3 Results

5.3.1 Development of the Cypose cyanobacterial segmentation models

Our Cypose segmentation models are fine-tuned models based on the Cellpose base models[167]. Cellpose consists of a U-Net like convolutional neural network, which transforms an image into a series of spatial gradients. These gradients are then used to identify and label individual cells in an image.

In initial testing, we found that the base Cellpose cytoplasmic models (cyto2[168] and cyto3[169]) showed poor performance when segmenting brightfield images of cyanobacteria (*Figure 15*). This is likely because these models were trained on cytoplasmic images of eukaryotic cells[167], which have different phenotypic and morphological features compared to cyanobacteria. We also tested a separate segmentation model, bact-phase-omni, from the Omnipose package[170] (which itself is derived from Cellpose), which was trained on images of bacteria. However, we found that this model appeared to perform worse than Cellpose for segmentation, likely because it was trained primarily on phase contrast images.

To achieve higher quality segmentation on cyanobacteria, we trained a family of specialist models. Three different models were trained: (1) cypose-7002 and (2) cypose-7002-scratch were trained on images of *Synechococcus sp.* PCC 7002 (hereafter PCC 7002), which are unicellular, while (3) cypose-33047 was trained on images of *Anabaena sp.* ATCC 33047 (hereafter ATCC 33047), which are filamentous. Both cypose-7002 and cypose-33047 were fine-tuned from the Cellpose cyto2 base model, while cypose-7002-scratch was trained from scratch on the Cellpose architecture. Details of the training and datasets used are provided in the methods section below. We note that our models are based on the Cellpose 2.0 cyto2 model rather than the recently released

Cellpose 3.0 cyto3 model, as the latter was unavailable at the start of this work. However, we have included comparisons of our new models with cyto3.

5.3.2 Segmentation of *Synechococcus* PCC 7002 cells

We used the cypose-7002 model to segment timelapse videos of PCC 7002 capturing single cells developing into colonies. A representative image showing a dense colony from a late frame taken from the benchmark movie is shown in *Figure 15a*. Masks generated by our cypose-7002 model, the Cellpose and Omnipose models, as well as our previously described intensity-thresholding algorithm are shown for comparison**.** We note that while the intensity-thresholding algorithm performed well, segmentation errors tended to develop within individual cells, as well as between cells after 3 doublings (*Figure 14*). However, our new Cypose model performed well over long timelapse movies. The model begins to fail when the colonies grow so dense that the cells start to overlap.

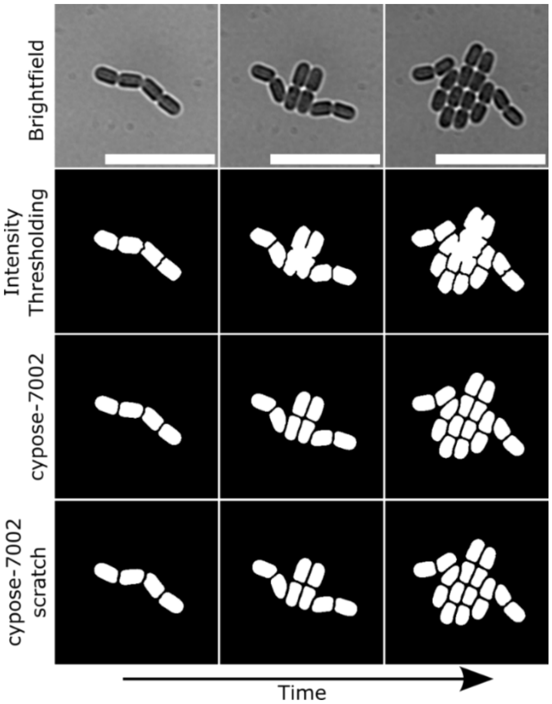

Figure 14. PCC 7002 Segmentation Comparison

Comparison of segmentation of 7002 between intensity-based thresholding, cypose-7002 and cypose-7002-scratch. Scale bars indicate 15 µm.

To assess the accuracy of our model, we compared the mask generated by each method to our ground-truth masks pixel-by-pixel by calculating the Intersection over Union (IoU) score, as well as the typical precision and recall scores for each method,[171] as shown in *Table 6* and *Appendix Figure 1*. These scores showed that cypose-7002 outperforms other models across nearly all metrics. The cypose-7002 model appears to perform slightly worse compared to the intensity-based approach. However, as detailed in the methods, the benchmark dataset was generated using the intensity-based approach so there is likely a bias towards this approach.

We note that while these pixel-based metrics are typically reported when comparing cell segmentation models, they do not accurately capture inaccuracies, such as over- and under-segmentation, in the resulting objects. For example, we observed that single cells were often split into two distinct objects by both cyto2, cyto3, and bact-phase-omni. In this case, the error could be as small as a single-pixel wide line, which means that the number of erroneous pixels were much smaller compared to the number of pixels in both cells, the precision and recall scores appear high.

To obtain a more accurate analysis, we developed code to recognize errors in the identified objects. We identified four errors: (1) oversegmentation (2) undersegmentation, (3) false positives, and (4) false negatives. We found that the cypose-7002 model resulted in a much lower number of errors compared to all other models, including the intensity-based approach (*Table 6, Figure 15b and c, Appendix Figure 1*). On the benchmark movie, cypose-7002 had 10% of the total number of segmentation errors compared to the other tested models. Additionally, we found that cypose-7002 only generated two false negatives, compared to the hundreds generated by the other models. We note that while the number of errors in a frame increases slightly over the duration of the movie as colonies become denser (*Figure 15c*), this model remains more accurate than the other tested models.

During the creation of the training dataset, lysed cells were not annotated. Consequently, we found that our cypose-7002 model was able to differentiate living and lysed cells (*Figure 15d*). Additionally, to test the breadth of the model's capability to segment cells with different morphologies, we applied the model to images of *Synechococcus elongatus* sp. PCC 7942 (hereafter PCC 7942), two genetic mutants of PCC 7002 with markedly different phenotypes, as well as images of PCC 7002 growing in a microfluidic device (*Figure 15e*). In the latter, plastic posts in the microfluidic chamber are visible in brightfield. In all cases, we found that our new model correctly segmented cells, while ignoring other artifacts such as the posts.

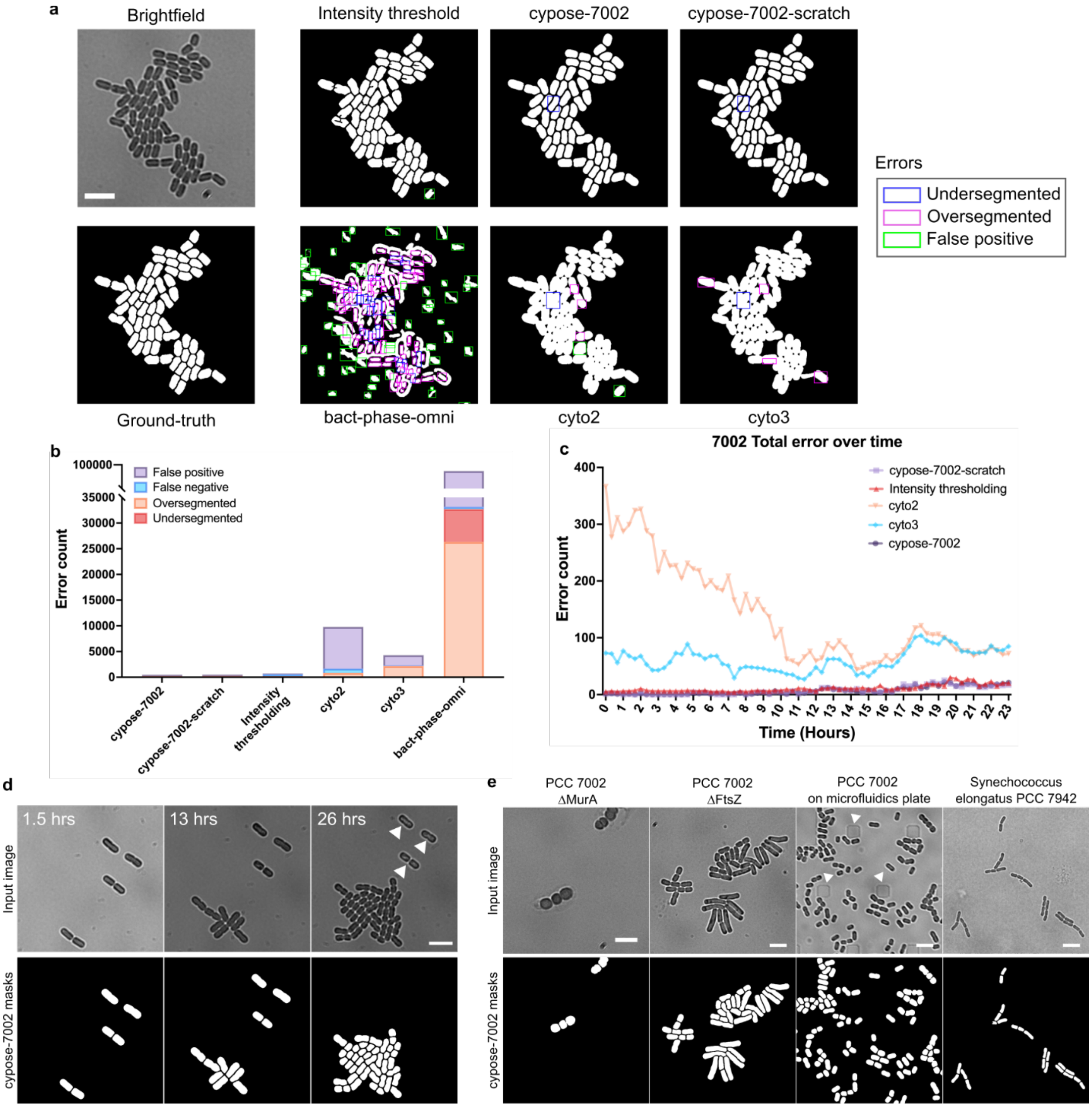

Figure 15. Cypose-7002 Model

(a) Representative images of PCC 7002 showing the input image, ground-truth, and resulting masks from the intensity-thresholding algorithm and the various machine learning models. Errors in each mask are highlighted by a box: undersegmentation in blue, oversegmentation in magenta, and false positives (additional objects) in green. Scale bar indicates 5 µm. (b) Bar plot showing the total number of segmentation errors over the entire benchmark movie. (c) Plot showing the number of total errors at each frame. The bact-phase-omni model gave a total error over two orders of magnitude higher and is excluded for clarity (data shown in *Appendix Figure 1*). (d) Representative frames from a movie showing that the cypose-7002 model was able to identify and ignore dead cells (indicated by white arrows), which were identified by their lack of growth during the movie. Scale bars indicate 5 µm. (e) Representative frames showing the model's ability to identify different species/phenotypes and under different imaging conditions. The white arrows indicate posts of the microfluidic plate. Scale bars indicate 5 µm.

5.3.3 Comparison of scratch-trained and fine-tuned models

As previously mentioned, our cypose-7002 model was fine-tuned from the pretrained cyto2 model. The cyto2 model was trained on a diverse training set, primarily comprising of images of eukaryotic cells, with additional non-cell images containing repeating patterns, such as shells and rocks. Since no images of cyanobacteria existed in the cyto2 dataset, we wanted to test if a segmentation model trained from scratch only on cyanobacterial images would perform better compared to the fine-tuned cypose-7002 model.

The cypose-7002-scratch model was trained from scratch using the Cellpose architecture. This model was trained on 3.5x more cell images compared to cypose-7002. To account for different cell morphologies, our dataset included various PCC 7002 mutants which showed morphological deviations from WT cells (e.g., cell swelling and elongation) similar to those shown in *Figure 15e* (note that these images were not shown to the fine-tuned cypose-7002 model). Results from this segmentation model are shown in *Figure 15a.* Benchmark metrics were also calculated and are shown in *Table 6*.

Overall, we found that the scratch-trained model provided very similar results to the fine-tuned cypose-7002 model. However, training from scratch was both labor intensive (since more training data needed to be manually curated) and required substantially more training than fine-tuning. Considering the similarity in performance, we concluded that training from scratch did not offer notable advantages.

5.3.4 Segmentation of filamentous cyanobacterial strains

We fine-tuned a second model (cypose-33047) to segment filamentous *Anabaena sp.* ATCC 33047 (hereafter ATCC 33047). This strain is challenging to segment as it forms interconnected structures with minimal intensity differences between neighboring cells. Additionally, ATCC 33047 differentiates into three morphologically and phenotypically distinct cell types: photosynthetic vegetative cells, specialized nitrogen-fixing heterocysts, which have no or little photosynthetic pigments[172], and akinetes[173], which are large, spore-like cells formed during low nutrient conditions. To increase the distinction between neighboring cells and to account for the different cell types, the cypose-33047 model was trained on images of both the brightfield and the chlorophyll fluorescence channels.

The resulting masks are shown in *Figure 16a*. We found that our fine-tuned model provided significant improvement when segmenting filamentous cyanobacteria compared to the Cellpose and Omnipose models, and to the intensity-thresholding method (*Table 6, Figure 16b and c, Appendix Figure 3, Appendix Figure 4*). As before, we used a timelapse movie with cells starting from small filaments as a benchmark. To capture a variety of conditions, we selected three distinct temporal subsets of this movie for testing, capturing variable cell densities at the start, middle, and end. We found that the cypose-33047 model excelled in early and mid-movie frames, with cyto3 performing better in later frames. This suggests that our model could be improved by increasing the number of images showing dense filaments in our training dataset.

More detailed analysis of the errors showed that the majority (52%, *Table 6*) of errors in cypose-33047 were due to under-segmentation (*Figure 16b, Appendix Figure 3*). However, our model still showed better results when compared to the next best model, cyto3 (cyto3 had 688 under-segmentation errors compared to 81 for cypose-33047). We also found that our model was more accurate at segmenting akinetes than the other tested models and was resilient to other imaging artifacts (*Figure 17*).

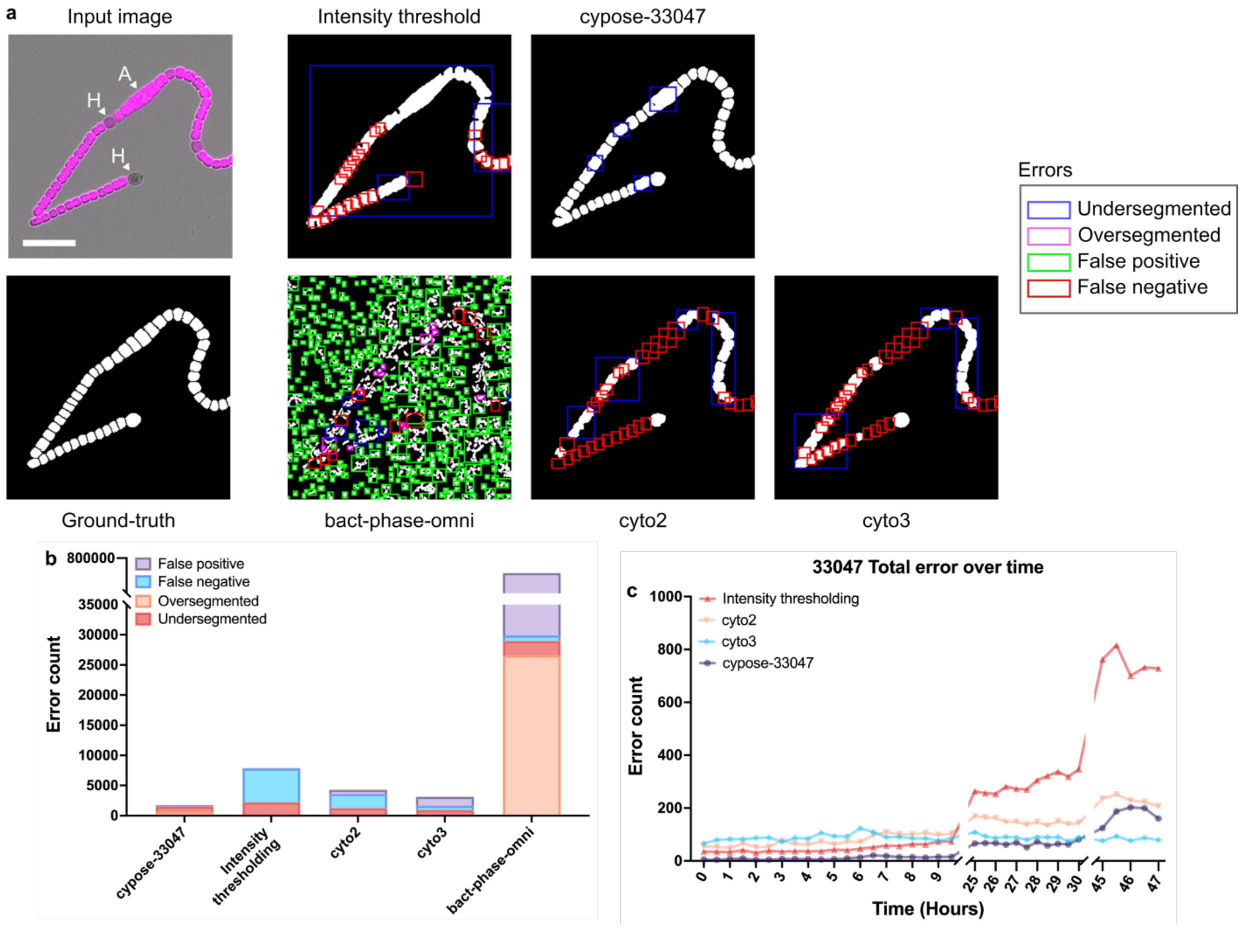

Figure 16. Cypose-33047 Model

(a) Representative images of ATCC 33047 showing the input image, ground-truth, and resulting masks from the intensity-thresholding algorithm and the various machine learning models. The input image is composed of two channels: brightfield (grayscale) and chlorophyll fluorescence (magenta). The heterocysts (labeled H) showed reduced or no chlorophyll fluorescence. An akinete cell is present in the image (labeled A). Errors in each mask are highlighted by a box: undersegmentation in blue, oversegmentation in magenta, false positives (additional objects) in green, and false negatives (missing objects) in red. Scale bar indicates 20 µm. (b) Bar plot showing the total number of segmentation errors. (c) Plot showing the total number of errors at each frame of the benchmark movie. The line for bact-phase-omni was excluded for clarity (data shown in *Appendix Figure 3*).

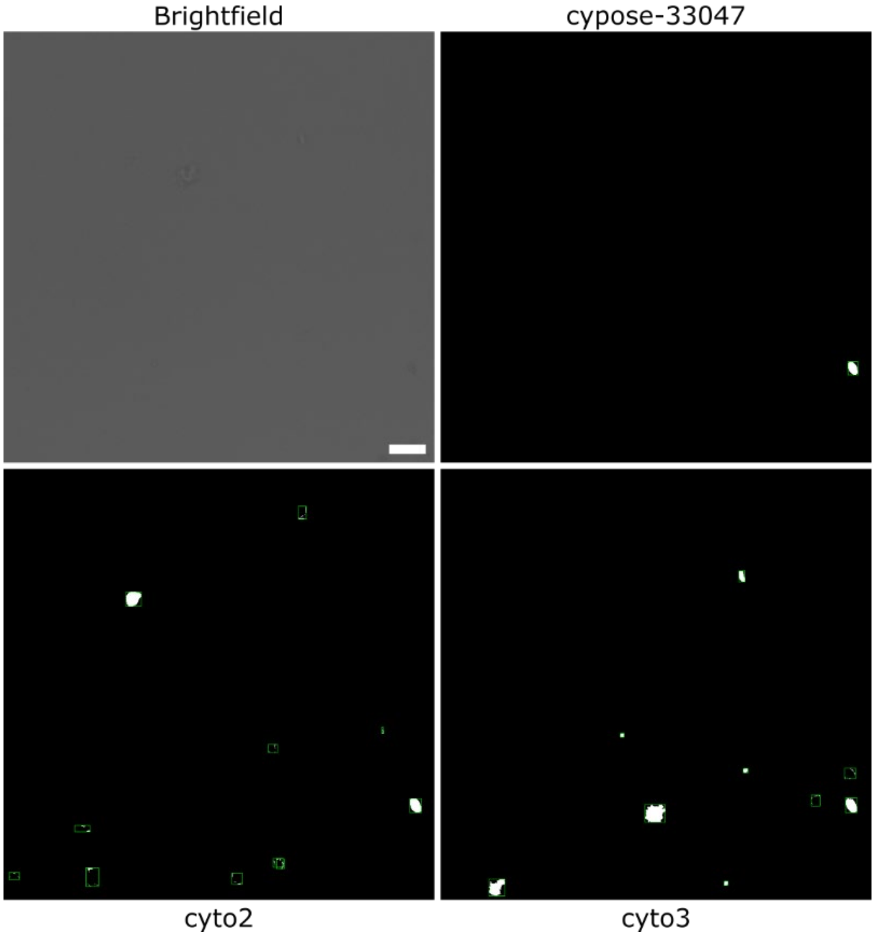

Figure 17. Debris segmentation comparison

ATCC 33047 segmentation comparisons showing false positive segmentation of debris and background in an area without cells present. False positives (additional objects) errors in each mask are highlighted by a green box.

Table 6. Segmentation Models Comparisons

Performance of segmentation models calculated by comparing the generated masks with ground-truth masks pixel-by-pixel or by identifying errors in individual objects.

Organism	**Model**	**Pixel-based performance**			**Object-based performance**				
		IoU[a]	**Precision[b]**	**Recall[c]**	**Over-segmented**	**Under-segmented**	**False Negative**	**False Positive**	**Total**
PCC 7002	**cypose-7002**	**0.929**	**0.953**	**0.973**	**59**	**153**	**2**	**274**	**488**
	cypose-scratch	**0.921**	**0.944**	**0.974**	**43**	**191**	**10**	**256**	**500**
	cypose-33047	0.852	0.897	0.944	1900	4	57	863	2824
	cyto3	0.784	0.949	0.818	2175	12	128	1985	4300
	cyto2	0.597	0.853	0.666	834	18	829	8107	9788
	bact-phase-omni	0.120	0.437	0.142	26364	6374	432	58982	92152
	Intensity thresholding	0.951	0.966	0.984	33	175	389	151	748
ATCC 33047	**cypose-33047**	**0.875**	**0.849**	**0.757**	**629**	**934**	**81**	**140**	**1784**
	cypose-7002	0.866	0.899	0.959	30	3119	627	61	3837
	cyto3	0.732	0.905	0.793	164	809	688	1485	3146
	cyto2	0.642	0.774	0.790	72	1199	2325	703	4299
	bact-phase-omni	0.040	0.374	0.043	26605	2373	904	727798	757680
	Intensity thresholding	0.659	0.798	0.790	33	2201	5597	46	7877

[a]IoU – ratio of the intersect over union of the predicted and ground truth object bounding boxes. [b]Precision - ratio of true positive predictions to total number of predictions. [c]Recall - ratio of true positive predictions to total ground truth instances[171]. For these pixel-based performance metrics, a value closer to 1 is better.

5.3.5 Development of Cyclass to classify cellular phenotypes in a single image

Microscopy-based assays allows individual cellular phenotypes to be observed, for example in microbiome[174] or competition assays[175,176] or to probe population heterogeneity[62,177]. Typically, cellular phenotypes are identified in post-processing by filtering using physical properties, such as size or growth rate, or by measuring the intensity of labelling with different fluorophores. However, developing these computational filters can be challenging if the phenotypes are not significantly different from each other or if a phenotype is not easily described by a single parameter.

Here, we describe a method to train a convolutional neural network (CNN) based classifier, named Cyclass (*Figure 19*), to identify different cellular phenotypes in an image. By using a CNN, we were able to train a model to recognize different phenotypes directly from input images without the need for explicitly designing filters. We note that, unlike the Cypose segmentation models, classifier models are not easily generalized to different imaging conditions (e.g., number of available channels (*Figure 18*)) or different phenotypes. Thus, it is likely that new classifier models must be trained for different applications. The Cyclass framework provided in the codebase enables users to train their own models using images consisting of up to 6 different channels.

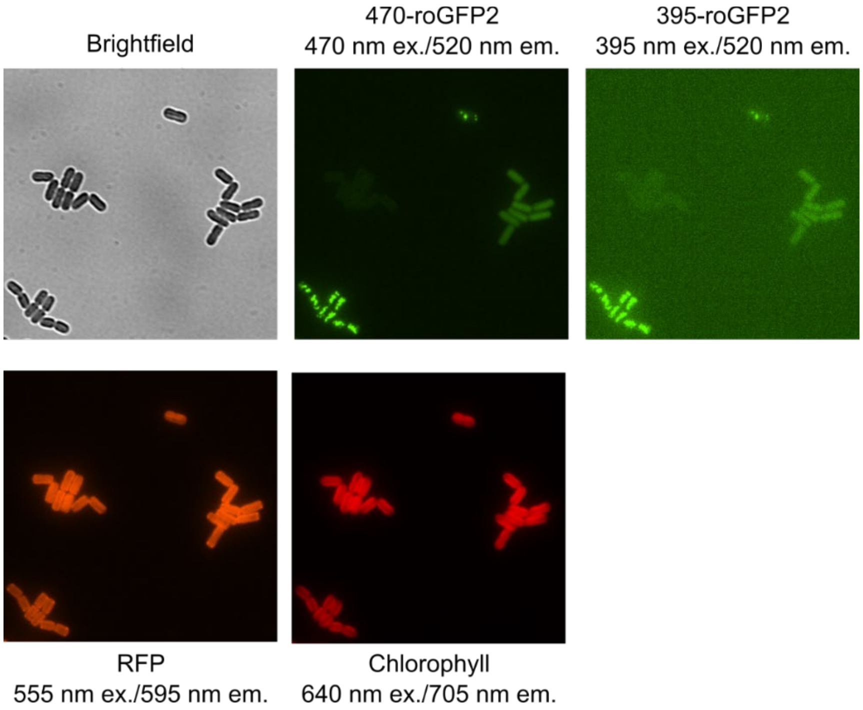

Figure 18. Classifier Training Channels

All channels of the input image used to train the classifier. The channels were combined into a single matrix and used as input to the classifier. Note that the roGFP2 fluorophore is a ratiometric redox sensor[26].

As proof-of-principle, we trained a mode, named cyclass-7002, to classify four cell types of co-cultured PCC 7002 mutants with differently localized GFP: Strain 1 had GFP freely diffused throughout the cytosol, Strain 2 had GFP localized to the carboxysome, Strain 3 had GFP localized to the procarboxysome, and the WT strain had no GFP. Details of each strain are available elsewhere[48].

A representative image showing the result of cyclass-7002 is shown in *Figure 19b***.** To visualize the results, we used the classification values from the spreadsheet to color the cell mask. To quantify the accuracy of the classification, we calculated the overall IoU (0.919), precision (0.958), and recall (0.958) scores. The confusion matrix was also calculated and is shown in Fig. 3c. When analyzing the error, we found that they primarily occurred in cells bordering merging colonies or in cells which exhibited intermediate phenotypes (*Figure 19d*). This is likely because the input image size of 32x32 is larger than a single cell, and information from neighboring cells could affect the resulting classification.

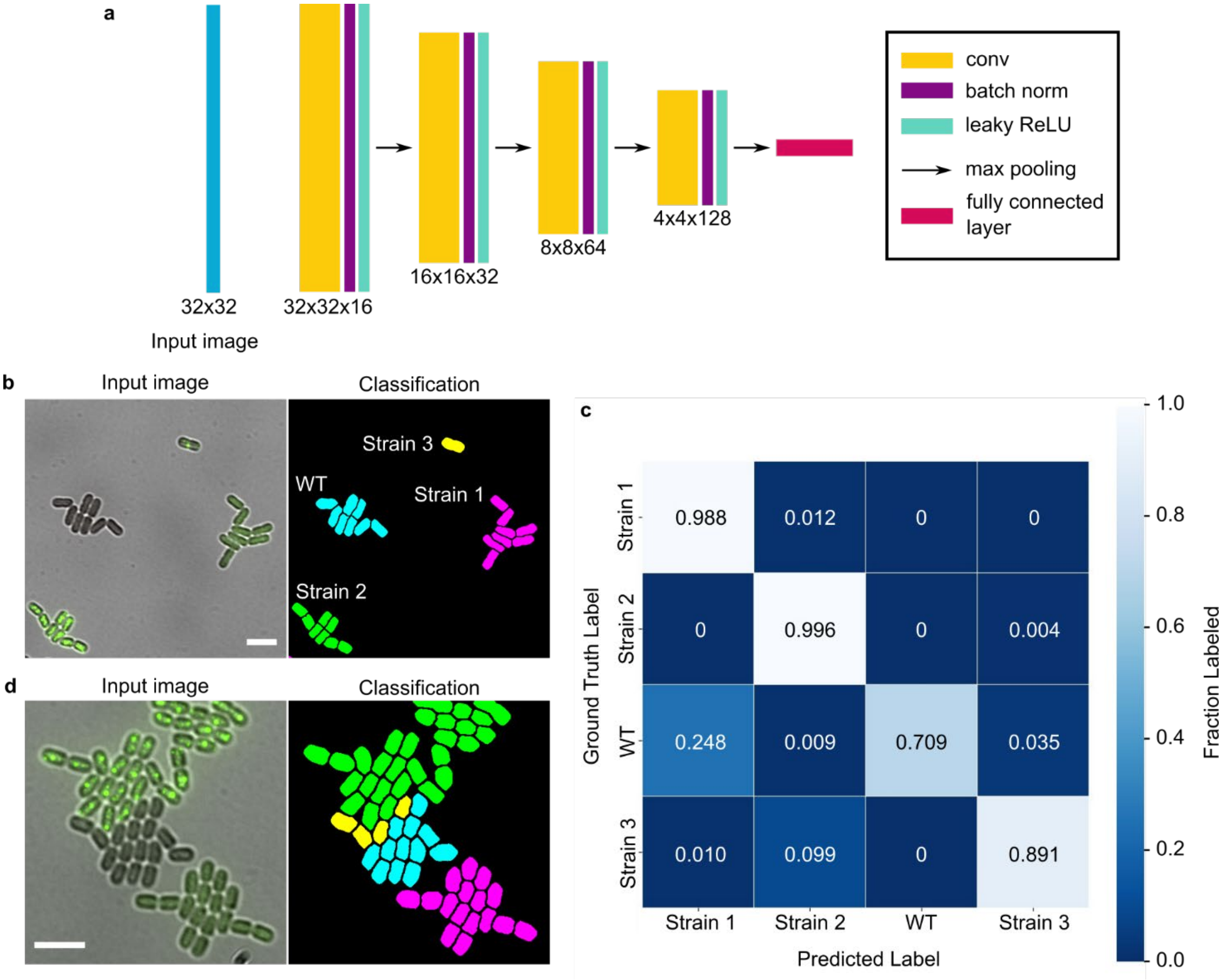

Figure 19. Cyclass-7002 Model

(a) Classification network architecture. The values provided indicate the size of the input image and the sizes of the feature maps in each layer. (b) Representative images showing the input image (only brightfield and one of the GFP channels are shown here for clarity; the full set of channels are shown in S7) and a recolored mask showing the classification of four strains of PCC 7002 cells. The strains have differently localized GFP: WT (no GFP labelling), Strain 1 (diffuse in cytoplasm), Strain 2 (carboxysome), and Strain 3 (procarboxysome). (c) Confusion matrix of the classification model. (d) Image showing the most common classification error, where WT (cyan) is misclassified as Strain 3 (yellow). These errors occur primarily when the colonies grow close together. The scale bars indicate 5 μm.

5.4 Discussion and conclusions

In summary, we have developed machine learning models for segmentation (Cypose) and classification of single cyanobacterial cells (Cyclass) in imaging datasets. These models can be used independently or within a pipeline in our previously developed CyAn software[136] (*Figure 20*). We have shown that the fine-tuned segmentation models generated from the generalist Cellpose models can outperform the originals, even when using images of cells which were highly distinct (i.e., bacteria) compared to those used to train the generalist models (i.e., primarily mammalian cells). Compared to our previous traditional intensity-based thresholding approach, these new models enable segmentation of challenging situations, such as PCC 7002 in dense colonies, and for filamentous bacteria like ATCC 33047.

ML models learn features of the images they are trained on. While the fine-tuned models were able to segment a variety of cell morphologies (particularly the cypose-7002 model which was able to segment the capsule-shaped *Synechococcus elongatus* sp. PCC7942), their ability to segment other species depends on visual similarity to the training images. Running the same validation tests using the "wrong" model for the two species in our study (results shown in *Figure 21* and *Table 6*) shows reduced performance. However, we note that our specialist models still performed better than the cyto2 and cyto3 models, likely because cyanobacteria still share similar characteristics between species. As with any ML model, to apply our models to other cyanobacteria species, it is likely that additional training will be required. However, assuming the cells are similar in shape to those used here, our models can be used as a starting point, thereby reducing the number of images required for training.

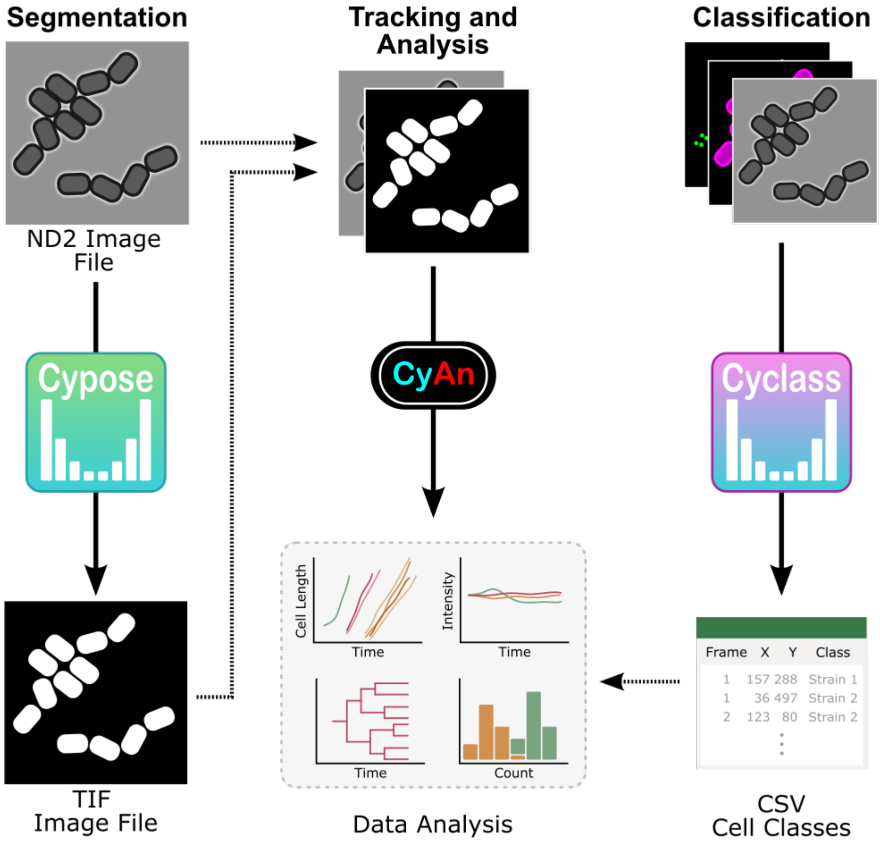

Frame	X	Y	Class
1	157	288	Strain 1
1	36	497	Strain 2
2	123	80	Strain 2
⋮			

Figure 20. Cypose and Cyclass pipeline overview

Overview of developed pipeline. Brightfield images are run through the appropriate Cypose model to generate cell masks, which are then exported as TIFF files. These masks, along with the original images, can then be input into our CyAn software package for tracking and data analysis. For images with different cell types, the images can also be run through a relevant Cyclass model to identify different cell classes. These classifications are saved in a CSV file and subsequently used to inform downstream data analysis.

Additionally, we investigated whether scratch-trained models performed better than fine-tuned models. We found that fine-tuned models trained from existing models provided the best balance between accuracy and resources required. Scratch-trained models offered little or no advantage over transfer learning.

Finally, we demonstrated that a cell classification model can be trained to classify different cellular phenotypes within a single image. Compared to traditional approaches, the cell classification model does not require the user to manually define filters (e.g., cell size or intensity) to identify different cell types, making analysis more robust and less prone to observer bias.

These new models advance the current state of image analysis for cyanobacterial imaging experiments by improving cell segmentation and classification. We believe that these models will enable future microscopy-based assays where different mutants or species are grown in the same conditions and imaged within a single field of view.

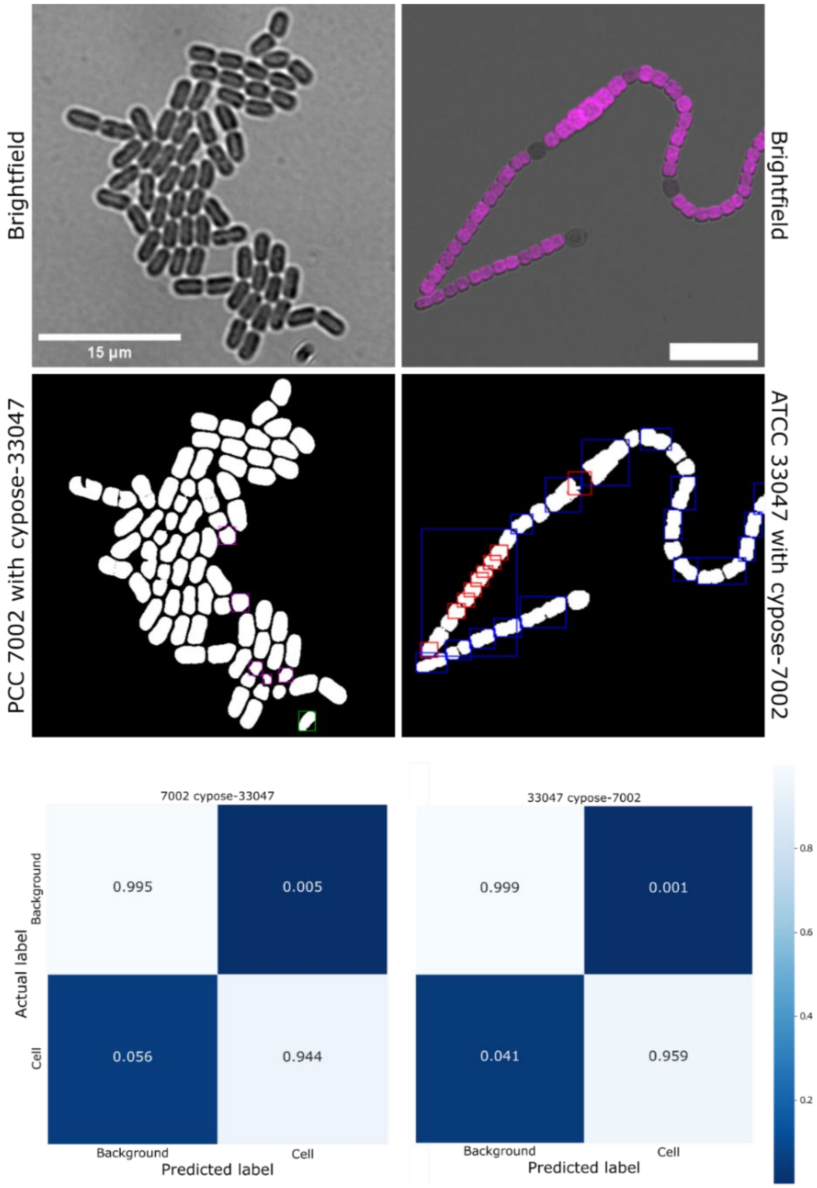

Figure 21. Cross application of segmentation models

Segmentation results and confusion matrices of cross application of the fine-tuned models to the opposite species (cypose-33047 segmenting PCC 7002 and cypose-7002 segmenting ATCC 33047). Errors in each mask are highlighted by a box: undersegmentation in blue, oversegmentation in magenta, false positives (additional objects) in green, and false negatives (missing objects) in red.

5.5 Methods

5.5.1 Dataset generation

5.5.1.1 Strain cultivation

To generate the training datasets, we acquired new images, as well as repurposed datasets from previous experiments, both reported and unreported. Details for all strains are provided in references cited in *Table 7*.

Synechococcus sp. PCC 7002 strains were cultivated in AL-41 L4 Environmental Chambers (Percival Scientific, Perry, IA) at 37°C under constant illumination (~150 µmol photons m^{-2} s^{-1}) by cool white, fluorescent lamps, under either ambient or elevated (3%) CO_2 conditions. Cultures were grown in 25 ml of A+ media in orbital shaking baffled flasks (125 ml) contained with foam stoppers (Jaece Identi-Plug), or on pH 8.2 A+ media solidified with Bacto Agar (1%; w/v). Antibiotics were added for routine growth of strains (kanamycin, 100 µg/ml; gentamycin, 30 µg/ml), depending on the genotype.

Anabaena sp. ATCC 33047 was obtained from the Pakrasi lab and grown at 37°C in BG11 media. All preculturing occurring in 25 mL liquid cultures with 100 rpm orbital shaking in 125 ml baffled flasks with foam stoppers. Liquid and agar cultures were grown in an AL-41 L4 Environmental Chamber (Percival Scientific, Perry, IA) at 37°C under constant illumination at ~150 µmol photons m^{-2} s^{-1} by cool white, fluorescent lamps in ambient air.

5.5.1.2 Microscopy

Images were taken using a Nikon TiE inverted wide-field microscope. Temperature and CO_2 were controlled with an environmental chamber (Okolab) outfitted with a ProCO_2 P120 Carbon Dioxide Single Chamber Controller (BioSpherix). Growth light was provided by a transilluminating red light emitting diode (LED) light source (Lida Light Engine, Lumencor). Fluorescence imaging was carried out using a highspeed light source (Spectra X Light Engine, Lumencor). NIS Elements software (version 5.11.00, 64-bits) with the Jobs acquisition upgrade was used to control the microscope. Image acquisition was performed using an ORCA-Flash4.0 V2+ Digital sCMOS camera (Hamamatsu) with a Nikon CF160 Plan Apochromat Lambda 100× oil immersion objective (1.45 NA) for PCC 7002 or Nikon CFI Plan Apochromat Lambda D 20× air objective (0.80 NA) for ATCC 33047.

To acquire time-lapse datasets, PCC 7002 cells in exponential or early linear phase were diluted to 0.14 OD_{730}. 1 μL was spotted onto a 1% agarose A+ pad and allowed to dry (20 min). The pad was then inverted into an imaging dish, which was then wrapped in parafilm to keep the pad from drying out. The cells were preincubated at 37°C for 1 hour in the dark. Images were taken every 20 minutes. Cells were constantly illuminated with red light except during fluorescent imaging.

ATCC 33047 cells were grown in liquid culture to ~1.00 OD_{730}. 3-5 x 2 μL drops of cells were added to the imaging side of a 1% agarose w/v BG11 (or BG11-N to induce heterocyst differentiation) pad and allowed to dry. The pad was flipped on to an imaging dish (Ibidi μ-dish 35mm glass). The imaging dish was then sealed with parafilm and placed into the microscope. Images were captured every 20 or 30 minutes, depending on the movie.

5.5.1.3 Data preparation

We used existing algorithms to assist with ground truth data generation. Initial cell masks were generated using either the CyAn Toolbox[136] (version 1.3.4) running on MATLAB version R2020b or cyto2 running on Python3. These masks were then manually corrected using ImageJ/Fiji. Dead or overlapping cells were not annotated during this process.

5.5.2 Segmentation model training details

Table 7. Model Descriptions

Description of the models used in this study, along with descriptions of the training datasets.

Model name	Description	Training dataset	Reference
cyto2	Cell cytoplasm segmentation model from Cellpose version 2.0.	Trained in two-channel images, where first channel is channel to segment and second is an optional nuclear channel	167
cyto3	Cell cytoplasm segmentation model from Cellpose version 3.0.	9 datasets; Trained to generate images which segment well from noisy images	169
bact-phase-omni	Bacterial segmentation model from Omnipose	Phase contrast images of assorted bacterial species with diverse morphologies and optical characteristics, 27,500 total cells	170
cypose-7002	Fine-tuned model for segmentation of PCC 7002 cells	6 movies of PCC 7002, 413 frames, 35,000 total cells	This study
cypose-7002-scratch	Scratch-trained model for segmentation of PCC 7002 cells	18 movies of PCC 7002 WT, Δ*murA,* Δ*ftsh1-4,* Δ*pdbH,* Δ*ftsZ,* 2271 frames, 125,040 total cells.	This study
cypose-33047	Fine-tuned model for segmentation of filamentous Anabaena cells	4 movies of ATCC 33047, 233 frames, 68411 total cells	This study
cyclass-7002	Cell classification network	9 movies of PCC 7002, 736 frames, 55,695 total cells	48

5.5.2.1 cypose-7002

The fine-tuned PCC 7002 model was trained using the Cellpose v2 framework[168], starting with the pretrained cyto2 model. A training corpus of 6 movies, consisting of 413 frames with a total of 35,000 cells was used. We note that only the brightfield channel was used for training this model. Training was carried out on a single Nvidia A100 GPU using pytorch (version 2.0.1).[178] The final model was trained for 150 epochs. To benchmark the model, we used a separate movie which was never shown to the model during training. This benchmark movie consisted of 70 frames and 13,214 cells. The evaluation was carried out on an NVIDIA T40 GPU using pytorch version 2.1.2.

5.5.2.2 cypose-33047

As before, this model was trained using the Cellpose v2 framework[168], starting with the pretrained cyto2 model. The training dataset consisted of images of ATCC 33047 containing both brightfield and chlorophyll fluorescence channels. A training corpus of 4 movies, consisting of 233 frames and 68,411 total cells was used. Training was carried out on a NVIDIA T40 GPU using pytorch (version 2.1.2).[178] The final model was trained for 1,250 epochs. To benchmark the model, a separate movie was used. This movie was cropped to a total of 36 representative frames showing different cell densities from the start (20 frames and 1,643 cells), middle (11 frames and 4,986 cells), and end (5 frames and 6,832 cells) of the full-length video for a total of 13,461 cells. The ground-truth data was made using an early version of the cypose-33047 model, then manually corrected.

5.5.2.3 cypose-7002-scratch

This model was trained from scratch using the Cellpose v2[168] framework. Training was carried out on a NVIDIA T40 GPU using pytorch (version 2.1.2).[178] Since a larger dataset is required to train a model from scratch, we used images from an additional 12 time-lapse movies in addition to the 6 movies used to train cypose-7002. The total training set comprised of 18 movies with a total of 2,271 frames and approximately 125,040 cells. To account for the different cell morphologies, the training dataset included images from various PCC 7002 knockdown mutants (e.g., *ΔmurA*, *ΔftsZ*, and *Δftsh1-4*) which show morphological deviations from WT-cells (e.g. cell swelling, cell elongation). The cypose-7002 model was used to generate the initial mask. As before, the masks were then manually corrected to generate the final training dataset.

5.5.3 Segmentation benchmarking

To validate our segmentation models, we calculated the pixel accuracy using the typical precision-recall metrics[167,171] using pytorch (version 2.1.2). However, as discussed above, these metrics provide misleading statistics as errors such as over-segmentation tend to only involve a small number of pixels compared to the size of the cells. As an alternative, we developed an algorithm to identify and count specific segmentation errors. The main segmentation errors that are detected are: over-segmentation (when a predicted object is divided into more pieces than the ground truth), under-segmentation (when multiple objects are grouped together into a single large object), false negative (objects that were found in the ground truth, but are missing in the predicted masks), and false positive (objects which were found in the predicted masks, but are not in the ground truth). To avoid overcounting the number of errors, the algorithm allowed approximately 10% discrepancy between the ground truth and predicted masks.

5.5.4 Training the Cyclass classification model

As shown in Fig. 3a, the Cyclass classification network architecture consists of a series of 4 sets of convolutional layers, with kernel sizes of 3x3. The feature map of each layer was batch normalized, and a leaky ReLU activation function was used. Each layer was followed by a 2x2 max-pooling layer with a stride of 2. A final fully connected layer was used for the classification task.[179] Training was carried out on a NVIDIA T40 GPU using pytorch (version 2.1.2).

To train the model, we used images from a dataset consisting of 4 distinct cell genotypes/phenotypes, as described above. The input images consisted of 5 channels, including brightfield and four fluorescent labels (*Figure 18*). To generate a training set, we manually annotated images as belonging to one of the four cell types. The model was trained with an input image size of 32x32 pixels (about ~1.5x – 2x cell size). It is interesting to note that during testing, smaller images appeared to perform worse suggesting that the network likely requires some information from neighboring cells. Conversely, input images that were larger might confuse the network as it includes too many other cells. The model was trained using the Adam optimizer[180] with learning rate of 1e^{-4}, stopping at 60 epochs. To validate the model, a separate movie consisting of 70 frames and 13,214 cells was used as a benchmark.

The classifier model was integrated into an automated pipeline. To use the classifier, we first generate masks to identify individual cells. The masks are then used to obtain the centroid position of each cell.[181] A region of 32x32 pixels around this location was then cropped from the original image. The cropped image is then fed into the Cyclass network which calculates class probabilities for the cell. The class corresponding to the highest probability is then output to a csv file and used in downstream analysis (*Figure 20*).

Chapter 6 – Cyanobacterial redox dynamics under perturbed redox conditions

6.1 Motivation for study

Unlike the previous two chapters, this chapter consists of entirely unpublished research. So instead of presenting this work as if it was a complete story, which it is most certainly not, I will instead share my results alongside my thoughts on what more is to be done and what could be done better. This is in hopes that this will bring clarity to my own final steps and inspire another to pursue more deeply the questions I will pose. Given the passing of my PI, Jeff Cameron, no one will be following in my footsteps here, so, for whoever might be reading this chapter, if you find this data curious and inspiring, I encourage you to take up the mantle and delve into these mysteries.

Recalling back to one of the first plots I presented, *Figure 9c* and *d*, I showed the responsiveness of the roGFP system to addition of a reducing agent (DTT) and oxidizing agent (H_2O_2) in the carboxysome, cytosol, and procarboxysome. This data was surprising in a couple of ways:

First of all, these bulk culture data were a touch tricky to acquire with consistency. I got the sense that if the time varied between the addition of the redox agent and measurement, the resulting values could vary immensely. What I have reported in *Figure 9c* and *d* was accomplished by being very careful to replicate the timing of ~25s between redox agent addition and measurement. However, this made me interested in what exactly was happening over time to the redox state in these samples.

Secondly, at the time, I was surprised to see DTT reduce the carboxysome. I was not expecting DTT to be able to permeate the carboxysome shell, though in retrospect, I don't see why not. This got me thinking that here was an example of clear permeability of a compound into the carboxysome and that this could be used to further probe carboxysome permeability. With these two thoughts in mind: redox state over time and carboxysome permeability, I began the experimental inquiry of this chapter.

6.2 H_2O_2 Microscopy Timelapse Addition

According to *Figure 9c*, the cytosol became more oxidized when H_2O_2 was added to the cells with no change to the carboxysome redox state. Is this because the carboxysome is already fully oxidized? Or is H_2O_2 not permeating the carboxysome shell? Or something entirely else? All these questions and more I was not able to answer in this section.

To explore more, I turned to our fluorescence microscope given the ease of timelapse measurements on the automated microscope setup as compared to the laborious sample preparation and measurement for bulk cultures on the spectrophotometer. My results were unexpected. Instead of seeing anything becoming more oxidized when exposed to 20 mM H_2O_2, I saw either reduction or no change across the board (*Figure 22*) and, surprisingly, reduction in the carboxysome.

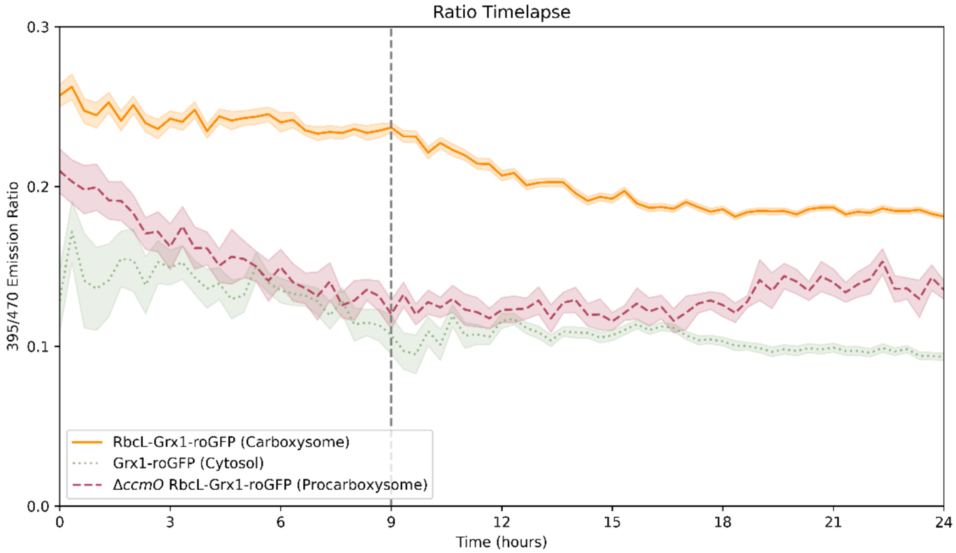

Figure 22. Timelapse microscopy with H_2O_2 addition at hour 9

Aggregated redox state from timelapse fluorescence microscopy of the carboxysome (RbcL-Grx1-roGFP2), procarboxysome (*ΔccmO* RbcL-Grx1-roGFP2), and cytosol (Grx1-roGFP2) over 24 hours of growth in air with 20 mM H_2O_2 added at hour 9 as indicated by the vertical dashed grey line.

Thinking that maybe I missed some smaller dynamic shift happening on a faster timescale than the every-20-minute measurement I typically used on the scope (this helps reduce photodamage to the cells and gives them time to grow with the growth light on), I reran the experiment and took images every 5 minutes post-H_2O_2 addition (*Figure 23*). Pretty much the same result, the carboxysome becomes more reduced with comparably less change in the cytosol. However, with the faster measurement timespan I did capture more definition of cytosolic changes. I also saw that carboxysomes seem to continue a trend towards more reduced, nearly meeting up with the cytosol at the end of the experiment.

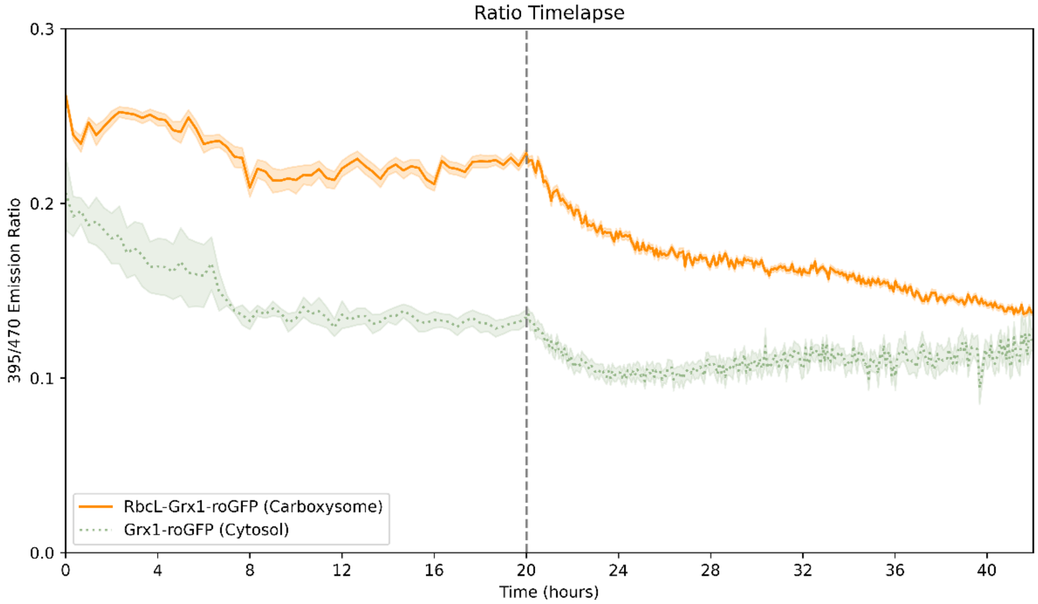

Figure 23. Timelapse microscopy with H_2O_2 addition at hour 20

Aggregated redox state from timelapse fluorescence microscopy of the carboxysome (RbcL-Grx1-roGFP2) and cytosol (Grx1-roGFP2) over 42 hours of growth in air with 20 mM H_2O_2 added at hour 20 as indicated by the vertical dashed grey line. Deviating from typical imaging methods, starting at hour 20 images were taken every 5 minutes instead of the usual 20-minute interval.

I speculate that the cell is accustomed to handling oxidizing agents, photosynthesis is constantly creating them, so perhaps the H_2O_2 is quickly sensed (in less than a 5 min timescale) and mechanisms for maintaining a more reduced environment are upregulated (ie glutathione, which my sensor specifically targets, catalase, and super peroxidase).[21,110,112,113] This upregulation could lead to a bit of an overshoot, hence the small dip in the cytosol to being more reduced, but otherwise the perturbation is swiftly corrected in the dynamic cytosol environment. This hypothesis could be tested by quantifying the glutathione levels over time in response to H_2O_2 addition.

As for the extended trends seen in the carboxysome, I am more inclined to believe the results in *Figure 22* as I suspect the later data in *Figure 23* may be suffering from photobleaching. What we know: carboxysomes are still more oxidized than the cytosol throughout the experiment. New carboxysomes are formed over the 15-hour time period which were not present during the initial H_2O_2 addition. My hypothesis is that if there is more glutathione created in the cytosol in response to the H_2O_2 addition, when new carboxysomes are formed and encapsulated, the carboxysomes will contain a different, more reduced redox pool than the carboxysomes formed prior to the H_2O_2 addition. However, this contradicts my theory proposed in Chapter 4 that the carboxysome is passively oxidized by diffusion of oxygen and H_2O_2 produced by photosynthesis into the carboxysome.

More work needs to be done here. First, fast redox measurements should be taken in the <5min timescale post H_2O_2 addition to track the immediate responses of the cell to this perturbation. In parallel, glutathione levels should be measured over a ~10-hour timescale to see if there are regulatory responses confounding the data (classic *in vivo*). This would address the main hypothesis that I have presented. As for the questions surrounding carboxysome oxidation, I think the experiments in the next section provide a much more direct way to probe this process.

6.3 DTT Timelapse Addition

6.3.1 Traditional timelapse microscopy

Following the same logic as the initial H_2O_2 addition experiments, I added DTT to a timelapse movie on the microscope (*Figure 24*). And WOW! Talk about a response! Even in these later, more jaded stages of my PhD, this data still managed to make me excited and hungry for more. In response to the addition of 100 µM DTT we see everything become more reduced, for a time (~6 hours). Theres a lot going on here, I will break it down into parts.

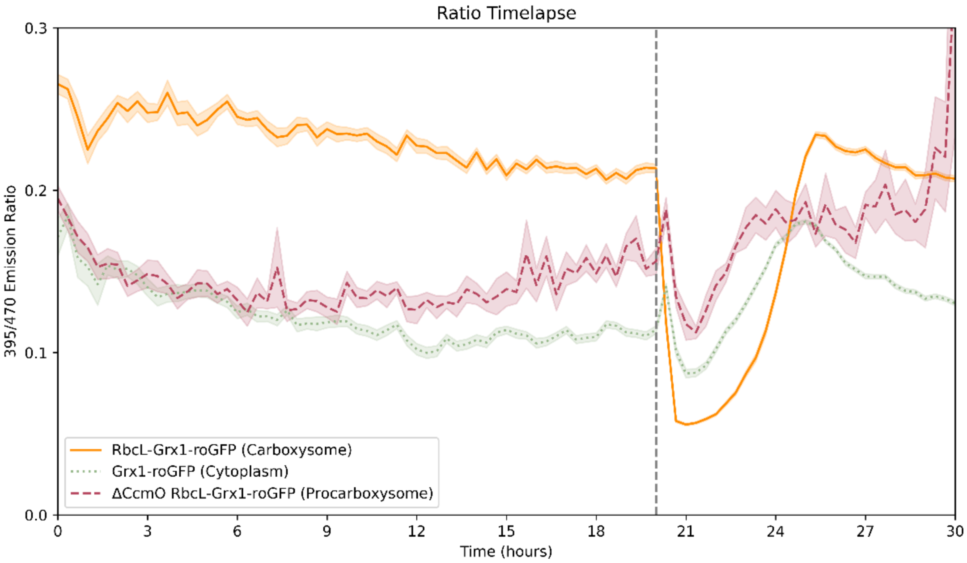

Figure 24. Timelapse microscopy with DTT addition in air

Aggregated redox state from timelapse fluorescence microscopy of the carboxysome (RbcL-Grx1-roGFP2), procarboxysome (*ΔccmO* RbcL-Grx1-roGFP2), and cytosol (Grx1-roGFP2) over 30 hours of growth in air with 100 µM DTT added at hour 20 as indicated by the vertical dashed grey line.

First, let's track the carboxysome redox state. Upon addition of DTT, carboxysomes immediately (<20 min) become dramatically reduced. Then, over the following 6 hours they seem to recover their redox state back to their initial oxidized baseline. If we look at each of the individual carboxysome data points in *Figure 25A*, we also see that we go from a wide range of redox values to a very tight range when they are reduced by DTT then back to a wide range again once returned to baseline.

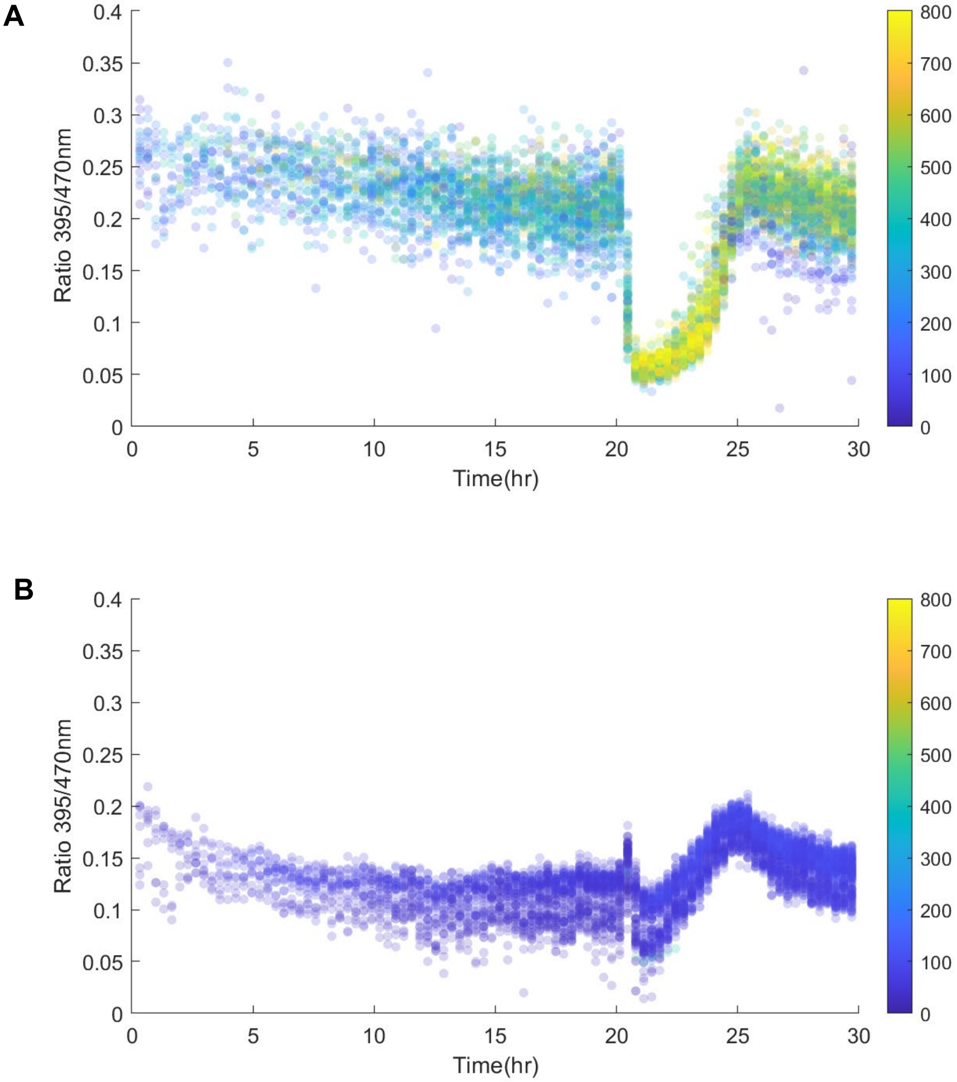

Figure 25. Individual data points from timelapse microscopy with DTT addition in air.

The individual points of (A) carboxysomes and (B) cytosol that comprise the averaged data displayed in Figure 24. The colorbar indicates GFP intensity. 100 µM DTT added at hour 20.

When we consider the cytosol (and procarboxysome, though I decide later to stop probing this compartment as I will explain), things are a touch different (*Figure 24, Figure 25B*). It's subtle and easy to miss in *Figure 24*, but we see more clearly in *Figure 25B* that, upon DTT addition, the cytosol first becomes more oxidized before mirroring the carboxysomes reduction. The recovery appears to massively overshoot the baseline redox state before trending back towards baseline.

This first experiment was all done in air. As I was previously probing changes in redox state when cells were grown in 3% CO_2 (see: all of Chapter 4), I decided to rerun the same experiment in 3% CO_2 and add DTT earlier to capture the 'return to baseline' timeline. And… all the cells died when DTT was added (*Figure 26*). We still capture the immediate reduction in the carboxysome upon DTT addition and a sort of recovery to baseline, but overall, the cells become more oxidized as they perish at different rates.[182] I think this is also quite interesting, it seems the cells are less capable of handling a redox perturbation when in 3% CO_2 which my committee pointed out falls in line with some foundational publications on cellular robustness.[183,184] Essentially, cells may be incredible robust to perturbations when operating under one set of environmental conditions (air in this case), but fragile to perturbations when in a different environmental condition (3% CO_2). This demonstrates that cellular robustness is a function of cellular state. As 3% CO_2 is fatal for cells in these DTT experiments and the procarboxysome strain can only grow in 3% CO_2, I put that strain aside and decided to focus on the carboxysome and cytosol solely.

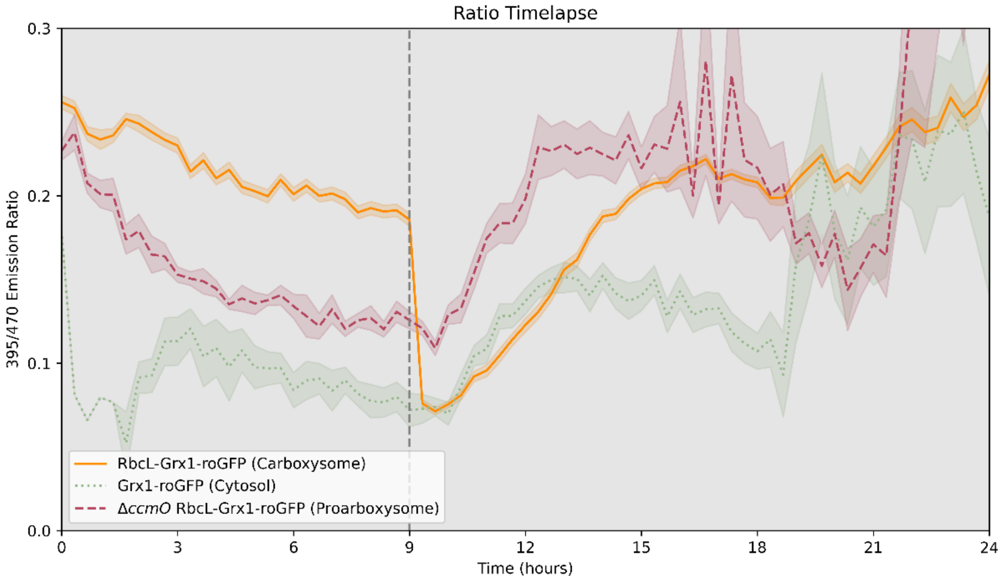

Figure 26. Timelapse microscopy with DTT addition in 3% CO2

Aggregated redox state from timelapse fluorescence microscopy of the carboxysome (RbcL-Grx1-roGFP2), procarboxysome (*ΔccmO* RbcL-Grx1-roGFP2), and cytosol (Grx1-roGFP2) over 24 hours of growth in air with 100 µM DTT added at hour 9 as indicated by the vertical dashed grey line. Cells died, which involves becoming oxidized, at differing time points following DTT addition.

6.3.2 Bulk culture spectrophotometer timelapse

I wanted to check if these fascinating dynamics could be measured not only on the microscope but also in bulk cultures. Using a whole box of cuvettes, half a liter of cultures, and the help of a fellow student to add DTT as close to simultaneously for all samples as was possible, I ran a time trial on the spectrophotometer. To my delight, the data follows much the same trends as we observed on the microscope (*Figure 27*)! We capture the carboxysome becoming reduced over the first 40 min (longer than seen on the microscope) and the cytosol first becoming more oxidized (5 min), then reduced (40 min) before potentially overshooting its baseline to trend back towards baseline over the following 5 hours. This experiment also highlights the need for even more fine time measurements at the <5 min span to track the redox dynamics in the cytosol in response to DTT addition.

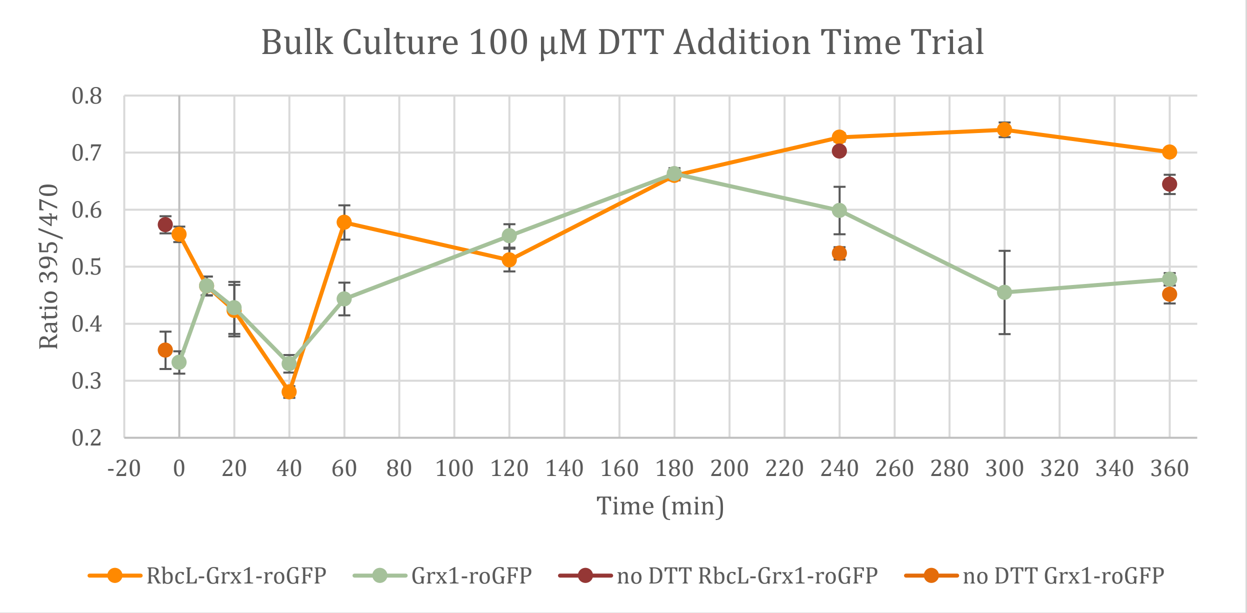

Figure 27. Timelapse bulk spectrofluorometry with DTT addition

Spectrofluorometer measurements of the carboxysome (RbcL-Grx1-roGFP2and cytosol (Grx1-roGFP2) over 6 hours in bulk culture with 100 μM DTT added at time 0. N=3.

I ran only a couple samples without DTT addition at hour 4 and 6 respectively, which are close to their DTT counterparts in redox state. If I were to run this experiment again, I would include more of these controls to better understand how the samples change redox state as they sit in low light on the bench in between measurements. It is very curious to me that we see the carboxysome and cytosol seemingly match in redox state from the ~20-40 min mark then re-oxidize at similar but slightly offset rates. These results prompted my next steps.

6.3.3 Microfluidics timelapse microscopy

I wanted to study these dynamics in more detail. The spectrophotometer method was an excellent proof of the replicability of these trends, but unwieldly to conduct regularly. The method by which I was adding DTT to the microscope with our traditional agar pad was fairly crude (picture: trying to use a syringe to add ~3 μL to an imaging disk set up on a microscope). So, as the section title gives away, I turned to a microfluidics device setup we had utilized in previous experiments in the lab.[62]

Using the CellASIC ONIX2 microfluidics system I could theoretically be much more precise in the concentration of DTT I was exposing the cells to, I could run four experiments simultaneously, and I could either expose the cells to a burst of DTT or prolong the exposure. My goal was to expose the cells to a range of [DTT] and measure the initial change in redox state and time required for recovery to baseline. I figured with this data we could start to ask questions relating to the oxidation rate of the carboxysome and generally how the cells respond to perturbations in redox state.

However, this approach also presented a number of challenges I had to first address:

1. How to minimize DTT degradation prior to addition to the imaging chambers.
2. How to maintain focus on the cells with the wide field of samples in the imaging chambers.
3. How to analyze the imaging data with the microfluidics device posts and a less consistent field of view.

6.3.3.1 DTT Degradation

DTT degrades overtime when exposed to the atmosphere, with faster degradation rates depending on temperature and pH.[185] As the microfluidics device is initially loaded with all the media for the experiment at the beginning of the timelapse and is held at 37°C, I ran a rough test of the activity loss of 20 mM DTT in these conditions (*Figure 28*). At 4°C in the dark I saw a small decline in activity (~20% loss from the initial state) as compared to 37°C in the light (~60-80% loss from the initial state) with the majority of the activity loss after 6 hours of incubation. I ran a second experiment with 100 µM DTT to match my timelapse movie conditions but the activity measurement was at or below baseline, perhaps due to limitations in sensitivity of the Ellman's Assay I was conducting (data not shown). From this work I concluded I needed to carefully (as to not disturb the focus and location of the microscope) add freshly prepared DTT just prior to the switch to DTT exposure on the microfluidics imaging chamber to minimize the impact of DTT degradation.

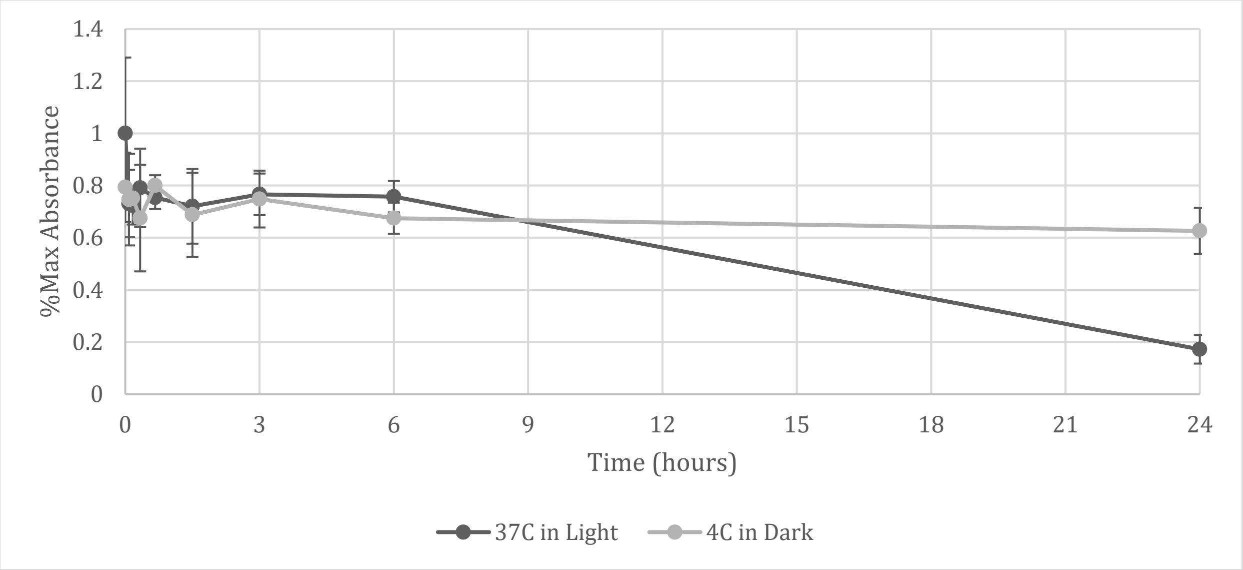

Figure 28. DTT degradation

Time trial with Ellman's Assay of the degradation of 20mM DTT in 37°C under full illumination compared to 4°C in the dark. Axis is scaled to the % max absorbance measured, which may have been an outlier but was maintained for data integrity.

6.3.3.2 Maintaining imaging focus

Many of my initial attempts with the microfluidics device were fraught with issues on maintaining focus and field of view. To cut to the chase on the issue with the focus, this was from user error. Turns out I had not removed some small screws from the microscope plate holder adapter and, with each change in location by the microscope, they would unscrew slightly and raise the adapter by a distance only perceivably by a microscope. Whoops! Fixed.

As for maintaining a field of view, as the microfluidics device imaging chambers are wider spaced than on an agar pad, extra care was needed to stabilize the microfluidics plate with an additional “spring” (i.e. a corkscrew-twisted twist-tie) and parafilm on the outside (but not bottom) of the plate to add friction for the plate holder to grip with. Another issue with the wider space is that the growth light does not equally illuminate all the imaging chambers. Meaning if the growth light was centered between the four imaging chambers, cells in the first and fourth chamber grew slower than those in the second and third. I am still working on further solutions here, but for now I have settled with running all conditions in duplicate, one on an outer chamber and one on an inner chamber to capture both light regimes.

6.3.3.3 Analyzing microfluidics imaging data

It became immediately apparent that analyzing the image data from the microfluidics device via the traditional intensity-based thresholding method I employed for Chapter 4 would be far too laborious a task to be accomplished on a reasonable time scale.[186] Firstly, the plastic posts in the imaging chamber were visible in the brightfield channel and partially identified as cells by our traditional segmentation methods. To hand remove these artifacts from the segmentation would be arduous. Secondly, cells not fully held in place by the imaging chamber system were prone to drifting in or out of the field of view, making it difficult to track my cocultured roGFP strains through their lineage as they grew and divided as I did prior. Again, to hand annotate the strains would be time consuming.

Instead of brute forcing these issues I decided to take a detour and get to the heart of the problem: we needed more robust segmentation methods, and I needed to develop a way to automatically classify my roGFP strains. How did I do this? Well, I used all the data I had already hand-corrected for Chapter 4 and trained segmentation and classification neural networks which, one year later, resulted in the machine learning models Cypose and Cyclass as explained in more detail in Chapter 5.[22] They are not perfect, some hand correction is still required, but this made analyzing microfluidics movies feasible.

6.3.3.4 Next steps

In theory, microfluidics experiments are ready to be executed. At the time of writing this chapter, I have some preliminary microfluidics movies that I have not yet had the time to analyze. I will try to squeeze in some data before this thesis is submitted!

6.4 Discussion and Conclusions

The main observations regarding carboxysomes from these data is that carboxysomes are permeable to DTT and are capable of being re-oxidzed to their original redox state. As this recovery occurs within 6 hours, less than the 16 hour half-life of carboxysomes,[62] I do not think this recovery is driven by production of *de novo* carboxysomes. Therefore, there must be some mechanism, either active or passive, in existing carboxysomes that maintains their oxidized state. I favor that this is a passive mechanism since none of the proteins encapsulated in the carboxysome have any proposed redox modulation capabilities.[18,48] It is unclear if there is a change in carboxysome permeability in response to the DTT addition. A closer look at the growth curves could aid in this distinction, though I did not see a lag in growth in my initial experiments (data not shown). Loss of carboxysome encapsulation should stall carbon fixation and cell growth.

However, if we do see a stall, it will be hard to differentiate the source being changes in carboxysome permeability or some other cellular impact of reduction by DTT, so additional assays would be necessary.

Given DTT seems to be permeable across the carboxysome shell, this could provide a unique platform to study the limitations of shell permeability. DTT could be modified with different chemical groups to probe size and charge property limitations with reduction of the carboxysome at a certain rate acting as the measurement of successful permeation. Reduction of the cytosol (assuming these experiments are performed *in vivo* as I have conducted them) would be a control for cell permeability. As studies of shell permeability have largely been restricted to computational modeling, this set up would provide extremely useful *in vivo* comparisons.

I am not the only person who has documented the ability for the carboxysome to be reduced. Exciting work tracking redox state of carboxysomes *in vitro* found that carboxysomes were reduced within ~15 min by reducing agent Tris(2-Carboxyethyl)Phosphine (TCEP) and that this reduction proceeded faster when the shell was not intact.[17,139] Given the recovery back to an oxidized state in my work, I would be interested to see if there is a similar trend with the *in vitro* system as well, as this would imply the reoxidation is a passive process rather than an adjustment made by the cell. These findings, alongside my results, offer interesting insights into the capabilities of the carboxysome shell as a redox barrier, permeability of small molecules across the shell, and rates of carboxysomal reoxidation.

The main observations regarding the cytosol from these data is the pattern of initial oxidation, then reduction, followed by oxidation before seeming to trend towards recovery. I hypothesize that we are capturing the efforts of internal redox homeostasis mechanisms acting in response to the reduction perturbation. I suspect that, if we increased [DTT], at a certain threshold we would see these mechanisms no longer being capable of recovering homeostasis and subsequently lead to cell death. Finding this reduction resilience threshold could be of use to biotechnological applications of PCC 7002.

I have largely tried to minimize making direct statements comparing the exact redox states of the cytosol and carboxysome, preferring to keep my observations more qualitative (this is less than that, we see a change in x). To make more direct statements (for example: the carboxysome is x-times more oxidized than the cytosol), further normalization of the roGFP readout is required. I believe this would ultimately be necessary for conclusions to be made regarding the work presented in this chapter. These normalizations would involve pushing both the carboxysome and cytosol to be fully oxidized and fully reduced with redox agents to capture the full span of the redox-sensing capabilities of the roGFP localized there. This would allow for any further data to be plotted relative to these min-max ranges and remove dense compartmentalization of roGFP as a potential confounding variable in redox-sensitivity.

Chapter 7 – Conclusions

Here we are. The final chapter of five years of effort diving deep into the world of carbon concentration mechanisms and the cyanobacterial carboxysome. Before I met Jeff, I had never heard of a carboxysome, let alone realized much of anything about the internal complexity of bacteria. I don't think I even comprehended that bacteria could perform photosynthesis. What I did come to the table with was a fascination of the metabolic capabilities of bacteria that allow them to thrive essentially everywhere on Earth and a curiosity about life existing beyond our planet. Those two concepts are interlinked and, to start to probe the possibility of the second (is there extraterrestrial life), we needed first to understand the origins of the first (how life came to conquer our beautiful blue pearl). What better way to approach this study but to work with one of the oldest known organisms.[23] Organisms that harnessed and evolved the fundamental processes by which nearly all life today depends on: oxygenic photosynthesis and carbon fixation.[26]

Not only did Jeff offer to me the study of cyanobacteria as a way to probe these fundamental questions, but he also showed me that this study could be accomplished before one's very own eyes with timelapse fluorescence microscopy. By growing the cyanobacteria directly on the microscope we could analyze phenotypical features as time progressed, know the relationship of every subsequent cell to one another, and control what environment these cells were growing in.[62,134,186] As he often said, seeing is believing. It's hard to argue against what one can see with their own eyes. The data is not wrong, only your interpretations can be. My hope is, with the data and conclusions I have made throughout this dissertation, that my interpretations of what we see are more often right than they are wrong. Only future work by all the other incredible talented scientists in this field will tell.

7.1 Contributions to the field

When I started my research, only one paper had been published, by Chen et al. in the Polka Lab,[16] using fluorescent sensors to probe the carboxysome interior. This article laid the groundwork of my research, and I saw improvements upon their system: Controls in the cytosol, a more specific redox sensor, comparisons of bulk culture and single-cell readouts, and parallel tracking of the shell-less procarboxysome. I also took things further to understand the range of redox states the carboxysome could be pushed to by altering the environment with [CO_2] and redox agents. I want to emphasize when I say redox state, because of the specificity of the roGFP2-Grx1 system, I am specifically referring to the glutathione redox pool.[21]

To summarize my contributions:

1. **The carboxysome is more oxidized than the cytosol in air**, indicating the carboxysome shell maintains a distinct internal redox environment.
2. **The procarboxysome has a similar redox state as the cytosol**, indicating that, without a shell, the procarboxysome aggregation is exposed to the cytosol redox environment.
3. Building from the previous two statements, **in high CO_2 large, reduced, procarboxysome-like structures form**, suggesting potential regulation of carboxysome shell permeability.
4. **The carboxysome is permeable to reducing agent DTT** and capable of being reduced, providing a mechanism by which to study shell permeability in detail.
5. **The carboxysome can recover to its previous oxidized state** after being reduced by DTT, giving a lead into studying mechanisms and rates driving carboxysome oxidation.
6. **I created image analysis tool kits, Cypose and Cyclass**, for the community to expediate data acquisition and interpretation of cyanobacteria microscopy images.

7.2 Future directions

I believe these findings will serve the field in guiding what questions should be asked next. I think most critically to understand their evolutionary origins and to push forward biotechnological applications of the carboxysome, we need to determine the purpose of the carboxysome shell and what is and is not permeable across it. As I have described in more detail where applicable, the work I have shared could be used to serve as a platform by which to dive deeper into the properties of shell permeability and redox regulation. Instead of reiterating myself, I will take this time instead to propose new experiments that may be useful in future explorations.

Building off the incredible system Dr. Nick Hill developed to controllably induce carboxysome formation, a redox sensor could replace the existing GFP and open up new insights on the lifecycle of the carboxysome.[62] The timing, trigger, and mechanisms for carboxysome degradation are still largely a mystery. With roGFP, we could potentially capture when the carboxysome shell breaks open, exposing the originally oxidized carboxysome lumen to the reducing cytosol. We would be able to determine if this shell breakage event occurs prior to or following recruitment to the pole of the cell, followed by degradation.[62] Understanding the processes involved in carboxysome degradation is essential for their robust application in biotechnologies and maintenance in plant systems.

There are multiple redox pools in the cell and throughout this dissertation I have been tracking only one of them, the glutathione pool. [115,149,187,188] When I initially started my work, I was working with not only the Grx1-roGFP2 glutathione sensor, but also a peroxidase-based sensor to track H_2O_2 (roGFP2-Orp1).[189] This H_2O_2 sensor had very low signal, making data analysis unreliable, so I focused instead on the glutathione sensor for the body of my research. However, I think it would be valuable to follow up with the H_2O_2 sensor, adjusting expression levels or reworking the construct to increase fluorescence. Alternative redox pool sensors would help expand the redox dynamics of the carboxysome and could give novel insights on shell permeability and redox-mediated regulatory processes.

I think it would be worthwhile to explore how the redox state of the carboxysome responds to other environmental changes. Very early on in my study I ran experiments with my strains with light/dark cycles to understand how the redox shifted when the photosynthetic machinery was active or inactive. My preliminary results showed an oscillating pattern with more reduction in the dark than in light, though I never followed up on these experiments. Another interesting experiment would be to test the redox state under anoxic conditions. The cells would need to be exposed to oxygen initially to allow for maturation of roGFP.[190] But once in anoxic conditions, if the carboxysomes are reduced (by DTT), do they recover back to an oxidized state? Or is it slowed? If there is slow (and light-dependent) recovery, this suggests that oxygen is responsible for oxidation of the carboxysome but, in anoxic conditions, is limited by oxygen produced by photosynthesis. I can certainly dream up some other very interesting experiments to consider but I will leave those realms of thoughts to future researchers to discover.

There is much more to discover regarding the relationships between redox state and carboxysome maturation, permeability, and maintenance of equilibria. Redox is a fundamental property of life and thermodynamics. I believe many of the mysteries of carboxysomes relate to its redox state. The work I have described in this thesis lays the groundwork and hopefully useful tools for future studies in this realm.

References

(1) Fuchs, G. Alternative Pathways of Carbon Dioxide Fixation: Insights into the Early Evolution of Life? *Annu. Rev. Microbiol.* **2011**, *65*, 631–658. https://doi.org/10.1146/annurev-micro-090110-102801.

(2) Poehlein, A.; Schmidt, S.; Kaster, A.-K.; Goenrich, M.; Vollmers, J.; Thürmer, A.; Bertsch, J.; Schuchmann, K.; Voigt, B.; Hecker, M.; Daniel, R.; Thauer, R. K.; Gottschalk, G.; Müller, V. An Ancient Pathway Combining Carbon Dioxide Fixation with the Generation and Utilization of a Sodium Ion Gradient for ATP Synthesis. *PLoS ONE* **2012**, *7* (3), e33439. https://doi.org/10.1371/journal.pone.0033439.

(3) Takami, H.; Noguchi, H.; Takaki, Y.; Uchiyama, I.; Toyoda, A.; Nishi, S.; Chee, G.-J.; Arai, W.; Nunoura, T.; Itoh, T.; Hattori, M.; Takai, K. A Deeply Branching Thermophilic Bacterium with an Ancient Acetyl-CoA Pathway Dominates a Subsurface Ecosystem. *PLOS ONE* **2012**, *7* (1), e30559. https://doi.org/10.1371/journal.pone.0030559.

(4) Avramov, A. P.; Hwang, H. J.; Burnap, R. L. The Role of Ca2+ and Protein Scaffolding in the Formation of Nature’s Water Oxidizing Complex. *Proc. Natl. Acad. Sci.* **2020**, *117* (45), 28036–28045. https://doi.org/10.1073/pnas.2011315117.

(5) Michaelian, K. Entropy Production and the Origin of Life. *J. Mod. Phys.* **2011**, *02* (06), 595. https://doi.org/10.4236/jmp.2011.226069.

(6) Ulanowicz, R. E.; Hannon, B. M.; May, R. M. Life and the Production of Entropy. *Proc. R. Soc. Lond. B Biol. Sci.* **1997**, *232* (1267), 181–192. https://doi.org/10.1098/rspb.1987.0067.

(7) Morowitz, H.; Smith, E. Energy Flow and the Organization of Life. *Complexity* **2007**, *13* (1), 51–59. https://doi.org/10.1002/cplx.20191.

(8) Benner, S. A.; Bell, E. A.; Biondi, E.; Brasser, R.; Carell, T.; Kim, H.-J.; Mojzsis, S. J.; Omran, A.; Pasek, M. A.; Trail, D. When Did Life Likely Emerge on Earth in an RNA-First Process? *ChemSystemsChem* **2020**, *2* (2), e1900035. https://doi.org/10.1002/syst.201900035.

(9) Itcovitz, J. P.; Rae, A. S. P.; Citron, R. I.; Stewart, S. T.; Sinclair, C. A.; Rimmer, P. B.; Shorttle, O. Reduced Atmospheres of Post-Impact Worlds: The Early Earth. *Planet. Sci. J.* **2022**, *3* (5), 115. https://doi.org/10.3847/PSJ/ac67a9.

(10) Demoulin, C. F.; Lara, Y. J.; Cornet, L.; François, C.; Baurain, D.; Wilmotte, A.; Javaux, E. J. Cyanobacteria Evolution: Insight from the Fossil Record. *Free Radic. Biol. Med.* **2019**, *140*, 206–223. https://doi.org/10.1016/j.freeradbiomed.2019.05.007.

(11) Bar-On, Y. M.; Milo, R. The Global Mass and Average Rate of Rubisco. *Proc. Natl. Acad. Sci.* **2019**, *116* (10), 4738–4743. https://doi.org/10.1073/pnas.1816654116.

(12) Cameron, J. C.; Wilson, S. C.; Bernstein, S. L.; Kerfeld, C. A. Biogenesis of a Bacterial Organelle: The Carboxysome Assembly Pathway. *Cell* **2013**, *155* (5), 1131–1140. https://doi.org/10.1016/j.cell.2013.10.044.

(13) Sarkar, D.; Maffeo, C.; Sutter, M.; Aksimentiev, A.; Kerfeld, C.; Vermaas, J. Atomic View of Photosynthetic Metabolite Permeability Pathways and Confinement in Cyanobacterial Carboxysomes. ChemRxiv February 12, 2024. https://doi.org/10.26434/chemrxiv-2024-kbcdf.

(14) Faulkner, M.; Szabó, I.; Weetman, S. L.; Sicard, F.; Huber, R. G.; Bond, P. J.; Rosta, E.; Liu, L.-N. Molecular Simulations Unravel the Molecular Principles That Mediate Selective Permeability of Carboxysome Shell Protein. *Sci. Rep.* **2020**, *10* (1), 17501. https://doi.org/10.1038/s41598-020-74536-5.

(15) Mangan, N. M.; Flamholz, A.; Hood, R. D.; Milo, R.; Savage, D. F. pH Determines the Energetic Efficiency of the Cyanobacterial CO2 Concentrating Mechanism. *Proc. Natl. Acad. Sci.* **2016**, *113* (36), E5354. https://doi.org/10.1073/pnas.1525145113.

(16) Chen, A. H.; Robinson-Mosher, A.; Savage, D. F.; Silver, P. A.; Polka, J. K. The Bacterial Carbon-Fixing Organelle Is Formed by Shell Envelopment of Preassembled Cargo. *PLOS ONE* **2013**, *8* (9), e76127. https://doi.org/10.1371/journal.pone.0076127.

(17) Carpenter, W. B.; Lavania, A. A.; Borden, J. S.; Oltrogge, L. M.; Perez, D.; Dahlberg, P. D.; Savage, D. F.; Moerner, W. E. Ratiometric Sensing of Redox Environments Inside Individual Carboxysomes Trapped in Solution. *J. Phys. Chem. Lett.* **2022**, *13* (20), 4455–4462. https://doi.org/10.1021/acs.jpclett.2c00782.

(18) Peña, K. L.; Castel, S. E.; de Araujo, C.; Espie, G. S.; Kimber, M. S. Structural Basis of the Oxidative Activation of the Carboxysomal γ-Carbonic Anhydrase, CcmM. *Proc. Natl. Acad. Sci. U. S. A.* **2010**, *107* (6), 2455–2460. https://doi.org/10.1073/pnas.0910866107.

(19) Wang, H.; Yan, X.; Aigner, H.; Bracher, A.; Nguyen, N. D.; Hee, W. Y.; Long, B. M.; Price, G. D.; Hartl, F. U.; Hayer-Hartl, M. Rubisco Condensate Formation by CcmM in β-Carboxysome Biogenesis. *Nature* **2019**, *566* (7742), 131–135. https://doi.org/10.1038/s41586-019-0880-5.

(20) Zang, K.; Wang, H.; Hartl, F. U.; Hayer-Hartl, M. Scaffolding Protein CcmM Directs Multiprotein Phase Separation in β-Carboxysome Biogenesis. *Nat. Struct. Mol. Biol.* **2021**, *28* (11), 909–922. https://doi.org/10.1038/s41594-021-00676-5.

(21) Gutscher, M.; Pauleau, A.-L.; Marty, L.; Brach, T.; Wabnitz, G. H.; Samstag, Y.; Meyer, A. J.; Dick, T. P. Real-Time Imaging of the Intracellular Glutathione Redox Potential. *Nat. Methods* **2008**, *5* (6), 553–559. https://doi.org/10.1038/nmeth.1212.

(22) Huffine, C. A.; Maas, Z. L.; Avramov, A.; Brininger, C. M.; Cameron, J. C.; Tay, J. W. Machine Learning Models for Segmentation and Classification of Cyanobacterial Cells. *Photosynth. Res.* **2025**, *163* (1), 16. https://doi.org/10.1007/s11120-025-01140-x.

(23) Tashiro, T.; Ishida, A.; Hori, M.; Igisu, M.; Koike, M.; Méjean, P.; Takahata, N.; Sano, Y.; Komiya, T. Early Trace of Life from 3.95 Ga Sedimentary Rocks in Labrador, Canada. *Nature* **2017**, *549* (7673), 516–518. https://doi.org/10.1038/nature24019.

(24) Mojzsis, S. J.; Brasser, R.; Kelly, N. M.; Abramov, O.; Werner, S. C. Onset of Giant Planet Migration before 4480 Million Years Ago. *Astrophys. J.* **2019**, *881* (1), 44. https://doi.org/10.3847/1538-4357/ab2c03.

(25) Crockford, P. W.; Bar On, Y. M.; Ward, L. M.; Milo, R.; Halevy, I. The Geologic History of Primary Productivity. *Curr. Biol.* **2023**, S0960982223012861. https://doi.org/10.1016/j.cub.2023.09.040.

(26) Blankenship, R. E. Early Evolution of Photosynthesis1. *Plant Physiol.* **2010**, *154* (2), 434–438. https://doi.org/10.1104/pp.110.161687.

(27) Cardona, T.; Sánchez-Baracaldo, P.; Rutherford, A. W.; Larkum, A. W. Early Archean Origin of Photosystem II. *Geobiology* **2019**, *17* (2), 127–150. https://doi.org/10.1111/gbi.12322.

(28) Soo, R. M.; Hemp, J.; Parks, D. H.; Fischer, W. W.; Hugenholtz, P. On the Origins of Oxygenic Photosynthesis and Aerobic Respiration in Cyanobacteria. *Science* **2017**, *355* (6332), 1436–1440. https://doi.org/10.1126/science.aal3794.

(29) Mehdizadeh Allaf, M.; Peerhossaini, H. Cyanobacteria: Model Microorganisms and Beyond. *Microorganisms* **2022**, *10* (4), 696. https://doi.org/10.3390/microorganisms10040696.

(30) Olejarz, J.; Iwasa, Y.; Knoll, A. H.; Nowak, M. A. The Great Oxygenation Event as a Consequence of Ecological Dynamics Modulated by Planetary Change. *Nat. Commun.* **2021**, *12* (1), 3985. https://doi.org/10.1038/s41467-021-23286-7.

(31) Hurley, S. J.; Wing, B. A.; Jasper, C. E.; Hill, N. C.; Cameron, J. C. Carbon Isotope Evidence for the Global Physiology of Proterozoic Cyanobacteria. *Sci. Adv.* **2021**, *7* (2), eabc8998. https://doi.org/10.1126/sciadv.abc8998.

(32) Boden, J. S.; Konhauser, K. O.; Robbins, L. J.; Sánchez-Baracaldo, P. Timing the Evolution of Antioxidant Enzymes in Cyanobacteria. *Nat. Commun.* **2021**, *12* (1), 4742. https://doi.org/10.1038/s41467-021-24396-y.

(33) Falcón, L. I.; Magallón, S.; Castillo, A. Dating the Cyanobacterial Ancestor of the Chloroplast. *ISME J.* **2010**, *4* (6), 777–783. https://doi.org/10.1038/ismej.2010.2.

(34) Badger, M.; Andrews, T.; Whitney, S.; Ludwig, M.; Yellowlees, D.; Leggat, W.; Price, G. The Diversity and Coevolution of Rubisco, Plastids, Pyrenoids, and Chloroplast-Based CO2-

Concentrating Mechanisms in Algae. *Can. J. Bot.-Rev. Can. Bot. - CAN J BOT* **1998**, *76*, 1052–1071. https://doi.org/10.1139/cjb-76-6-1052.

(35) Michelet, L.; Zaffagnini, M.; Morisse, S.; Sparla, F.; Pérez-Pérez, M. E.; Francia, F.; Danon, A.; Marchand, C. H.; Fermani, S.; Trost, P.; Lemaire, S. D. Redox Regulation of the Calvin–Benson Cycle: Something Old, Something New. *Front. Plant Sci.* **2013**, *4*, 470. https://doi.org/10.3389/fpls.2013.00470.

(36) Huffine, C. A.; Zhao, R.; Tang, Y. J.; Cameron, J. C. Role of Carboxysomes in Cyanobacterial CO2 Assimilation: CO2 Concentrating Mechanisms and Metabolon Implications. *Environ. Microbiol.* **2023**, *25* (2), 219–228. https://doi.org/10.1111/1462-2920.16283.

(37) Shi, X.; Bloom, A. Photorespiration: The Futile Cycle? *Plants* **2021**, *10* (5), 908. https://doi.org/10.3390/plants10050908.

(38) Bauwe, H.; Hagemann, M.; Kern, R.; Timm, S. Photorespiration Has a Dual Origin and Manifold Links to Central Metabolism. *Curr. Opin. Plant Biol.* **2012**, *15* (3), 269–275. https://doi.org/10.1016/j.pbi.2012.01.008.

(39) Broddrick, J. T.; Rubin, B. E.; Welkie, D. G.; Du, N.; Mih, N.; Diamond, S.; Lee, J. J.; Golden, S. S.; Palsson, B. O. Unique Attributes of Cyanobacterial Metabolism Revealed by Improved Genome-Scale Metabolic Modeling and Essential Gene Analysis. *Proc. Natl. Acad. Sci.* **2016**, *113* (51), E8344–E8353. https://doi.org/10.1073/pnas.1613446113.

(40) Timm, S.; Sun, H.; Huang, W. Photorespiration – Emerging Insights into Photoprotection Mechanisms. *Trends Plant Sci.* **2024**, *29* (10), 1052–1055. https://doi.org/10.1016/j.tplants.2024.04.011.

(41) Shih, P. M.; Occhialini, A.; Cameron, J. C.; Andralojc, P. J.; Parry, M. A. J.; Kerfeld, C. A. Biochemical Characterization of Predicted Precambrian RuBisCO. *Nat. Commun.* **2016**, *7* (1), 10382. https://doi.org/10.1038/ncomms10382.

(42) Behrenfeld, M. J.; Randerson, J. T.; McClain, C. R.; Feldman, G. C.; Los, S. O.; Tucker, C. J.; Falkowski, P. G.; Field, C. B.; Frouin, R.; Esaias, W. E.; Kolber, D. D.; Pollack, N. H. Biospheric Primary Production During an ENSO Transition. *Science* **2001**, *291* (5513), 2594–2597. https://doi.org/10.1126/science.1055071.

(43) Huffine, C. A.; Wheeler, L. C.; Wing, B.; Cameron, J. C. Computational Modeling and Evolutionary Implications of Biochemical Reactions in Bacterial Microcompartments. *Curr. Opin. Microbiol.* **2022**, *65*, 15–23. https://doi.org/10.1016/j.mib.2021.10.001.

(44) Dahlgren, K. K.; Gates, C.; Lee, T.; Cameron, J. C. Proximity-Based Proteomics Reveals the Thylakoid Lumen Proteome in the Cyanobacterium Synechococcus Sp. PCC 7002. *Photosynth. Res.* **2021**, *147* (2), 177–195. https://doi.org/10.1007/s11120-020-00806-y.

(45) Ostermeier, M.; Garibay-Hernández, A.; Holzer, V. J. C.; Schroda, M.; Nickelsen, J. Structure, Biogenesis, and Evolution of Thylakoid Membranes. *Plant Cell* **2024**, koae102. https://doi.org/10.1093/plcell/koae102.

(46) Krupovic, M.; Koonin, E. V. Cellular Origin of the Viral Capsid-like Bacterial Microcompartments. *Biol. Direct* **2017**, *12*, 25. https://doi.org/10.1186/s13062-017-0197-y.

(47) Axen, S. D.; Erbilgin, O.; Kerfeld, C. A. A Taxonomy of Bacterial Microcompartment Loci Constructed by a Novel Scoring Method. *PLOS Comput. Biol.* **2014**, *10* (10), e1003898. https://doi.org/10.1371/journal.pcbi.1003898.

(48) Huffine, C. A.; Fontana, C.; Avramov, A.; Sempeck, C.; Cameron, J. C. Cyanobacteria Form a Procarboxysome-like Structure in Response to High CO2. bioRxiv June 28, 2024, p 2024.06.28.601118. https://doi.org/10.1101/2024.06.28.601118.

(49) Ferlez, B.; Sutter, M.; Kerfeld, C. A. Glycyl Radical Enzyme-Associated Microcompartments: Redox-Replete Bacterial Organelles. *mBio* **2019**, *10* (1), e02327-18. https://doi.org/10.1128/mBio.02327-18.

(50) Kennedy, N. W.; Mills, C. E.; Nichols, T. M.; Abrahamson, C. H.; Tullman-Ercek, D. Bacterial Microcompartments: Tiny Organelles with Big Potential. *Curr. Opin. Microbiol.* **2021**, *63*, 36–42. https://doi.org/10.1016/j.mib.2021.05.010.

(51) Zhang, X.; Konarev, P. V.; Petoukhov, M. V.; Svergun, D. I.; Xing, L.; Cheng, R. H.; Haase, I.; Fischer, M.; Bacher, A.; Ladenstein, R.; Meining, W. Multiple Assembly States of Lumazine Synthase: A Model Relating Catalytic Function and Molecular Assembly. *J. Mol. Biol.* **2006**, *362* (4), 753–770. https://doi.org/10.1016/j.jmb.2006.07.037.

(52) Dalmau, M.; Lim, S.; Chen, H. C.; Ruiz, C.; Wang, S.-W. Thermostability and Molecular Encapsulation within an Engineered Caged Protein Scaffold. *Biotechnol. Bioeng.* **2008**, *101* (4), 654–664. https://doi.org/10.1002/bit.21988.

(53) MacCready, J. S.; Vecchiarelli, A. G. Positioning the Model Bacterial Organelle, the Carboxysome | mBio. **2021**.

(54) Melnicki, M. R.; Sutter, M.; Kerfeld, C. A. Evolutionary Relationships among Shell Proteins of Carboxysomes and Metabolosomes. *Curr. Opin. Microbiol.* **2021**, *63*, 1–9. https://doi.org/10.1016/j.mib.2021.05.011.

(55) Liu, L.-N. Bacterial Metabolosomes: New Insights into Their Structure and Bioengineering. *Microb. Biotechnol.* **2021**, *14* (1), 88–93. https://doi.org/10.1111/1751-7915.13740.

(56) Liu, L.-N.; Yang, M.; Sun, Y.; Yang, J. Protein Stoichiometry, Structural Plasticity and Regulation of Bacterial Microcompartments. *Curr. Opin. Microbiol.* **2021**, *63*, 133–141. https://doi.org/10.1016/j.mib.2021.07.006.

(57) Stewart, K. L.; Stewart, A. M.; Bobik, T. A. Prokaryotic Organelles: Bacterial Microcompartments in E. Coli and Salmonella. *EcoSal Plus* **2020**, *9* (1). https://doi.org/10.1128/ecosalplus.ESP-0025-2019.

(58) Mallette, E.; Kimber, M. S. Structural and Kinetic Characterization of (S)-1-Amino-2-Propanol Kinase from the Aminoacetone Utilization Microcompartment of Mycobacterium Smegmatis. *J. Biol. Chem.* **2018**, *293* (51), 19909–19918. https://doi.org/10.1074/jbc.RA118.005485.

(59) Zarzycki, J.; Erbilgin, O.; Kerfeld, C. A. Bioinformatic Characterization of Glycyl Radical Enzyme-Associated Bacterial Microcompartments. *Appl. Environ. Microbiol.* **2015**, *81* (24), 8315–8329. https://doi.org/10.1128/AEM.02587-15.

(60) Kennedy, N. W.; Hershewe, J. M.; Nichols, T. M.; Roth, E. W.; Wilke, C. D.; Mills, C. E.; Jewett, M. C.; Tullman-Ercek, D. Apparent Size and Morphology of Bacterial Microcompartments Varies with Technique. *PLOS ONE* **2020**, *15* (3), e0226395. https://doi.org/10.1371/journal.pone.0226395.

(61) Liberton, M.; Austin, J. R., II; Berg, R. H.; Pakrasi, H. B. Unique Thylakoid Membrane Architecture of a Unicellular N2-Fixing Cyanobacterium Revealed by Electron Tomography. *Plant Physiol.* **2011**, *155* (4), 1656–1666. https://doi.org/10.1104/pp.110.165332.

(62) Hill, N. C.; Tay, J. W.; Altus, S.; Bortz, D. M.; Cameron, J. C. Life Cycle of a Cyanobacterial Carboxysome. *Sci. Adv.* **2020**, *6* (19), eaba1269. https://doi.org/10.1126/sciadv.aba1269.

(63) Kimber, M. S. Carboxysomal Carbonic Anhydrases. In *Carbonic Anhydrase: Mechanism, Regulation, Links to Disease, and Industrial Applications*; Frost, S. C., McKenna, R., Eds.; Subcellular Biochemistry; Springer Netherlands: Dordrecht, 2014; pp 89–103. https://doi.org/10.1007/978-94-007-7359-2_6.

(64) McGurn, L. D.; Moazami-Goudarzi, M.; White, S. A.; Suwal, T.; Brar, B.; Tang, J. Q.; Espie, G. S.; Kimber, M. S. The Structure, Kinetics and Interactions of the β-Carboxysomal β-Carbonic Anhydrase, CcaA. *Biochem. J.* **2016**, *473* (24), 4559–4572. https://doi.org/10.1042/BCJ20160773.

(65) Price, G. D.; Coleman, J. R.; Badger, M. R. Association of Carbonic Anhydrase Activity with Carboxysomes Isolated from the Cyanobacterium *Synechococcus* PCC7942. *Plant Physiol.* **1992**, *100* (2), 784–793. https://doi.org/10.1104/pp.100.2.784.

(66) Selim, K. A.; Haffner, M.; Mantovani, O.; Albrecht, R.; Zhu, H.; Hagemann, M.; Forchhammer, K.; Hartmann, M. D. Carbon Signaling Protein SbtB Possesses Atypical Redox-Regulated Apyrase Activity to Facilitate Regulation of Bicarbonate Transporter SbtA. *Proc. Natl. Acad. Sci.* **2023**, *120* (8), e2205882120. https://doi.org/10.1073/pnas.2205882120.

(67) Sültemeyer, D.; Price, G. D.; Yu, J.-W.; Badger, M. R. Characterisation of Carbon Dioxide and Bicarbonate Transport during Steady-State Photosynthesis in the Marine Cyanobacterium

Synechococcus Strain PCC7002. *Planta* **1995**, *197* (4), 597–607. https://doi.org/10.1007/BF00191566.

(68) Badger, M. R.; Price, G. D. CO2 Concentrating Mechanisms in Cyanobacteria: Molecular Components, Their Diversity and Evolution. *J. Exp. Bot.* **2003**, *54* (383), 609–622. https://doi.org/10.1093/jxb/erg076.

(69) Kinney, J. N.; Salmeen, A.; Cai, F.; Kerfeld, C. A. Elucidating Essential Role of Conserved Carboxysomal Protein CcmN Reveals Common Feature of Bacterial Microcompartment Assembly. *J. Biol. Chem.* **2012**, *287* (21), 17729–17736. https://doi.org/10.1074/jbc.M112.355305.

(70) Kerfeld, C. A.; Melnicki, M. R. Assembly, Function and Evolution of Cyanobacterial Carboxysomes. *Curr. Opin. Plant Biol.* **2016**, *31*, 66–75. https://doi.org/10.1016/j.pbi.2016.03.009.

(71) Turmo, A.; Gonzalez-Esquer, C. R.; Kerfeld, C. A. Carboxysomes: Metabolic Modules for CO2 Fixation. *FEMS Microbiol. Lett.* **2017**, *364* (18). https://doi.org/10.1093/femsle/fnx176.

(72) Chen, X.; Zheng, F.; Wang, P.; Mi, H. Novel Protein CcmS Is Required for Stabilization of the Assembly of β-Carboxysome in Synechocystis Sp. Strain PCC 6803. *New Phytol.* **2023**, *n/a* (n/a). https://doi.org/10.1111/nph.19016.

(73) Cheng, J.; Li, C.-Y.; Meng, M.; Li, J.-X.; Liu, S.-J.; Cao, H.-Y.; Wang, N.; Zhang, Y.-Z.; Liu, L.-N. Molecular Interactions of the Chaperone CcmS and Carboxysome Shell Protein CcmK1 That Mediate β-Carboxysome Assembly. *Plant Physiol.* **2024**, kiae438. https://doi.org/10.1093/plphys/kiae438.

(74) Liu, L.-N. Advances in the Bacterial Organelles for CO2 Fixation. *Trends Microbiol.* **2022**, *30* (6), 567–580. https://doi.org/10.1016/j.tim.2021.10.004.

(75) Rae, B. D.; Long, B. M.; Badger, M. R.; Price, G. D. Structural Determinants of the Outer Shell of β-Carboxysomes in Synechococcus Elongatus PCC 7942: Roles for CcmK2, K3-K4, CcmO, and CcmL. *PLOS ONE* **2012**, *7* (8), e43871. https://doi.org/10.1371/journal.pone.0043871.

(76) Cai, F.; Menon, B. B.; Cannon, G. C.; Curry, K. J.; Shively, J. M.; Heinhorst, S. The Pentameric Vertex Proteins Are Necessary for the Icosahedral Carboxysome Shell to Function as a CO2 Leakage Barrier. *PLOS ONE* **2009**, *4* (10), e7521. https://doi.org/10.1371/journal.pone.0007521.

(77) Ochoa, J. M.; Yeates, T. O. Recent Structural Insights into Bacterial Microcompartment Shells. *Curr. Opin. Microbiol.* **2021**, *62*, 51–60. https://doi.org/10.1016/j.mib.2021.04.007.

(78) Sommer, M.; Sutter, M.; Gupta, S.; Kirst, H.; Turmo, A.; Lechno-Yossef, S.; Burton, R. L.; Saechao, C.; Sloan, N. B.; Cheng, X.; Chan, L.-J. G.; Petzold, C. J.; Fuentes-Cabrera, M.; Ralston, C. Y.; Kerfeld, C. A. Heterohexamers Formed by CcmK3 and CcmK4 Increase the Complexity of Beta Carboxysome Shells1[OPEN]. *Plant Physiol.* **2019**, *179* (1), 156–167. https://doi.org/10.1104/pp.18.01190.

(79) Cai, F.; Sutter, M.; Cameron, J. C.; Stanley, D. N.; Kinney, J. N.; Kerfeld, C. A. The Structure of CcmP, a Tandem Bacterial Microcompartment Domain Protein from the β-Carboxysome, Forms a Subcompartment Within a Microcompartment. *J. Biol. Chem.* **2013**, *288* (22), 16055–16063. https://doi.org/10.1074/jbc.M113.456897.

(80) Larsson, A. M.; Hasse, D.; Valegård, K.; Andersson, I. Crystal Structures of β-Carboxysome Shell Protein CcmP: Ligand Binding Correlates with the Closed or Open Central Pore. *J. Exp. Bot.* **2017**, *68* (14), 3857–3867. https://doi.org/10.1093/jxb/erx070.

(81) Wang, J.; Zhang, Y.; Su, Y.; Liu, X.; Zhang, P.; Lin, R.-B.; Chen, S.; Deng, Q.; Zeng, Z.; Deng, S.; Chen, B. Fine Pore Engineering in a Series of Isoreticular Metal-Organic Frameworks for Efficient C2H2/CO2 Separation. *Nat. Commun.* **2022**, *13* (1), 200. https://doi.org/10.1038/s41467-021-27929-7.

(82) Liu, S.; Xiang, X.; Liu, H. NEPRE: A Scoring Function for Protein Structures Based on Neighbourhood Preference. bioRxiv November 6, 2018, p 463554. https://doi.org/10.1101/463554.

(83) Dou, Z.; Heinhorst, S.; Williams, E. B.; Murin, C. D.; Shively, J. M.; Cannon, G. C. CO2 Fixation Kinetics of Halothiobacillus Neapolitanus Mutant Carboxysomes Lacking Carbonic Anhydrase

Suggest the Shell Acts as a Diffusional Barrier for CO2. *J. Biol. Chem.* **2008**, *283* (16), 10377–10384. https://doi.org/10.1074/jbc.M709285200.

(84) Sarkar, D.; Maffeo, C.; Sutter, M.; Aksimentiev, A.; Kerfeld, C. A.; Vermaas, J. V. Atomic View of Photosynthetic Metabolite Permeability Pathways and Confinement in Synthetic Carboxysome Shells. *Proc. Natl. Acad. Sci.* **2024**, *121* (45), e2402277121. https://doi.org/10.1073/pnas.2402277121.

(85) Mangan, N. M.; Brenner, M. P. Systems Analysis of the CO2 Concentrating Mechanism in Cyanobacteria. *eLife* **2014**, *3*, e02043. https://doi.org/10.7554/eLife.02043.

(86) Dai, W.; Chen, M.; Myers, C.; Ludtke, S. J.; Pettitt, B. M.; King, J. A.; Schmid, M. F.; Chiu, W. Visualizing Individual RuBisCO and Its Assembly into Carboxysomes in Marine Cyanobacteria by Cryo-Electron Tomography. *J. Mol. Biol.* **2018**, *430* (21), 4156–4167. https://doi.org/10.1016/j.jmb.2018.08.013.

(87) Ni, T.; Sun, Y.; Seaton-Burn, W.; Al-Hazeem, M. M. J.; Zhu, Y.; Yu, X.; Liu, L.-N.; Zhang, P. Tales of Two α-Carboxysomes: The Structure and Assembly of Cargo Rubisco. bioRxiv March 16, 2022, p 2022.03.15.484529. https://doi.org/10.1101/2022.03.15.484529.

(88) Huang, F.; Vasieva, O.; Sun, Y.; Faulkner, M.; Dykes, G. F.; Zhao, Z.; Liu, L.-N. Roles of RbcX in Carboxysome Biosynthesis in the Cyanobacterium Synechococcus Elongatus PCC79421. *Plant Physiol.* **2019**, *179* (1), 184–194. https://doi.org/10.1104/pp.18.01217.

(89) Stec, B. Structural Mechanism of RuBisCO Activation by Carbamylation of the Active Site Lysine. *Proc. Natl. Acad. Sci.* **2012**, *109* (46), 18785–18790. https://doi.org/10.1073/pnas.1210754109.

(90) Flamholz, A. I.; Prywes, N.; Moran, U.; Davidi, D.; Bar-On, Y. M.; Oltrogge, L. M.; Alves, R.; Savage, D.; Milo, R. Revisiting Trade-Offs between Rubisco Kinetic Parameters. *Biochemistry* **2019**, *58* (31), 3365–3376. https://doi.org/10.1021/acs.biochem.9b00237.

(91) Amritkar, K.; Cuevas-Zuviría, B.; Kaçar, B. Evolutionary Dynamics of RuBisCO: Emergence of the Small Subunit and Its Impact Through Time. *Mol. Biol. Evol.* **2025**, *42* (1), msae268. https://doi.org/10.1093/molbev/msae268.

(92) de Araujo, C.; Arefeen, D.; Tadesse, Y.; Long, B. M.; Price, G. D.; Rowlett, R. S.; Kimber, M. S.; Espie, G. S. Identification and Characterization of a Carboxysomal γ-Carbonic Anhydrase from the Cyanobacterium Nostoc Sp. PCC 7120. *Photosynth. Res.* **2014**, *121* (2), 135–150. https://doi.org/10.1007/s11120-014-0018-4.

(93) Price, G. D.; Badger, M. R. Expression of Human Carbonic Anhydrase in the Cyanobacterium Synechococcus PCC7942 Creates a High CO2-Requiring Phenotype. *Plant Physiol.* **1989**, *91* (2), 505–513.

(94) Cai, F.; Bernstein, S. L.; Wilson, S. C.; Kerfeld, C. A. Production and Characterization of Synthetic Carboxysome Shells with Incorporated Luminal Proteins. *Plant Physiol.* **2016**, *170* (3), 1868–1877. https://doi.org/10.1104/pp.15.01822.

(95) Long, B. M.; Tucker, L.; Badger, M. R.; Price, G. D. Functional Cyanobacterial β-Carboxysomes Have an Absolute Requirement for Both Long and Short Forms of the CcmM Protein. *Plant Physiol.* **2010**, *153* (1), 285–293. https://doi.org/10.1104/pp.110.154948.

(96) Sun, H.; Cui, N.; Han, S.-J.; Chen, Z.-P.; Xia, L.-Y.; Chen, Y.; Jiang, Y.-L.; Zhou, C.-Z. Complex Structure Reveals CcmM and CcmN Form a Heterotrimeric Adaptor in β-Carboxysome. *Protein Sci.* **2021**, *30* (8), 1566–1576. https://doi.org/10.1002/pro.4090.

(97) Rillema, R.; Hoang, Y.; MacCready, J. S.; Vecchiarelli, A. G. Carboxysome Mispositioning Alters Growth, Morphology, and Rubisco Level of the Cyanobacterium Synechococcus Elongatus PCC 7942. *mBio* **2021**, *12* (4), 10.1128/mbio.02696-20. https://doi.org/10.1128/mbio.02696-20.

(98) Savage, D. F.; Afonso, B.; Chen, A. H.; Silver, P. A. Spatially Ordered Dynamics of the Bacterial Carbon Fixation Machinery. *Science* **2010**, *327* (5970), 1258–1261. https://doi.org/10.1126/science.1186090.

(99) MacCready, J. S.; Basalla, J. L.; Vecchiarelli, A. G. Origin and Evolution of Carboxysome Positioning Systems in Cyanobacteria. *Mol. Biol. Evol.* **2020**, *37* (5), 1434–1451. https://doi.org/10.1093/molbev/msz308.

(100) Vecchiarelli, A.; Hoang, Y.; Azaldegui, C.; Ghalmi, M.; Biteen, J. *An Experimental Framework to Assess Biomolecular Condensates in Bacteria*; preprint; In Review, 2023. https://doi.org/10.21203/rs.3.rs-2725220/v1.

(101) Sun, Y.; Casella, S.; Fang, Y.; Huang, F.; Faulkner, M.; Barrett, S.; Liu, L.-N. Light Modulates the Biosynthesis and Organization of Cyanobacterial Carbon Fixation Machinery through Photosynthetic Electron Flow1[OPEN]. *Plant Physiol.* **2016**, *171* (1), 530–541. https://doi.org/10.1104/pp.16.00107.

(102) Oren, N.; Timm, S.; Frank, M.; Mantovani, O.; Murik, O.; Hagemann, M. Red/Far-Red Light Signals Regulate the Activity of the Carbon-Concentrating Mechanism in Cyanobacteria. *Sci. Adv.* **2021**, *7* (34), eabg0435. https://doi.org/10.1126/sciadv.abg0435.

(103) Rillema, R.; Hoang, Y.; MacCready, J. S.; Vecchiarelli, A. G. Carboxysome Mispositioning Alters Growth, Morphology, and Rubisco Level of the Cyanobacterium Synechococcus Elongatus PCC 7942. *mBio* **2021**, *12* (4), e02696-20. https://doi.org/10.1128/mBio.02696-20.

(104) Singh, A. K.; Santos-Merino, M.; Sakkos, J. K.; Walker, B. J.; Ducat, D. C. Rubisco Regulation in Response to Altered Carbon Status in the Cyanobacterium Synechococcus Elongatus PCC 7942. *Plant Physiol.* **2022**, kiac065. https://doi.org/10.1093/plphys/kiac065.

(105) Santos-Merino, M.; Nikkanen, L.; Kokarakis, E. J.; Allahverdiyeva, Y.; Ducat, D. C. Plastoquinone Redox Status Influences Carboxysome Integrity via a RpaA- and ROS-Dependent Regulatory Network. bioRxiv January 24, 2025, p 2025.01.24.634715. https://doi.org/10.1101/2025.01.24.634715.

(106) Ansong, C.; Sadler, N. C.; Hill, E. A.; Lewis, M. P.; Zink, E. M.; Smith, R. D.; Beliaev, A. S.; Konopka, A. E.; Wright, A. T. Characterization of Protein Redox Dynamics Induced during Light-to-Dark Transitions and Nutrient Limitation in Cyanobacteria. *Front. Microbiol.* **2014**, *5*.

(107) Sadler, N. C.; Melnicki, M. R.; Serres, M. H.; Merkley, E. D.; Chrisler, W. B.; Hill, E. A.; Romine, M. F.; Kim, S.; Zink, E. M.; Datta, S.; Smith, R. D.; Beliaev, A. S.; Konopka, A.; Wright, A. T. Live Cell Chemical Profiling of Temporal Redox Dynamics in a Photoautotrophic Cyanobacterium. *ACS Chem. Biol.* **2014**, *9* (1), 291–300. https://doi.org/10.1021/cb400769v.

(108) Dietz, K.-J.; Pfannschmidt, T. Novel Regulators in Photosynthetic Redox Control of Plant Metabolism and Gene Expression. *Plant Physiol.* **2011**, *155* (4), 1477–1485. https://doi.org/10.1104/pp.110.170043.

(109) Hackenberg, C.; Huege, J.; Engelhardt, A.; Wittink, F.; Laue, M.; Matthijs, H. C. P.; Kopka, J.; Bauwe, H.; Hagemann, M. Low-Carbon Acclimation in Carboxysome-Less and Photorespiratory Mutants of the Cyanobacterium Synechocystis Sp. Strain PCC 6803. *Microbiology* **2012**, *158* (2), 398–413. https://doi.org/10.1099/mic.0.054544-0.

(110) Cameron, J. C.; Pakrasi, H. B. Essential Role of Glutathione in Acclimation to Environmental and Redox Perturbations in the Cyanobacterium Synechocystis Sp. PCC 6803. *Plant Physiol.* **2010**, *154* (4), 1672–1685. https://doi.org/10.1104/pp.110.162990.

(111) Nomura, C. T.; Sakamoto, T.; Bryant, D. A. Roles for Heme–Copper Oxidases in Extreme High-Light and Oxidative Stress Response in the Cyanobacterium Synechococcus Sp. PCC 7002. *Arch. Microbiol.* **2006**, *185* (6), 471–479. https://doi.org/10.1007/s00203-006-0107-7.

(112) Hudek, L.; Enez, A.; Bräu, L. Cyanobacterial Catalase Activity Prevents Oxidative Stress Induced by Pseudomonas Fluorescens DUS1-27 from Inhibiting Brassica Napus L. (Canola) Growth. *Microbes Environ.* **2018**, *33* (4), 407–416. https://doi.org/10.1264/jsme2.ME18061.

(113) Samanta, L.; Stensjö, K.; Lindblad, P.; Bhattacharya, J. Differential Catalase Activity and Tolerance to Hydrogen Peroxide in the Filamentous Cyanobacteria Nostoc Punctiforme ATCC 29133 and Anabaena Sp. PCC 7120. *Arch. Microbiol.* **2022**, *204* (2), 121. https://doi.org/10.1007/s00203-021-02643-6.

(114) Mantovani, O.; Haffner, M.; Walke, P.; Elshereef, A. A.; Wagner, B.; Petras, D.; Forchhammer, K.; Selim, K. A.; Hagemann, M. The Redox-Sensitive R-Loop of the Carbon Control Protein SbtB Contributes to the Regulation of the Cyanobacterial CCM. *Sci. Rep.* **2024**, *14* (1), 7885. https://doi.org/10.1038/s41598-024-58354-7.

(115) Reuter, W. H.; Masuch, T.; Ke, N.; Lenon, M.; Radzinski, M.; Van Loi, V.; Ren, G.; Riggs, P.; Antelmann, H.; Reichmann, D.; Leichert, L. I.; Berkmen, M. Utilizing Redox-Sensitive GFP Fusions to Detect in Vivo Redox Changes in a Genetically Engineered Prokaryote. *Redox Biol.* **2019**, *26*, 101280. https://doi.org/10.1016/j.redox.2019.101280.

(116) van der Heijden, J.; Vogt, S. L.; Reynolds, L. A.; Peña-Díaz, J.; Tupin, A.; Aussel, L.; Finlay, B. B. Exploring the Redox Balance inside Gram-Negative Bacteria with Redox-Sensitive GFP. *Free Radic. Biol. Med.* **2016**, *91*, 34–44. https://doi.org/10.1016/j.freeradbiomed.2015.11.029.

(117) Menon, B. B.; Dou, Z.; Heinhorst, S.; Shively, J. M.; Cannon, G. C. Halothiobacillus Neapolitanus Carboxysomes Sequester Heterologous and Chimeric RubisCO Species. *PLoS ONE* **2008**, *3* (10), e3570. https://doi.org/10.1371/journal.pone.0003570.

(118) Davidi, D.; Shamshoum, M.; Guo, Z.; Bar-On, Y. M.; Prywes, N.; Oz, A.; Jablonska, J.; Flamholz, A.; Wernick, D. G.; Antonovsky, N.; de Pins, B.; Shachar, L.; Hochhauser, D.; Peleg, Y.; Albeck, S.; Sharon, I.; Mueller-Cajar, O.; Milo, R. Highly Active Rubiscos Discovered by Systematic Interrogation of Natural Sequence Diversity. *EMBO J.* **2020**, *39* (18), e104081. https://doi.org/10.15252/embj.2019104081.

(119) Flamholz, A. I.; Dugan, E.; Blikstad, C.; Gleizer, S.; Ben-Nissan, R.; Amram, S.; Antonovsky, N.; Ravishankar, S.; Noor, E.; Bar-Even, A.; Milo, R.; Savage, D. F. Functional Reconstitution of a Bacterial CO2 Concentrating Mechanism in Escherichia Coli. *eLife* **2020**, *9*, e59882. https://doi.org/10.7554/eLife.59882.

(120) Zhang, Y.; Zhou, J.; Zhang, Y.; Liu, T.; Lu, X.; Men, D.; Zhang, X.-E. Auxiliary Module Promotes the Synthesis of Carboxysomes in E. Coli to Achieve High-Efficiency CO2 Assimilation. *ACS Synth. Biol.* **2021**, *10* (4), 707–715. https://doi.org/10.1021/acssynbio.0c00436.

(121) Sidhu, G. K.; Pandey, R.; Kaur, G.; Singh, A.; Lenka, S. K.; Reddy, P. M. Towards Assembling Functional Cyanobacterial β-Carboxysomes in Oryza Sativa Chloroplasts. *Funct. Integr. Genomics* **2025**, *25* (1), 5. https://doi.org/10.1007/s10142-024-01518-5.

(122) McGrath, J. M.; Long, S. P. Can the Cyanobacterial Carbon-Concentrating Mechanism Increase Photosynthesis in Crop Species? A Theoretical Analysis. *Plant Physiol.* **2014**, *164* (4), 2247–2261. https://doi.org/10.1104/pp.113.232611.

(123) Yin, X.; Struik, P. C. Can Increased Leaf Photosynthesis Be Converted into Higher Crop Mass Production? A Simulation Study for Rice Using the Crop Model GECROS. *J. Exp. Bot.* **2017**, *68* (9), 2345–2360. https://doi.org/10.1093/jxb/erx085.

(124) Lin, M. T.; Occhialini, A.; Andralojc, P. J.; Parry, M. A. J.; Hanson, M. R. A Faster Rubisco with Potential to Increase Photosynthesis in Crops. *Nature* **2014**, *513* (7519), 547–550. https://doi.org/10.1038/nature13776.

(125) Occhialini, A.; Lin, M. T.; Andralojc, P. J.; Hanson, M. R.; Parry, M. A. J. Transgenic Tobacco Plants with Improved Cyanobacterial Rubisco Expression but No Extra Assembly Factors Grow at near Wild-Type Rates If Provided with Elevated CO2. *Plant J. Cell Mol. Biol.* **2016**, *85* (1), 148–160. https://doi.org/10.1111/tpj.13098.

(126) Long, B. M.; Hee, W. Y.; Sharwood, R. E.; Rae, B. D.; Kaines, S.; Lim, Y.-L.; Nguyen, N. D.; Massey, B.; Bala, S.; von Caemmerer, S.; Badger, M. R.; Price, G. D. Carboxysome Encapsulation of the CO2-Fixing Enzyme Rubisco in Tobacco Chloroplasts. *Nat. Commun.* **2018**, *9* (1), 3570. https://doi.org/10.1038/s41467-018-06044-0.

(127) Borden, J. S.; Savage, D. F. New Discoveries Expand Possibilities for Carboxysome Engineering. *Curr. Opin. Microbiol.* **2021**, *61*, 58–66. https://doi.org/10.1016/j.mib.2021.03.002.

(128) Nguyen, N. D.; Pulsford, S. B.; Förster, B.; Rottet, S.; Rourke, L.; Long, B. M.; Price, G. D. A Carboxysome-Based CO Concentrating Mechanism for C Crop Chloroplasts: Advances and the Road Ahead. *Plant J.* **2024**, *118* (4), 940–952. https://doi.org/10.1111/tpj.16667.

(129) Zeng, R.; Lv, C.; Zang, J.; Zhang, T.; Zhao, G. Designing Stacked Assembly of Type III Rubisco for CO2 Fixation with Higher Efficiency. *J. Agric. Food Chem.* **2022**. https://doi.org/10.1021/acs.jafc.2c02521.

(130) Chen, T.; Fang, Y.; Jiang, Q.; Dykes, G. F.; Lin, Y.; Price, G. D.; Long, B. M.; Liu, L.-N. Incorporation of Functional Rubisco Activases into Engineered Carboxysomes to Enhance Carbon Fixation. *ACS Synth. Biol.* **2021**, *11* (1), 154–161. https://doi.org/10.1021/acssynbio.1c00311.

(131) Nakajima, T.; Kajihata, S.; Yoshikawa, K.; Matsuda, F.; Furusawa, C.; Hirasawa, T.; Shimizu, H. Integrated Metabolic Flux and Omics Analysis of Synechocystis Sp. PCC 6803 under Mixotrophic and Photoheterotrophic Conditions. *Plant Cell Physiol.* **2014**, *55* (9), 1605–1612. https://doi.org/10.1093/pcp/pcu091.

(132) Rubin, B. E.; Wetmore, K. M.; Price, M. N.; Diamond, S.; Shultzaberger, R. K.; Lowe, L. C.; Curtin, G.; Arkin, A. P.; Deutschbauer, A.; Golden, S. S. The Essential Gene Set of a Photosynthetic Organism. *Proc. Natl. Acad. Sci.* **2015**, *112* (48). https://doi.org/10.1073/pnas.1519220112.

(133) Bernstein, H. C.; McClure, R. S.; Hill, E. A.; Markillie, L. M.; Chrisler, W. B.; Romine, M. F.; McDermott, J. E.; Posewitz, M. C.; Bryant, D. A.; Konopka, A. E.; Fredrickson, J. K.; Beliaev, A. S. Unlocking the Constraints of Cyanobacterial Productivity: Acclimations Enabling Ultrafast Growth. *mBio* **2016**, *7* (4), e00949-16. https://doi.org/10.1128/mBio.00949-16.

(134) Moore, K. A.; Altus, S.; Tay, J. W.; Meehl, J. B.; Johnson, E. B.; Bortz, D. M.; Cameron, J. C. Mechanical Regulation of Photosynthesis in Cyanobacteria. *Nat. Microbiol.* **2020**, *5* (5), 757–767. https://doi.org/10.1038/s41564-020-0684-2.

(135) Porra, R. J.; Thompson, W. A.; Kriedemann, P. E. Determination of Accurate Extinction Coefficients and Simultaneous Equations for Assaying Chlorophylls a and b Extracted with Four Different Solvents: Verification of the Concentration of Chlorophyll Standards by Atomic Absorption Spectroscopy. *Biochim. Biophys. Acta BBA - Bioenerg.* **1989**, *975* (3), 384–394. https://doi.org/10.1016/S0005-2728(89)80347-0.

(136) Tay, J. W.; Cameron, J. C. Chapter Four - Computational and Biochemical Methods to Measure the Activity of Carboxysomes and Protein Organelles in Vivo. In *Methods in Enzymology*; Jez, J., Ed.; Biochemical Pathways and Environmental Responses in Plants: Part C; Academic Press, 2023; Vol. 683, pp 81–100. https://doi.org/10.1016/bs.mie.2022.09.010.

(137) Mohajerani, F.; Sayer, E.; Neil, C.; Inlow, K.; Hagan, M. F. Mechanisms of Scaffold-Mediated Microcompartment Assembly and Size Control. *ACS Nano* **2021**, *15* (3), 4197–4212. https://doi.org/10.1021/acsnano.0c05715.

(138) Cai, F.; Dou, Z.; Bernstein, S. L.; Leverenz, R.; Williams, E. B.; Heinhorst, S.; Shively, J.; Cannon, G. C.; Kerfeld, C. A. Advances in Understanding Carboxysome Assembly in Prochlorococcus and Synechococcus Implicate CsoS2 as a Critical Component. *Life* **2015**, *5* (2), 1141–1171. https://doi.org/10.3390/life5021141.

(139) Carpenter, W. B.; Lavania, A. A.; Squires, A. H.; Moerner, W. E. Label-Free Anti-Brownian Trapping of Single Nanoparticles in Solution. *J. Phys. Chem. C* **2024**. https://doi.org/10.1021/acs.jpcc.4c05878.

(140) Long, B. M.; Förster, B.; Pulsford, S. B.; Price, G. D.; Badger, M. R. Rubisco Proton Production Can Drive the Elevation of CO2 within Condensates and Carboxysomes. *Proc. Natl. Acad. Sci.* **2021**, *118* (18). https://doi.org/10.1073/pnas.2014406118.

(141) Huang, J.; Jiang, Q.; Yang, M.; Dykes, G. F.; Weetman, S. L.; Xin, W.; He, H.-L.; Liu, L.-N. Probing the Internal pH and Permeability of a Carboxysome Shell. *Biomacromolecules* **2022**. https://doi.org/10.1021/acs.biomac.2c00781.

(142) Menon, B. B.; Heinhorst, S.; Shively, J. M.; Cannon, G. C. The Carboxysome Shell Is Permeable to Protons. *J. Bacteriol.* **2010**, *192* (22), 5881–5886. https://doi.org/10.1128/JB.00903-10.

(143) Kinney, J. N.; Axen, S. D.; Kerfeld, C. A. Comparative Analysis of Carboxysome Shell Proteins. *Photosynth. Res.* **2011**, *109* (1), 21–32. https://doi.org/10.1007/s11120-011-9624-6.

(144) Sutter, M.; Utschig, L. M.; Niklas, J.; Paul, S.; Kahan, D. N.; Gupta, S.; Poluektov, O. G.; Ferlez, B. H.; Tefft, N. M.; TerAvest, M. A.; Hickey, D. P.; Vermaas, J. V.; Ralston, C. Y.; Kerfeld, C. A. Electrochemical Cofactor Recycling of Bacterial Microcompartments. *Proc. Natl. Acad. Sci. U. S. A.* **2024**, *121* (49), 2024.07.15.603600. https://doi.org/10.1073/pnas.2414220121.

(145) Kim, G.; Weiss, S. J.; Levine, R. L. Methionine Oxidation and Reduction in Proteins. *Biochim. Biophys. Acta* **2014**, *1840* (2), 10.1016/j.bbagen.2013.04.038. https://doi.org/10.1016/j.bbagen.2013.04.038.

(146) Sun, Y.; Wollman, A. J. M.; Huang, F.; Leake, M. C.; Liu, L.-N. Single-Organelle Quantification Reveals Stoichiometric and Structural Variability of Carboxysomes Dependent on the Environment. *Plant Cell* **2019**, *31* (7), 1648–1664. https://doi.org/10.1105/tpc.18.00787.

(147) Turnšek, J. B.; Oltrogge, L. M.; Savage, D. F. Conserved and Repetitive Motifs in an Intrinsically Disordered Protein Drive α-Carboxysome Assembly. *J. Biol. Chem.* **2024**, *300* (8), 107532. https://doi.org/10.1016/j.jbc.2024.107532.

(148) Abernathy, M. H.; Czajka, J. J.; Allen, D. K.; Hill, N. C.; Cameron, J. C.; Tang, Y. J. Cyanobacterial Carboxysome Mutant Analysis Reveals the Influence of Enzyme Compartmentalization on Cellular Metabolism and Metabolic Network Rigidity. *Metab. Eng.* **2019**, *54*, 222–231. https://doi.org/10.1016/j.ymben.2019.04.010.

(149) Woodger, F. J.; Badger, M. R.; Price, G. D. Inorganic Carbon Limitation Induces Transcripts Encoding Components of the CO2-Concentrating Mechanism in Synechococcus Sp. PCC7942 through a Redox-Independent Pathway. *Plant Physiol.* **2003**, *133* (4), 2069–2080. https://doi.org/10.1104/pp.103.029728.

(150) Eisenhut, M.; von Wobeser, E. A.; Jonas, L.; Schubert, H.; Ibelings, B. W.; Bauwe, H.; Matthijs, H. C. P.; Hagemann, M. Long-Term Response toward Inorganic Carbon Limitation in Wild Type and Glycolate Turnover Mutants of the Cyanobacterium Synechocystis Sp. Strain PCC 6803. *Plant Physiol.* **2007**, *144* (4), 1946–1959. https://doi.org/10.1104/pp.107.103341.

(151) Whitehead, L.; Long, B. M.; Price, G. D.; Badger, M. R. Comparing the in Vivo Function of α-Carboxysomes and β-Carboxysomes in Two Model Cyanobacteria. *Plant Physiol.* **2014**, *165* (1), 398–411. https://doi.org/10.1104/pp.114.237941.

(152) McKay, R. M. L.; Gibbs, S. P.; Espie, G. S. Effect of Dissolved Inorganic Carbon on the Expression of Carboxysomes, Localization of Rubisco and the Mode of Inorganic Carbon Transport in Cells of the Cyanobacterium Synechococcus UTEX 625. *Arch. Microbiol.* **1993**, *159* (1), 21–29. https://doi.org/10.1007/BF00244259.

(153) Flamholz, A. I.; Dugan, E.; Panich, J.; Desmarais, J. J.; Oltrogge, L. M.; Fischer, W. W.; Singer, S. W.; Savage, D. F. Trajectories for the Evolution of Bacterial CO2-Concentrating Mechanisms. *Proc. Natl. Acad. Sci.* **2022**, *119* (49), e2210539119. https://doi.org/10.1073/pnas.2210539119.

(154) Nishimura, T.; Yamaguchi, O.; Takatani, N.; Maeda, S.; Omata, T. In Vitro and in Vivo Analyses of the Role of the Carboxysomal β-Type Carbonic Anhydrase of the Cyanobacterium Synechococcus Elongatus in Carboxylation of Ribulose-1,5-Bisphosphate. *Photosynth. Res.* **2014**, *121* (2–3), 151–157. https://doi.org/10.1007/s11120-014-9986-7.

(155) Yokoo, R.; Hood, R. D.; Savage, D. F. Live-Cell Imaging of Cyanobacteria. *Photosynth. Res.* **2015**, *126* (1), 33–46. https://doi.org/10.1007/s11120-014-0049-x.

(156) Muzzey, D.; van Oudenaarden, A. Quantitative Time-Lapse Fluorescence Microscopy in Single Cells. *Annu. Rev. Cell Dev. Biol.* **2009**, *25* (1), 301–327. https://doi.org/10.1146/annurev.cellbio.042308.113408.

(157) Young, J. W.; Locke, J. C. W.; Altinok, A.; Rosenfeld, N.; Bacarian, T.; Swain, P. S.; Mjolsness, E.; Elowitz, M. B. Measuring Single-Cell Gene Expression Dynamics in Bacteria Using Fluorescence Time-Lapse Microscopy. *Nat. Protoc.* **2012**, *7* (1), 80–88. https://doi.org/10.1038/nprot.2011.432.

(158) Schneider, D.; Fuhrmann, E.; Scholz, I.; Hess, W. R.; Graumann, P. L. Fluorescence Staining of Live Cyanobacterial Cells Suggest Non-Stringent Chromosome Segregation and Absence of a

Connection between Cytoplasmic and Thylakoid Membranes. *BMC Cell Biol.* **2007**, *8* (1), 39. https://doi.org/10.1186/1471-2121-8-39.

(159) MacCready, J. S.; Hakim, P.; Young, E. J.; Hu, L.; Liu, J.; Osteryoung, K. W.; Vecchiarelli, A. G.; Ducat, D. C. Protein Gradients on the Nucleoid Position the Carbon-Fixing Organelles of Cyanobacteria. *eLife* **2018**, *7*, e39723. https://doi.org/10.7554/eLife.39723.

(160) Sieracki, M. E.; Reichenbach, S. E.; Webb, K. L. Evaluation of Automated Threshold Selection Methods for Accurately Sizing Microscopic Fluorescent Cells by Image Analysis. *Appl. Environ. Microbiol.* **1989**, *55* (11), 2762–2772. https://doi.org/10.1128/aem.55.11.2762-2772.1989.

(161) Dima, A. A.; Elliott, J. T.; Filliben, J. J.; Halter, M.; Peskin, A.; Bernal, J.; Kociolek, M.; Brady, M. C.; Tang, H. C.; Plant, A. L. Comparison of Segmentation Algorithms for Fluorescence Microscopy Images of Cells. *Cytometry A* **2011**, *79A* (7), 545–559. https://doi.org/10.1002/cyto.a.21079.

(162) Kraus, B.; Ziegler, M.; Wolff, H. Linear Fluorescence Unmixing in Cell Biological Research.

(163) Orth, A.; Ghosh, R. N.; Wilson, E. R.; Doughney, T.; Brown, H.; Reineck, P.; Thompson, J. G.; Gibson, B. C. Super-Multiplexed Fluorescence Microscopy via Photostability Contrast. *Biomed. Opt. Express* **2018**, *9* (7), 2943–2954. https://doi.org/10.1364/BOE.9.002943.

(164) Ali, R.; Gooding, M.; Szilágyi, T.; Vojnovic, B.; Christlieb, M.; Brady, M. Automatic Segmentation of Adherent Biological Cell Boundaries and Nuclei from Brightfield Microscopy Images. *Mach. Vis. Appl.* **2012**, *23* (4), 607–621. https://doi.org/10.1007/s00138-011-0337-9.

(165) Buggenthin, F.; Marr, C.; Schwarzfischer, M.; Hoppe, P. S.; Hilsenbeck, O.; Schroeder, T.; Theis, F. J. An Automatic Method for Robust and Fast Cell Detection in Bright Field Images from High-Throughput Microscopy. *BMC Bioinformatics* **2013**, *14* (1), 297. https://doi.org/10.1186/1471-2105-14-297.

(166) Moen, E.; Bannon, D.; Kudo, T.; Graf, W.; Covert, M.; Van Valen, D. Deep Learning for Cellular Image Analysis. *Nat. Methods* **2019**, *16* (12), 1233–1246. https://doi.org/10.1038/s41592-019-0403-1.

(167) Stringer, C.; Wang, T.; Michaelos, M.; Pachitariu, M. Cellpose: A Generalist Algorithm for Cellular Segmentation. *Nat. Methods* **2021**, *18* (1), 100–106. https://doi.org/10.1038/s41592-020-01018-x.

(168) Pachitariu, M.; Stringer, C. Cellpose 2.0: How to Train Your Own Model. *Nat. Methods* **2022**, *19* (12), 1634–1641. https://doi.org/10.1038/s41592-022-01663-4.

(169) Stringer, C.; Pachitariu, M. Cellpose3: One-Click Image Restoration for Improved Cellular Segmentation. bioRxiv February 12, 2024, p 2024.02.10.579780. https://doi.org/10.1101/2024.02.10.579780.

(170) Cutler, K. J.; Stringer, C.; Lo, T. W.; Rappez, L.; Stroustrup, N.; Brook Peterson, S.; Wiggins, P. A.; Mougous, J. D. Omnipose: A High-Precision Morphology-Independent Solution for Bacterial Cell Segmentation. *Nat. Methods* **2022**, *19* (11), 1438–1448. https://doi.org/10.1038/s41592-022-01639-4.

(171) Rainio, O.; Teuho, J.; Klén, R. Evaluation Metrics and Statistical Tests for Machine Learning. *Sci. Rep.* **2024**, *14*, 6086. https://doi.org/10.1038/s41598-024-56706-x.

(172) Muro-Pastor, A. M.; Hess, W. R. Heterocyst Differentiation: From Single Mutants to Global Approaches. *Trends Microbiol.* **2012**, *20* (11), 548–557. https://doi.org/10.1016/j.tim.2012.07.005.

(173) Flores, E.; Herrero, A. Compartmentalized Function through Cell Differentiation in Filamentous Cyanobacteria. *Nat. Rev. Microbiol.* **2010**, *8* (1), 39–50. https://doi.org/10.1038/nrmicro2242.

(174) Hatzenpichler, R.; Krukenberg, V.; Spietz, R. L.; Jay, Z. J. Next-Generation Physiology Approaches to Study Microbiome Function at Single Cell Level. *Nat. Rev. Microbiol.* **2020**, *18* (4), 241–256. https://doi.org/10.1038/s41579-020-0323-1.

(175) Rombouts, S.; Mas, A.; Le Gall, A.; Fiche, J.-B.; Mignot, T.; Nollmann, M. Multi-Scale Dynamic Imaging Reveals That Cooperative Motility Behaviors Promote Efficient Predation in Bacteria. *Nat. Commun.* **2023**, *14* (1), 5588. https://doi.org/10.1038/s41467-023-41193-x.

(176) Batsch, M.; Guex, I.; Todorov, H.; Heiman, C. M.; Vacheron, J.; Vorholt, J. A.; Keel, C.; van der Meer, J. R. Fragmented Micro-Growth Habitats Present Opportunities for Alternative Competitive Outcomes. *Nat. Commun.* **2024**, *15* (1), 7591. https://doi.org/10.1038/s41467-024-51944-z.

(177) Tay, J. W.; Cameron, J. C. Asymmetric Survival in Single-Cell Lineages of Cyanobacteria in Response to Photodamage. *Photosynth. Res.* **2023**, *155* (3), 289–297. https://doi.org/10.1007/s11120-022-00986-9.

(178) Paszke, A.; Gross, S.; Massa, F.; Lerer, A.; Bradbury, J.; Chanan, G.; Killeen, T.; Lin, Z.; Gimelshein, N.; Antiga, L.; Desmaison, A.; Köpf, A.; Yang, E.; DeVito, Z.; Raison, M.; Tejani, A.; Chilamkurthy, S.; Steiner, B.; Fang, L.; Bai, J.; Chintala, S. PyTorch: An Imperative Style, High-Performance Deep Learning Library. arXiv December 3, 2019. https://doi.org/10.48550/arXiv.1912.01703.

(179) Krizhevsky, A.; Sutskever, I.; Hinton, G. E. ImageNet Classification with Deep Convolutional Neural Networks. *Commun ACM* **2017**, *60* (6), 84–90. https://doi.org/10.1145/3065386.

(180) Kingma, D. P.; Ba, J. Adam: A Method for Stochastic Optimization. arXiv January 30, 2017. https://doi.org/10.48550/arXiv.1412.6980.

(181) Bradski, G. The OpenCV Library, 2000.

(182) Aguilera, A.; Klemenčič, M.; Sueldo, D. J.; Rzymski, P.; Giannuzzi, L.; Martin, M. V. Cell Death in Cyanobacteria: Current Understanding and Recommendations for a Consensus on Its Nomenclature. *Front. Microbiol.* **2021**, *12*, 631654. https://doi.org/10.3389/fmicb.2021.631654.

(183) Alon, U.; Surette, M. G.; Barkai, N.; Leibler, S. Robustness in Bacterial Chemotaxis. *Nature* **1999**, *397* (6715), 168–171. https://doi.org/10.1038/16483.

(184) Barkai, N.; Leibler, S. Robustness in Simple Biochemical Networks. *Nature* **1997**, *387* (6636), 913–917. https://doi.org/10.1038/43199.

(185) Stevens, R.; Stevens, L.; Price, N. The Stabilities of Various Thiol Compounds Used in Protein Purifications. *Biochem. Educ.* **1983**, *11* (2), 70. https://doi.org/10.1016/0307-4412(83)90048-1.

(186) Tay, J. W.; Cameron, J. C. Computational and Biochemical Methods to Measure the Activity of Carboxysomes and Protein Organelles in Vivo. In *Methods in Enzymology*; Academic Press, 2022. https://doi.org/10.1016/bs.mie.2022.09.010.

(187) Meyer, A. J.; Dick, T. P. Fluorescent Protein-Based Redox Probes. *Antioxid. Redox Signal.* **2010**, *13* (5), 621–650. https://doi.org/10.1089/ars.2009.2948.

(188) Schwarzländer, M.; Dick, T. P.; Meyer, A. J.; Morgan, B. Dissecting Redox Biology Using Fluorescent Protein Sensors. *Antioxid. Redox Signal.* **2016**, *24* (13), 680–712. https://doi.org/10.1089/ars.2015.6266.

(189) Gutscher, M.; Sobotta, M. C.; Wabnitz, G. H.; Ballikaya, S.; Meyer, A. J.; Samstag, Y.; Dick, T. P. Proximity-Based Protein Thiol Oxidation by H2O2-Scavenging Peroxidases*♦. *J. Biol. Chem.* **2009**, *284* (46), 31532–31540. https://doi.org/10.1074/jbc.M109.059246.

(190) Ma, Y.; Sun, Q.; Smith, S. C. The Mechanism of Oxidation in Chromophore Maturation of Wild-Type Green Fluorescent Protein: A Theoretical Study. *Phys. Chem. Chem. Phys. PCCP* **2017**, *19* (20), 12942–12952. https://doi.org/10.1039/c6cp07983k.

Appendix

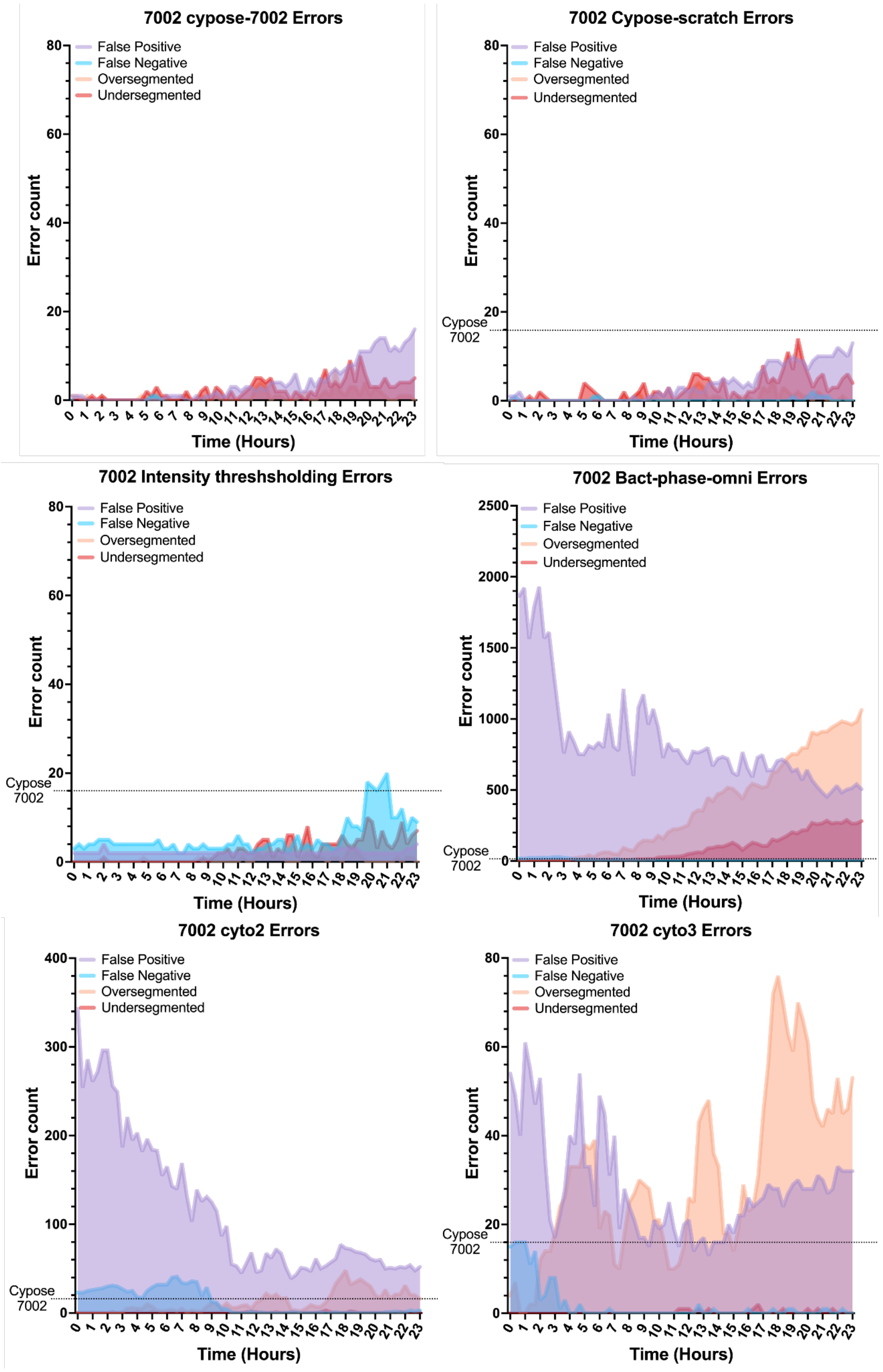

Appendix Figure 1. PCC 7002 segmentation errors over time

Segmentation error over time of the PCC 7002 benchmark. The max number of errors for cypose-7002 is marked on the other graphs to provide easier relative comparison.

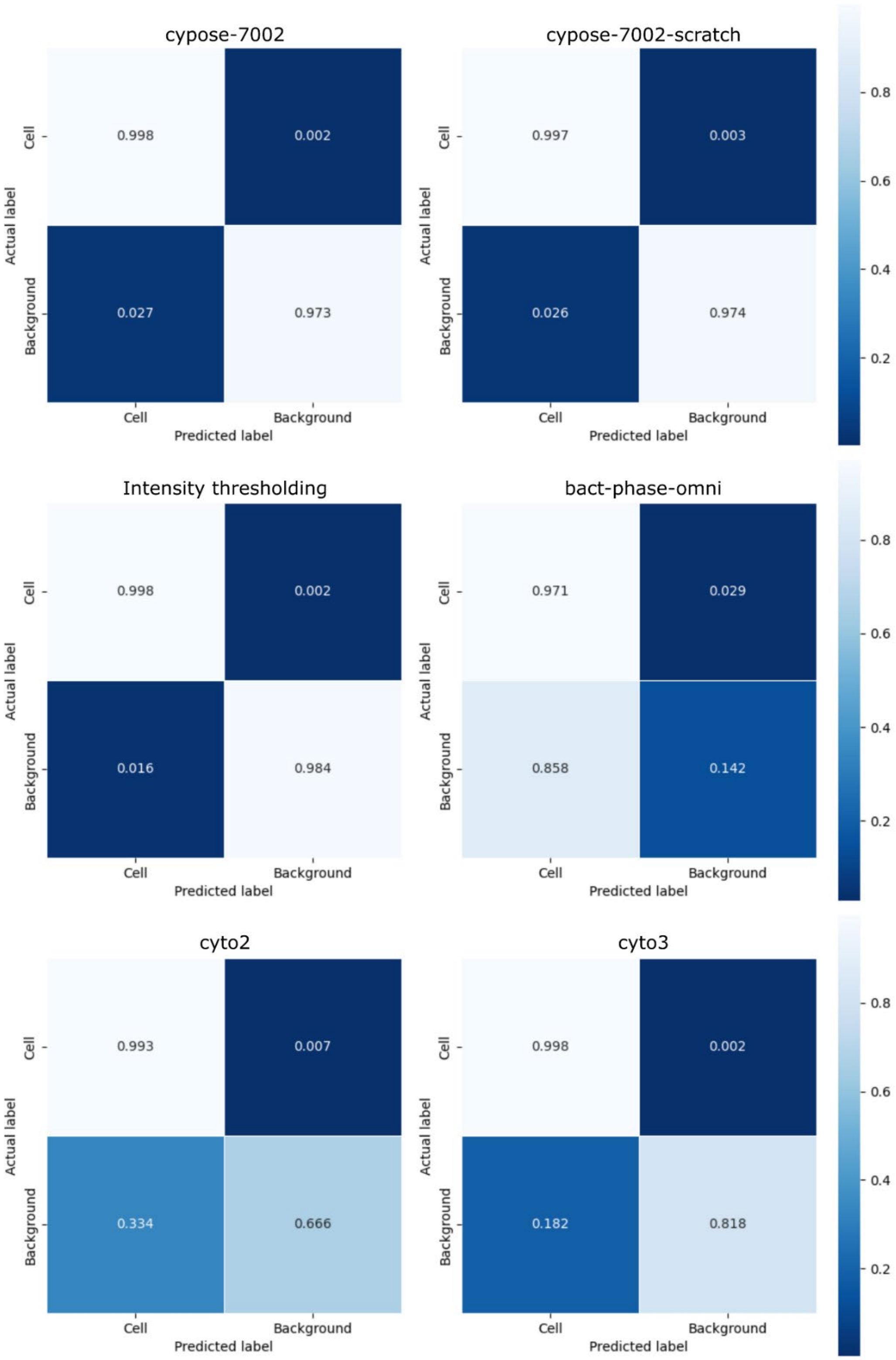

Appendix Figure 2. PCC 7002 segmentation confusion matrices

Confusion matrixes for segmentation models on the PCC 7002 benchmark.

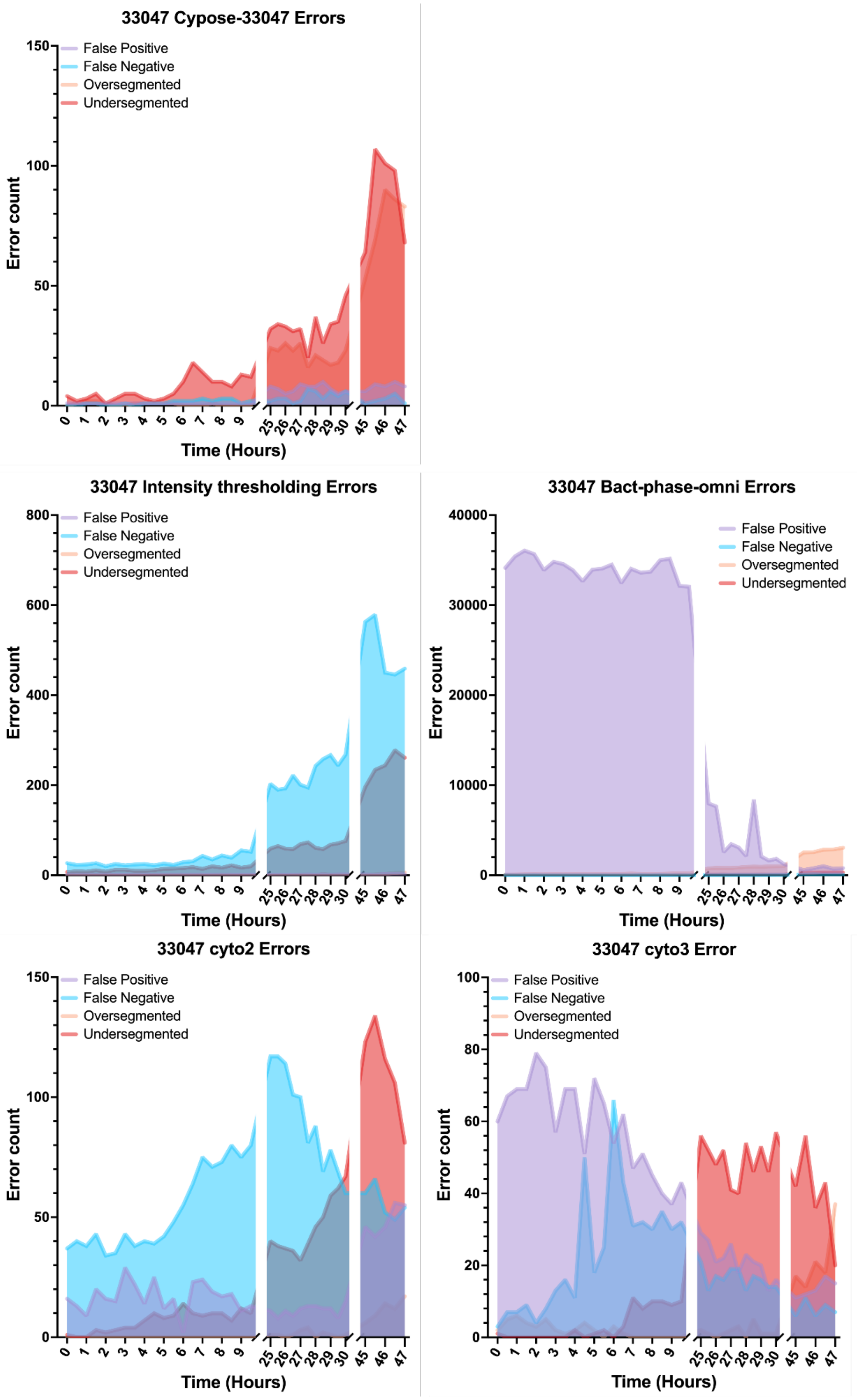

Appendix Figure 3. ATCC 33047 segmentation errors over time

Segmentation errors over time of the ATCC 33047 benchmark.

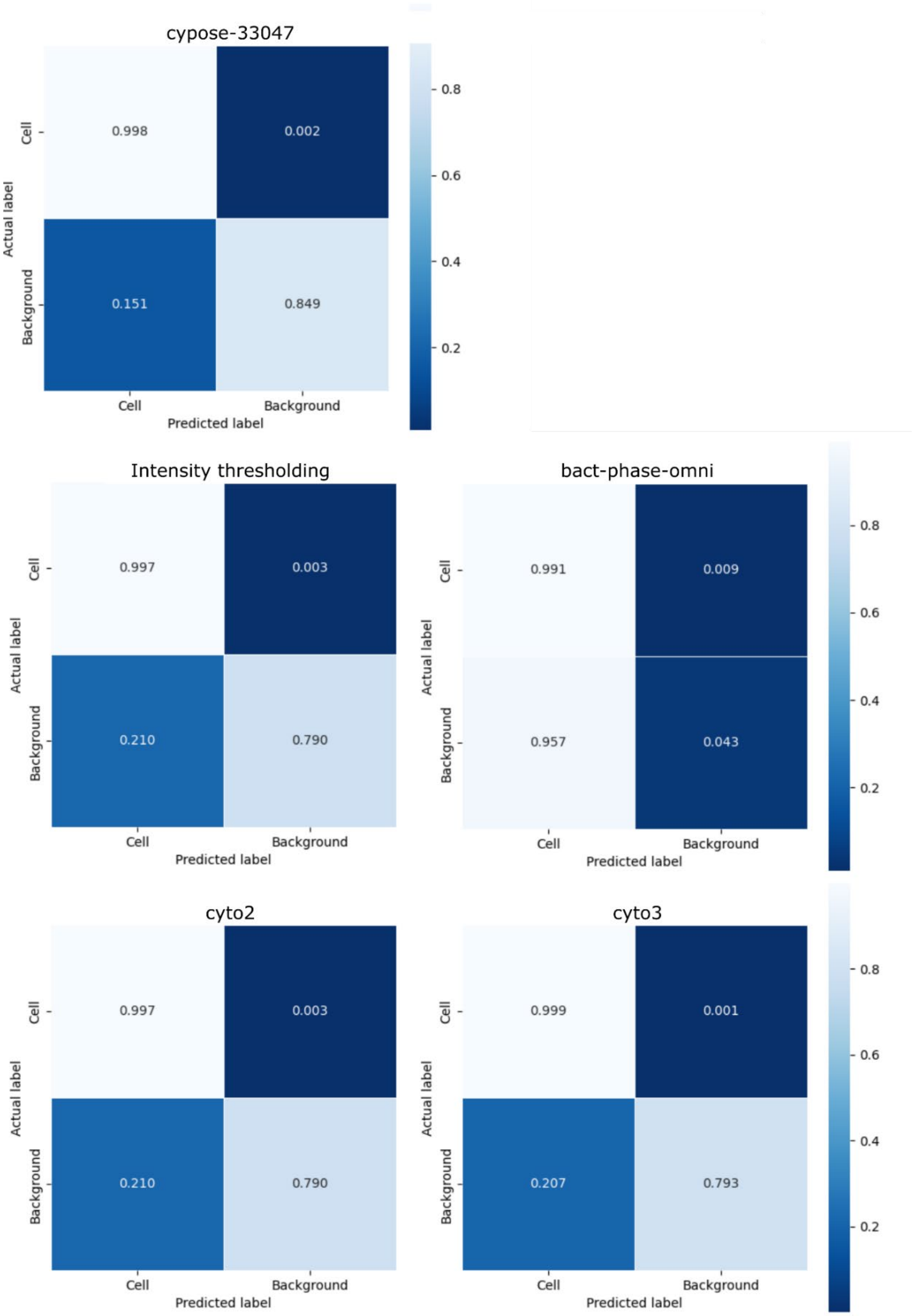

Appendix Figure 4. ATCC 33047 segmentation confusion matrices

Confusion matrixes for segmentation models on the ATCC 33047 benchmark.